



CENTER FOR INFRASTRUCTURE ENGINEERING STUDIES

SECONDARY REINFORCEMENT FOR FIBER REINFORCED POLYMERS REINFORCED CONCRETE PANELS

by

Daniel Koenigsfeld

Dr. John J. Myers

University of Missouri-Rolla

**CIES
03-45**

Disclaimer

The contents of this report reflect the views of the author(s), who are responsible for the facts and the accuracy of information presented herein. This document is disseminated under the sponsorship of the Center for Infrastructure Engineering Studies (CIES), University of Missouri -Rolla, in the interest of information exchange. CIES assumes no liability for the contents or use thereof.

The mission of CIES is to provide leadership in research and education for solving society's problems affecting the nation's infrastructure systems. CIES is the primary conduit for communication among those on the UMR campus interested in infrastructure studies and provides coordination for collaborative efforts. CIES activities include interdisciplinary research and development with projects tailored to address needs of federal agencies, state agencies, and private industry as well as technology transfer and continuing/distance education to the engineering community and industry.

Center for Infrastructure Engineering Studies (CIES)

University of Missouri-Rolla
223 Engineering Research Lab

1870 Miner Circle

Rolla, MO 65409-0710

Tel: (573) 341-6223; fax -6215

E-mail: cies@umr.edu

www.cies.umr.edu

ABSTRACT

Controlling the width and pattern of concrete cracks are important for two primary reasons; durability and aesthetic appearance. Due to rebar corrosion accelerating the deterioration of concrete bridge decks, emphasis has been placed on conserving the service life of structures through adequate crack control. Volume changes due to shrinkage and temperature alone can produce tensile stresses large enough to produce cracks if subjected to sufficient restraint. Reinforcement can not prevent cracks, yet with proper design crack widths are smaller and less likely to contribute to durability problems. Limitations and problems associated with epoxy-coated rebar have led to efforts of trying nonmetallic rebar, such as glass fiber-reinforced polymers (GFRP).

Currently, ACI 440.1R-03 “Guide for the Design and Construction of Concrete Reinforced with FRP Bars” requires in many applications a secondary reinforcement ratio that is significantly larger than the primary reinforcement ratio based on flexural requirements be used. The current minimum reinforcement ratio guideline for shrinkage and temperature has no experimental validation and is considered to be excessive by many experts.

The objective of the project was to investigate the development of an empirical secondary reinforcement ratio for FRP based on experimental tests performed at the University of Missouri-Rolla (UMR). This study was separated into three phases which examined both early-age and later-age effects of various reinforcement ratios on the formation of shrinkage/temperature and flexural cracks. This report provides the experimental program and test procedures as well as the test results and observations.

ACKNOWLEDGMENTS

I would like to express my sincere gratitude to my advisor Dr. John J. Myers for his guidance and support throughout my research project. In addition, a special thanks to my committee members, Dr. Antonio Nanni and Dr. K. Chandrashekhara, for their suggestions and comments throughout this research.

Sincere thanks to the Center for Infrastructure Engineering Studies (CIES) and the Department of Civil Engineering at the University of Missouri-Rolla (UMR), particularly Gary Abbot, Bill Fredrickson, Jeff Bradshaw, Jason Cox, and Steve Gabel for their technical support. I am very appreciative of my colleagues and friends, especially Preston Carney and William Bolte, and the CIES undergraduate research assistants who contributed to the experimental phase of the project.

For their assistance with funding and donation of materials, I would also like to thank the Repair of Buildings and Bridges with Composites (RB2C) National Science Foundation (NSF) Industry University Cooperative Research Center, and Hughes Brothers, Inc.

TABLE OF CONTENTS

	Page
ABSTRACT.....	iv
ACKNOWLEDGMENTS	v
LIST OF ILLUSTRATIONS.....	ix
LIST OF TABLES.....	xii
NOTATION.....	xiv
SECTION	
1. INTRODUCTION.....	1
1.1. BACKGROUND	1
1.2. SCOPE AND OBJECTIVES.....	3
1.3. LAYOUT OF THE REPORT.....	4
2. LITERATURE REVIEW.....	6
2.1. SIGNIFICANTS OF CRACKS	6
2.2. CRACK FORMATION AND TYPES.....	8
2.2.1. Crack Formation.....	9
2.2.2. Drying Shrinkage Cracks.....	11
2.2.3. Temperature Cracks.....	17
2.2.4. Plastic Shrinkage Cracks.....	22
2.3. SHRINKAGE REINFORCEMENT.....	25
2.3.1 ACI 318 Code Requirements for Mild Steel.....	28
2.3.2 ACI 440 Code Recommendations for FRP.....	29
2.4. PREVIOUS RESEARCH.....	31

3. EXPERIMENTAL PROGRAM.....	34
3.1. TEST PROGRAM	34
3.2. TEST SPECIMENS	37
3.2.1. Phase I Specimens.....	37
3.2.2. Phase II Specimens.....	39
3.2.3. Phase III Specimens.....	40
3.2.4. Form Development.....	42
3.2.5. Mixing Procedure.....	44
3.2.6. Concrete Placement and Finishing.....	44
3.2.7. Curing Procedure.....	46
3.3. MATERIALS.....	46
3.3.1. Concrete Mixes and Properties.....	46
3.3.2. Steel Rebar.....	51
3.3.3. GFRP Rebar	51
3.4. TEST SETUP AND PROCEDURES	52
3.4.1. Phase I Test Setup.....	53
3.4.2. Phase I Test Procedure.....	56
3.4.3. Phase II Test Setup.....	57
3.4.4. Phase II Test Procedure.....	60
3.4.5. Phase III Test Setup.....	61
3.4.6. Phase III Test Procedure.....	64
3.5. SUPPLEMENTAL TEST METHODS INVESTIGATED	64

4. TEST RESULTS AND DISCUSSIONS.....	67
4.1. CONCRETE COMPRESSIVE STRENGTH TESTS	67
4.2. CONCRETE FLEXURAL STRENGTH TESTS.....	69
4.3. REINFORCING STEEL TENSILE STRENGTH CHARACTERIZATON ...	71
4.4. PHASE I TESTS.....	73
4.5. PHASE II TESTS	83
4.6. PHASE III TESTS	90
4.7. SUMMARY	99
5. CONCLUSIONS AND FUTURE RESEARCH.....	101
5.1. CONCLUSIONS.....	101
5.2. FUTURE RESEARCH.....	102
APPENDICIES	
A. SPECIMEN ULTIMATE CRACK PATTERNS.....	104
B. PHASE III DEFLECTION AND LOAD VS. STRAIN GRAPHS.....	117
BIBLIOGRAPHY.....	132

LIST OF ILLUSTRATIONS

Figure	Page
2.1. Cracking of Concrete Due to Volume Change and Restraint	10
2.2. Stress in Concrete After First Crack in a Member Subjected to Axial Force	10
2.3. Typical Drying and Rewetting Behavior of Concrete	11
2.4. Effect of Aggregate Size on Water Requirement of Non-AE Concrete	14
2.5. Typical Effect of Concrete Water Content on Drying Shrinkage	16
2.6. Effect of Fresh Concrete Temperature on Water Content for a Given Slump	16
2.7. Heat Transfer Processes for a Bridge Deck During a Summer Day	19
2.8. Typical Thermal Gradient for a Standard Bridge System in Missouri	20
2.9. Thermal Stressed for a MoDOT Type III Girder	20
2.10. Reinforcement Behavior for Concrete Expansion and Contraction	28
3.1. Common Phase I Specimens Before Concrete Placement	38
3.2. Steel Angle Used to Predetermine Crack Location	38
3.3. Embedded Threaded Rod with Hex Nut and Washer	39
3.4. Grooves Cut to Predetermine Crack Location	40
3.5. Common Phase III Panel Before Concrete Placement	41
3.6. Illustration of Phase III Groove Pattern	43
3.7. Common Strain Gauge Application to GFRP Rebar	43
3.8. Platform System Retrofitted for Phase III	44
3.9. Specimen Leveling of Fresh Concrete	45
3.10. Phase III Concrete Curing	47
3.11. Environmental Chamber	54

3.12.	Phase I Test Setup.....	55
3.13.	Load Cell Used in Phase I Testing.....	56
3.14.	Phase II Test Setup.....	59
3.15.	Phase II Method of Measuring Deformation	60
3.16.	Phase III Method of Measuring Deflection	62
3.17.	Phase III Test Setup	63
3.18.	Specimen Forms to Investigate Plastic Shrinkage Cracks.....	65
3.19.	Specimen Forms with Minimal Restraint to Investigate Shrinkage Cracks	66
4.1.	Forney Testing Machine	68
4.2.	Compressive Strength Gain Curve for Phase III Concrete	68
4.3.	Third-Point Loading of Flexural Beam.....	70
4.4.	Steel Rebar Tensile Coupon Test.....	72
4.5.	Typical Stress-Strain Curve for a No. 5 Steel Rebar	72
4.6.	Phase I Environmental Chamber Ambient Temperature Cycles	74
4.7.	Phase I Environmental Chamber Relative Humidity Cycles.....	74
4.8.	Phase I Micro-Strain vs. Concrete Age.....	75
4.9.	Phase I Restraint Load vs. Average Crack Width.....	76
4.10.	Phase I Average Peak Crack Width After First Heating Cycle	78
4.11	Phase I Crack Width / Reinforcement Area vs. Reinforcement Area.....	80
4.12	Phase I Expected Peak Crack Widths After First Condition Cycle for GFRP Modulus of Elasticity Range.....	82
4.13	Phase I Peak Crack Width vs. Reinforcement Area for GFRP Modulus of Elasticity Range	82
4.14.	Phase II Typical Specimen Crack Pattern.....	84

4.15.	Phase II Tensile Load vs. Deformation.....	85
4.16.	Phase II Tensile Load vs. Micro-Strain	86
4.17.	Phase II Tensile Load vs. Crack Area.....	87
4.18.	Phase II Tensile Load at a Given Crack Area = 1 in ²	89
4.19.	Phase II Efficiency vs. Reinforcement Area at Crack Area = 1in ²	89
4.20.	Phase III Typical Panel Crack Pattern	92
4.21.	Phase III Typical Deflection Graph	93
4.22.	Phase III Typical Load vs. Micro-Strain Graph.....	93
4.23.	Phase III Load vs. Crack Area for 23.25"x5"x78" Panels.....	94
4.24.	Phase III Load vs. Crack Area for 23.25"x7"x78" Panels.....	95
4.25.	Phase III Load vs. Crack Area for 32"x7"x78" Panels.....	96
4.26.	Phase III Load vs. Mid-Span Deflection for 23.25"x5"x78" Panels	97
4.27.	Phase III Load vs. Mid-Span Deflection for 23.25"x7"x78" Panels	98
4.28.	Phase III Load vs. Mid-Span Deflection for 32"x7"x78" Panels	98

LIST OF TABLES

Table	Page
2.1. Effect of Aggregate Type on Concrete Shrinkage.....	14
2.2. Thermal Coefficient of Expansion of Concrete Depending on Aggregate Type..	22
2.3. Aggregate Coefficient of Thermal Expansion Range.....	23
2.4. Tolerable Crack Widths for Reinforced Concrete	26
2.5. ACI 440-03 Secondary Reinforcement Ratio Analysis	31
3.1. Phase I Test Program Matrix	35
3.2. Phase II Test Program Matrix.....	36
3.3. Phase III Test Program Matrix.....	36
3.4. Phase I Laboratory Mix Design Batched on 01/28/03.....	48
3.5. Phase I Laboratory Mix Design Batched on 02/07/03.....	49
3.6. Phase II Ready Mix Design Batched on 01/14/03	49
3.7. Phase III Ready Mix Design Batched on 09/11/02.....	50
3.8. Phase III Ready Mix Design Batched on 09/17/02.....	50
3.9. ASTM A 615-01 Steel Rebar Design Properties	51
3.10. Aslan 100 GFRP Rebar Design Properties	52
4.1. Cylinder Compressive Strength Results	69
4.2. Flexural Beam Modulus of Rupture Results.....	70
4.3. Steel Rebar Strength Results.....	71
4.4. Phase I Data Analysis Results.....	77

4.5.	Phase I Calculated Crack Widths for Modulus of Elasticity Range	81
4.6.	Phase II Efficiency at a Selected Crack Area	88
4.7.	Phase III Test Results.....	92

NOTATION

- A = Effective tension area of concrete surrounding the tension reinforcement, and having the same centroid as the reinforcement, divided by the number of bars, in²
- A_s = Area of tension steel reinforcement, in²
- d_c = Distance from the extreme tension fiber to the center of the reinforcing bar location closest to it, in.
- E_f = Modulus of elasticity of FRP, psi
- E_s = Modulus of elasticity of steel, psi
- f_{ct} = Tensile stress, psi
- f_{fu} = Design tensile strength of FRP, psi
- f_s = Calculated stress in reinforcement at service loads, psi
- f_y = Yield stress of nonprestressed steel reinforcement, psi
- f_u = Ultimate stress of nonprestressed steel reinforcement, psi
- s = Center-to-center spacing of flexural tension reinforcement nearest to the extreme tension face, in.
- S_{ro} = Distance between the first crack and the cross-section where the stress has increased to f_{ct}
- w = crack width in units of 0.001 in.
- w_c = maximum crack width, in.
- β = Ratio of the distance from the neutral axis to extreme tension fiber to the distance from the neutral axis to the center of the tensile reinforcement
- $\rho_{f,ts}$ = FRP shrinkage and temperature reinforcement ratio

1. INTRODUCTION

1.1. BACKGROUND

Bridges are a substantial part of our infrastructure that contributes to our economy and way of life. To function properly, today's economy significantly relies on bridges to provide a safe and efficient transportation system. This infrastructure represents a tremendous investment in our economy. This investment is increasingly being questioned over time as our infrastructure reaches its critical age and becomes deficient or obsolete. According to the Federal Highway Administration (National Bridge Inventory 2002), more than 27% of the bridges in the United States are classified as being either structurally deficient or functionally obsolete. For the State of Missouri that percentage increased to 37%. As the infrastructure age, traffic volume, and truckloads increase, proper bridge management and maintenance becomes very important. Compared to the substructure and superstructure of a bridge, the service life of the deck is much shorter. Bridge decks commonly require major repair or replacement every 15 to 20 years, while most other components remain in service for 40 or more years. Many times, the corrosion of reinforcing steel in bridge decks is the critical factor which leads to structural deficiency and a shortened service life. As water, oxygen, and chloride ions combine on the surface of exposed steel rebar, rust is produced. This chemical reaction of corrosion produces an increase in the original steel volume that causes the reinforcement to debond from the concrete. This debonding eventually causes delamination of the bridge deck and loss of structural integrity.

One effective method of reducing concrete deterioration and steel corrosion is by limiting the crack widths. When concrete is subjected to proper restraint, drying

shrinkage and temperature alone commonly produce tensile stresses large enough to produce cracks. These cracks provide the easiest path for water, oxygen, and chloride ions from deicing salt to penetrate concrete bridge decks. Reinforcement can not prevent cracks, yet with proper design they can be controlled. With adequate reinforcement more cracks with smaller widths are formed instead of fewer cracks with larger widths that accelerate durability problems.

Epoxy-coated reinforcement, galvanized steel reinforcement, and cathode protection have been used to prevent corrosion in bridge decks, yet over the years these techniques have shown only to delay corrosion instead of a preventative technique. Limitations and problems associated with epoxy-coated reinforcement have led to efforts of trying nonmetallic rebar, such as glass fiber-reinforced polymers (GFRP).

Today fiber-reinforced polymers (FRP) have become an alternative form of concrete reinforcement in applications where corrosion is of concern. The use of FRP reinforcement has been traced back as far as World War II. These composite materials were first used by the aerospace industry since it was a relatively lightweight and high-strength material. In the 1960's FRP was first considered for use as concrete reinforcement. During the 1990's, the potential for FRP reinforcement became more evident due to increasing bridge deterioration and field examples of epoxy-coated rebar corrosion throughout the country (ACI Committee 440.1 R-03).

FRP reinforcement is typically comprised of glass (GFRP), carbon (CFRP), or aramid (AFRP) continuous fibers embedded in a resin matrix. FRP reinforcement is commonly fabricated in the form of reinforcing bars and fabric. FRP rebar is used for typical concrete reinforcement in lieu of traditional steel rebar, while FRP fabric is

commonly externally bonded to concrete, masonry, and steel as a form of strengthening. The potential durability and corrosion resistance are the most significant benefits of FRP compared to steel. Other benefits include high tensile strengths, lightweight, and non-magnetic characteristics. As it is with all building materials, FRP also has certain disadvantages. Some of the common disadvantages include low modulus of elasticity, no yielding point before brittle rupture, high initial cost, and lack of familiarity within the industry. Due to FRP's low modulus of elasticity, deflection and crack width serviceability are greater than steel reinforcement and will commonly govern the design. Even though FRP has a high initial cost, the life cycle cost is potentially lower depending on the increase in service life. This research study primarily focused on crack control characteristics due to the low modulus of elasticity.

1.2. SCOPE AND OBJECTIVES

The primary objective of this study was to investigate the development of an empirical secondary reinforcement ratio for FRP based on experimental test data. Currently, ACI 440 "Guide for the Design and Construction of Concrete Reinforced with FRP Bars" requires in most applications a secondary reinforcement ratio that is significantly larger than the primary reinforcement ratio based on flexural requirements. Since no experimental data was available to develop the current FRP secondary reinforcement ratio for shrinkage and temperature, the ACI 440 guideline uses the ACI 318 secondary reinforcement ratio of 0.0018 for steel as a base value and incorporates the stiffness and strength of the FRP material into a secondary reinforcement ratio design equation. This design equation has no experimental validation and is considered to be

excessive by many experts. Similar to FRP, the current ACI 318 secondary reinforcement ratio for steel also has no experimental validation. Although, this required ratio of 0.0018 for Grade 60 steel is based on several decades of satisfactory performance in the field. Knowing that a ratio of 0.0018 has proven to be adequate for steel; an equivalent ratio for FRP that possessed similar crack control characteristics was desired. Since corrosion is not a concern for structures reinforced with FRP, crack width limitations are governed more by aesthetic appearance in lieu of durability, therefore one may argue that larger crack widths may be permissible in the field.

Currently, there is no standard test method to evaluate secondary reinforcement materials. The three phases developed in this study were examined to investigate both early-age and later-age effects of various reinforcement ratios on the formation of shrinkage/temperature cracks and flexural cracks for steel and GFRP reinforcement. These three phases include: Phase I – Early-age tensile test subjected to environmental conditions, Phase II – Later-age tensile test, and Phase III – Cracks control of panels tested in flexure. Only one bar manufacturer was selected for use in this study. Future tests will certainly need to investigate other bar manufactures to develop a large data-base of test results.

1.3. LAYOUT OF THE REPORT

Section 1 covers the project background including the significance of the study, as well as the scope and objectives.

Section 2 describes the significance of cracks and gives an overview of drying shrinkage, temperature, and plastic shrinkage crack formation. This section also includes

shrinkage reinforcement, ACI 318 code requirement for steel reinforcement, ACI 440 code recommendations for FRP reinforcement, and discusses previous research efforts relating to reinforcement crack control.

Section 3 describes the experimental program in terms of test program, test specimens, materials, test setup, and testing procedure. This section attempts to give a specific description of the test program so further research can easily build upon what has already been done.

Section 4 details the test results and discussion of the laboratory testing. The test results include concrete compressive strength, concrete flexural strength, reinforcing steel tensile strength, Phase I tests, Phase II tests, and Phase III tests.

Section 5 presents the test program conclusions and offers recommendations for future research.

The Appendices provide illustration of specimen crack patterns and additional graphs of specimen test results.

2. LITERATURE REVIEW

2.1. SIGNIFICANTS OF CRACKS

It is well known that concrete has good compressive strength characteristics with comparably low tensile strength characteristics. Small tensile stresses caused by plastic shrinkage, drying shrinkage, and/or changes in temperature can easily cause cracks to form. Controlling the width and pattern of cracks are important for two primary reasons. These include the aesthetic appearance and the durability performance of the structure.

In particular, bridge decks have been susceptible to corrosion of steel reinforcement due to exposure of deicing salts. For oxidation of the steel reinforcement to occur, oxygen and moisture must be present. Cracks provide a direct transport for these to ingress. Typically, when concrete is poured it has a pH value on the order of 13. The high alkalinity of the concrete creates a protective layer around the reinforcement bars preventing corrosion. The pH decreases as chloride ions from deicing salt penetrates the concrete. As chlorides neutralize the alkalinity of the protective layer, it becomes ineffective and the concrete adjacent to the reinforcing bars begins to corrode at pH values of 10 or 11 (MacGregor 1997). The less permeable and thicker the concrete cover is, the longer it will take the chloride ions, oxygen, and moisture to come in contact with the reinforcement bars. As cracks form in the concrete cover, the easier it is for agents to penetrate. Corrosion is more severe under wetting and drying cycles than structures that are fully submerged in the water (MacGregor 1997). For this reason, adequate drainage is important.

As previously mentioned, to prevent corrosion of the reinforcement it must be restricted from exposure to oxygen and moisture to prevent electron flow from the anode

to the cathode (Mindess et al. 2003). The most effective procedures include increasing the cover thickness, reducing the concrete permeability, placing a protective membrane over the concrete surface, and applying a protective surface coating on the steel. One of the best methods is to also eliminate crack potential since this is a direct path to local damage or deterioration.

Increasing the cover with high quality, impermeable concrete with a low water-to-cementitious (w/cm) ratio can greatly increase the durability by decreasing the penetration of chlorides, oxygen, and moisture. To prevent the penetration of deicing salts on bridge decks, protective membranes such as a layer of asphalt concrete at least two inches (49 mm) thick has been widely used. With properly installed drainage, the protective membrane can help prevent deicing salts from coming in direct contact with the upper concrete surface. Since the late 1970's, the use of epoxy-coated reinforcement has reduced the rate of deterioration of bridge decks in North America (Mindess et al. 2003). However, due to poor field handling and construction procedures it is nearly impossible to prevent or repair all chips in the epoxy coating (Dobrowolski 1998).

“In well-publicized cases, improperly applied epoxy has been shown to accelerate corrosion as the result of a process known as crevice corrosion, which involves the concentration of chloride ions and, thus, highly acidic conditions in regions with very limited oxygen availability (i.e., under the coating)” (Mindess et al. 2003).

Due to the limitations and problems associated with epoxy-coated reinforcement, research efforts in the 1990's started to examine nonmetallic reinforcing bars, such as GFRP. For secondary reinforcement, GFRP bars are selected in lieu of other types of FRP bars primarily due to cost.

Crack widths of 0.01 in. (0.3 mm) or smaller are generally not a significant concern to the public (Ghali and Favre 1994). However, when wider cracks develop it detracts for the structure visually and may cause the public to question its structural integrity. Crack width tolerances are dependent on factors such as crack spacing, length, position, illumination, surface texture, and the personal opinion of the observer. Wider cracks are more acceptable on surfaces that are dimly lit and on rougher surfaces since they are not as noticeable. Also, the aesthetic appearance of a structure is greatly tarnished when streaks of dirt or other leached material deposits and stains exposed surfaces. Cleaning the surface by sandblasting techniques usually makes smaller cracks much more noticeable.

2.2. CRACK FORMATION AND TYPES

Mitigation or even prevention of cracking in concrete bridge decks is of high concern for preventing deterioration and conserving its service life. Volume changes in concrete due to shrinkage and temperature changes alone can produce tensile stresses that are large enough to produce cracks if subjected to some degree of restraint. Dimensional changes of concrete that is free to move without external and internal restraint produce minimal stresses that results in no damage. However, if the concrete is subjected to any sufficient restraint while experiencing volume changes, as the stresses increase cracking is possible. The three main types of cracks due to volume change include drying shrinkage cracks, temperature cracks, and plastic shrinkage cracks. These are discussed in further detail later in this section.

2.2.1. Crack Formation. As previously mentioned, for concrete to crack from dimensional changes some degree of restraint must be present. With the combination of restraint and shrinkage tensile stresses are produced. Once the tensile stress reaches and exceeds the ultimate tensile strength of the concrete, a crack is formed. As illustrated in Figure 2.1, the unrestrained concrete is allowed to shrink without any cracks produced, although the restrained concrete develops tensile stresses greater than the ultimate tensile strength of the concrete and cracks are produced. Restraints can also be developed by the difference in the amount of shrinkage that takes place at the exposed surface compared to the interior of the concrete. Since the shrinkage at the outer surface is always greater than the interior of the member, the interior portion restrains the shrinkage of the outer surface producing tensile stress in the member (ACI Committee 224-89). This type of restraint usually results in initial surface cracking which later penetrates further into the member as the interior continues to dry. The concrete modulus of elasticity, amount of shrinkage, and the degree of restraint are primary factors that determine the magnitude of tensile stress developed. As the concrete shrinks with restraint, it is equivalent to applying an axial tensile force at each restraint. As Figure 2.2 illustrates, the tensile stress (f_{ct}) caused by the tensile force from the restraint has exceeded the tensile capacity of the concrete. At this crack location, the stress in the member is zero and all the axial force is transferred to the reinforcement. The symbol S_{r0} denotes the distance between the first crack and the cross-section where the stress has increased to f_{ct} . Any increase in load will cause the formation of a second and third crack on each side a distance S_{r0} from the first.

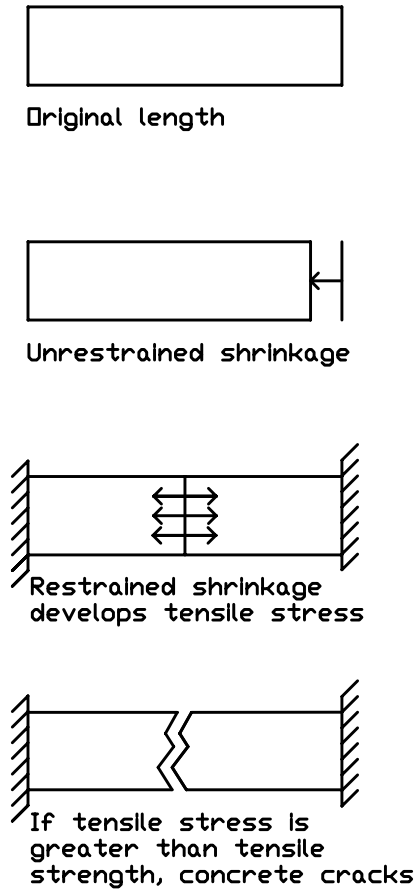


Figure 2.1. Cracking of Concrete Due to Volume Change and Restraint (ACI Committee 224-89)

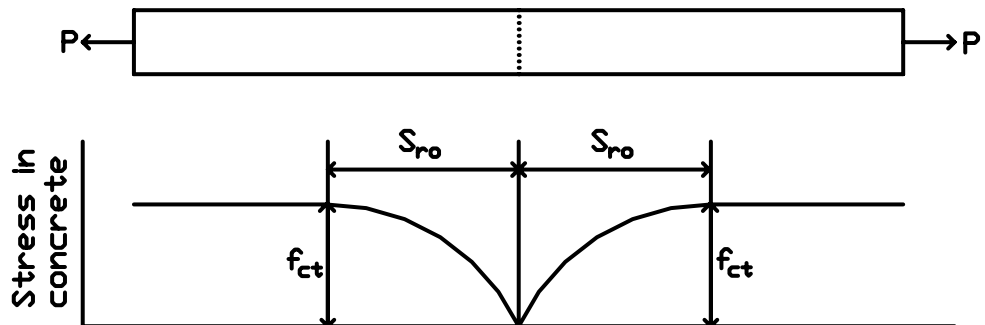


Figure 2.2. Stress in Concrete After First Crack in a Member Subjected to Axial Force (Ghali and Favre 1994)

2.2.2. Drying Shrinkage Cracks. It is well known that as concrete dries it shrinks and as it is rewetted it expands. Typically after curing, concrete bridge decks lose some original mix water to the environment due to evaporation. During this process, longitudinal beams restrain the shrinkage which causes full depth transverse cracks in the deck to form (Babaei and Fouladgar 1997). Inadequate allowances in the concrete design and construction for the effects of drying shrinkage and rewetting expansion can lead to excessive cracking or warping of the member. One important aspect with drying shrinkage of cement paste and the concrete is the fact that the first part of drying, which contributes to the total shrinkage, is irreversible (see Figure 2.3) (Mindess et al. 2003).

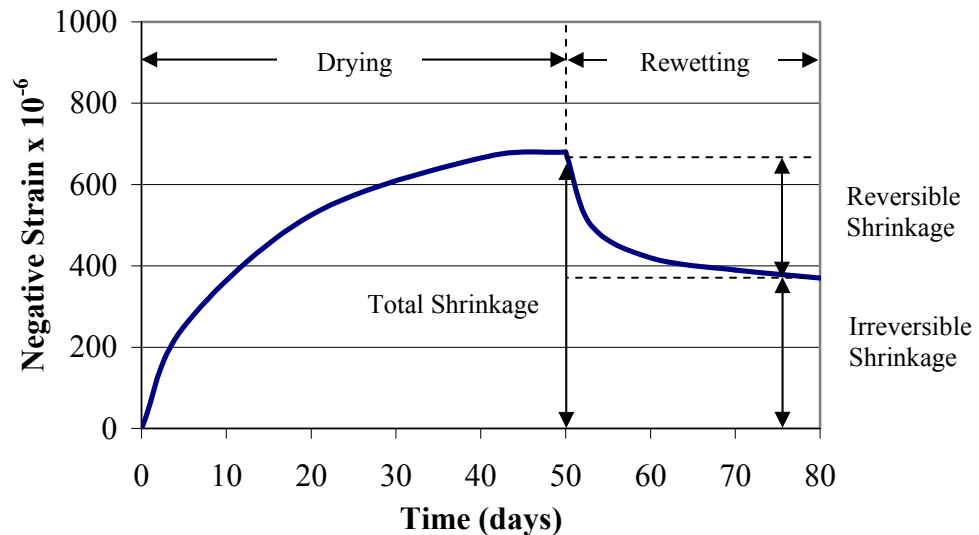


Figure 2.3. Typical Drying and Rewetting Behavior of Concrete (Mindess et al. 2003)

The volume change due to the change in moisture content is a characteristic of hydraulic cement concretes. The shrinkage and swelling of concrete is due to changes in

the moisture content of the concrete paste, while the aggregate provides internal restraint, which contributes to significantly less changes in overall volume (ACI Committee 224-89). During the process of hydration when cement is mixed with water, large amounts of hardened calcium silicate gel are produced. Within the hardened paste, a majority of the water is in the calcium silicate gel with some in the capillary pores. Drying shrinkage is mostly due to the loss of the absorbed water layer on the surface of the gel particles. This layer is approximately one water molecule thick or about 1% the size of the gel particles (MacGregor 1997). Initially, the first loss of water which comes from the larger capillary pores in the concrete paste result in very little, if any, shrinkage. The loss of the inter-layer of water from the hydrated calcium silicate gel is the source of significant paste shrinkage (ACI Committee 224-89). During dry conditions, internal moisture gradually diffuses to the surface and evaporates whereas during wet conditions the process is reversed causing concrete expansion.

Factors that influence drying shrinkage cracks: The primary factors that influence drying shrinkage include cement composition, aggregate type, water content, and the mix proportions. Other factors that affect drying shrinkage are quality of paste, characteristics and amounts of admixtures used, maximum aggregate size, size and shape of the concrete mass (surface to volume ratio), amount and distribution of reinforcing steel, curing conditions, humidity, and length of drying period.

From previous studies, we are not able to say that a particular type of cement, because it meets the requirements of one of the standard cement types, will have more or less shrinkage than another type of cement that meets the requirements of a different type (ACI Committee 224-89). Usually, lower shrinkage is associated with lower C_3A/SO_3

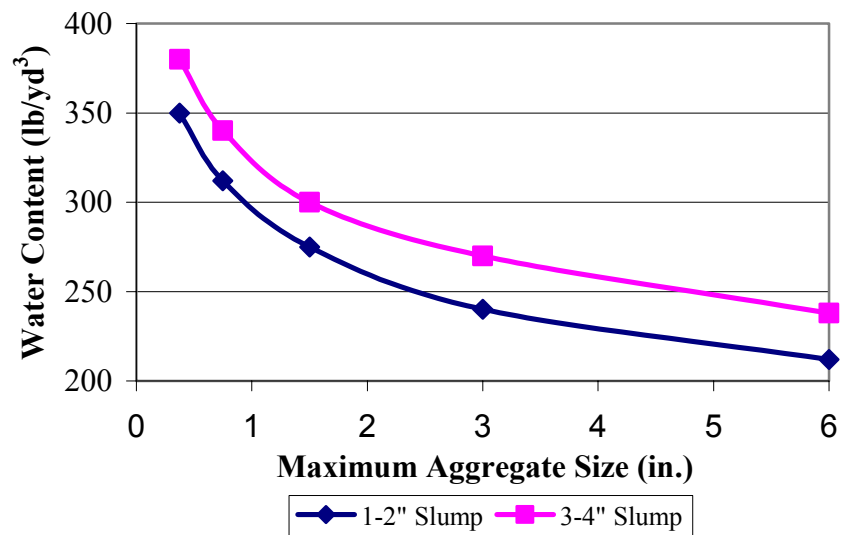
ratios, lower Na_2O and K_2O contents, and higher C_4AF amounts in the cement (ACI Committee 224-89). Initially, Type II cement generally shrinks less than Type I, but after curing for 28 days the amount of total shrinkage is approximately the same. Even though the difference is not large, it can be noted that the finer cements usually result in greater concrete shrinkage.

Coarse and fine aggregate can have a significant influence on shrinkage since these materials occupy between 65 and 75 percent of concrete's total volume. Compressibility of the aggregate and extensibility of paste, paste-aggregate bond, cement paste degree of cracking, and contraction of aggregate due to drying are the major factors that influence aggregates ability to restrain shrinkage (ACI Committee 224-89). Aggregate with a high stiffness or modulus of elasticity having rougher surfaces are more effective in reducing the amount of concrete shrinkage. Generally, aggregates with a low modulus of elasticity are usually associated with high absorption. As Table 2.1 indicates the amount of 1-year concrete shrinkage increases as the aggregate absorption increases. Quartz, limestone, dolomite, granite, feldspar, and some basalts are generally classified as low shrinkage aggregates, while sandstone, slate, hornblende and some other types of basalts are classified as high shrinkage aggregates (ACI Committee 224-89). The maximum aggregate size is also important to reducing shrinkage. As the maximum aggregate size increases, it helps to resist cement paste shrinkage that allows less water (see Figure 2.4). As the maximum aggregate size increases, the total surface area decreases resulting in less required paste and water to properly coat it. Well-graded gradations are desired to avoid over-sanding of the mix design to obtain the required

workability. Unwashed coarse aggregates and dirty sands containing high amounts of expansive clay can also contribute to drying shrinkage.

Table 2.1. Effect of Aggregate Type on Concrete Shrinkage (ACI Committee 224-89)

Aggregate	Specific Gravity	Absorption (%)	1-Year Shrinkage (%)
Sandstone	2.47	5.0	0.116
Slate	2.75	1.3	0.068
Granite	2.67	0.8	0.047
Limestone	2.74	0.2	0.041
Quartz	2.66	0.3	0.032



Conversion Units: 1 lb/yd³ = 0.593 kg/m³, 1 in. = 25.4 mm

Figure 2.4. Effect of Aggregate Size on Water Requirement of Non-AE Concrete (ACI Committee 224-89)

The water content of a concrete mix is a very important factor influencing drying shrinkage: as water content increases, shrinkage increases. A typical relationship between drying shrinkage and water content is shown in Figure 2.5. An increase in water content also reduces the amount of restraining aggregates thus increasing shrinkage. By increasing the total aggregate volume while minimizing the paste water content lowers the water amount per unit volume; resulting in less drying shrinkage. Previous research indicates that the cement factor has little effect on shrinkage of concrete as long as the water content remains constant (ACI Committee 224-89). Also illustrated in Figure 2.4 is the effect of slump on water content requirement. For example, the required water content of concrete made with 1 in. (25.4 mm) maximum aggregate size is 320 lb/yd³ (190 kg/m³) for a 3 to 4 in. (75 to 100 mm) slump, but only 295 lb/yd³ (175 kg/m³) for a 1 to 2 in. (25 to 50 mm) slump. Another factor that affects the water requirement, and thus total shrinkage, is the temperature of fresh concrete to maintain a given slump (see Figure 2.6). For example, to maintain a given slump, the water content must be increased from 285 to 300 lb/yd³ (169 to 178 kg/m³) if the concrete temperature increases from 70 to 90° F (21 to 32° C). These two examples both demonstrate a substantial reduction in water content that would result in less drying shrinkage. A certain amount of water is required for hydration, workability, finishability, but any excessive water that is present for placing and finishing convenience will result in more shrinkage cracking than is necessary (Fricks 1992).

Chemical admixtures such as air-entraining agents, water-reducers, retarding agents, and accelerators are commonly used to achieve certain desirable concrete properties. When drying shrinkage is of high concern, admixtures should be used with

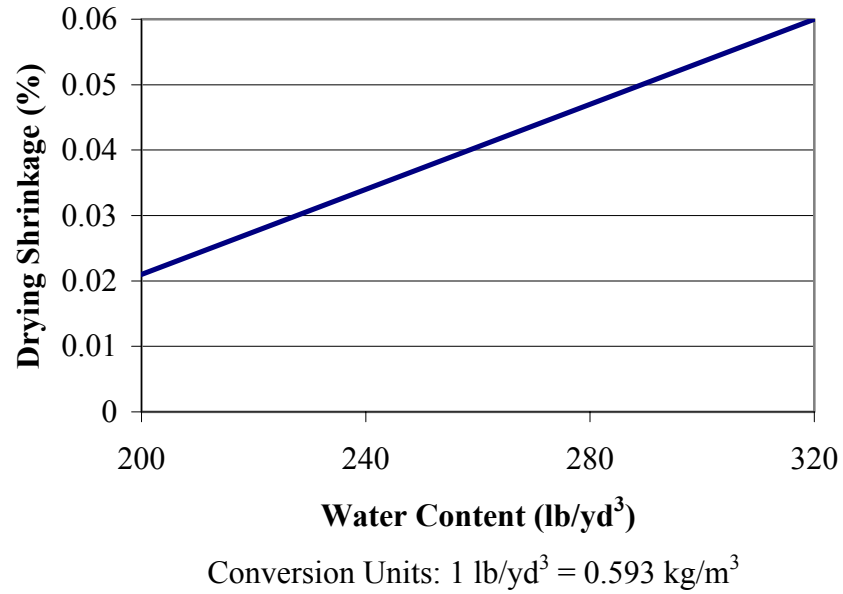


Figure 2.5. Typical Effect of Concrete Water Content on Drying Shrinkage (ACI Committee 224-89)

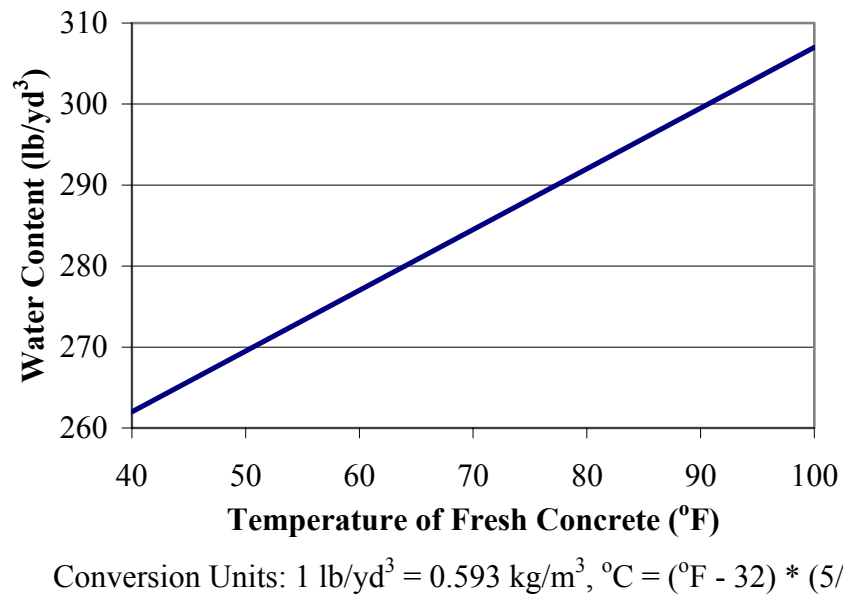


Figure 2.6. Effect of Fresh Concrete Temperature on Water Content for a Given Slump (ACI Committee 224-89)

care since their effects on drying shrinkage are variable. Since air-entraining agents increase the percentage of air, one would expect an increase in drying shrinkage; however, since it allows a reduction in water content to maintain the same slump, the shrinkage is not appreciably affected by air content up to five percent (ACI Committee 224-89). Some air-entraining agents contain accelerators to offset their retarding characteristics that can increase drying shrinkage up to ten percent. Accelerators containing calcium chloride have been found to greatly increase both early-age and later-age shrinkage by up to 40 percent. Water-reducers and retarding agents commonly allow a reduction in water content but usually will not decrease drying shrinkage (ACI Committee 224-89). In fact, some can actually increase early-age drying shrinkage, but commonly later-age shrinkage is similar to mixes without admixtures. The use of pozzolan replacement and addition can increase the drying shrinkage of concrete, especially if the water demand increases. It has also been observed that drying shrinkage can be increased with the use of pozzolans even if the water demand does not increase (ACI Committee 224-89).

2.2.3. Temperature Cracks. During the curing process, the temperature of concrete increases due to the hydration process. Initially when the concrete temperature is increasing and expanding, no residual compressive stresses are produced during this “plastic-to-hardened” state since the concrete has an extremely low modulus of elasticity (Babaei and Fouladgar 1997). Heat of hydration usually causes minimal problems for slabs since the heat is able to dissipate rapidly due to their high surface area to volume ratio. When the concrete has reached its peak hydration temperature, it has reached its hardened state. After this peak temperature is reached, the concrete begins to cool and

approach the ambient temperature. Due to restraints, as the concrete cools and contracts, high tensile stresses can result in cracking. Once cracking occurs, the thermal restraint gradually dissipates and the stresses are relieved. For many bridge decks, the longitudinal bridge girders restrain the deck shrinkage induced by cooling, which in turn causes tensile stresses and may result in transverse cracking in the deck. These temperature cracks are usually full-depth and form above the uppermost transverse bars. The amount of restrained temperature shrinkage in a bridge deck depends on the difference between the peak concrete temperature and the temperature of the supporting beams at the time of the peak temperature (Babaei and Fouladgar 1997).

Factors that influence temperature cracks: Bridge decks are exposed to an environment which is continuously losing and gaining heat from convection, solar radiation, and re-radiation to or from the surrounding air (Ghali and Favre 1994). During hot summer days, heat gain is greater than heat loss causing an increase in temperature. During the winter night, the opposite occurs causing a decrease in temperature. Figure 2.7 is a schematic representation of heat transfer during a summer day for a bridge deck. As shown, some of the incident solar radiation is absorbed while the rest is reflected. A temperature gradient through the deck is produced when the bridge deck absorbs the heat and the temperature increases. Differential temperature gradients at night may cause the deck surface to shorten with respect to the bottom surface, tending to lift the slab ends above the sub-grade, decreasing the ability of the slab to support traffic loads without cracking (Dobrowolski 1998). Large enough temperature gradients (above 30° F or 16.7° C) can cause excessive curling or bending of the concrete slab.

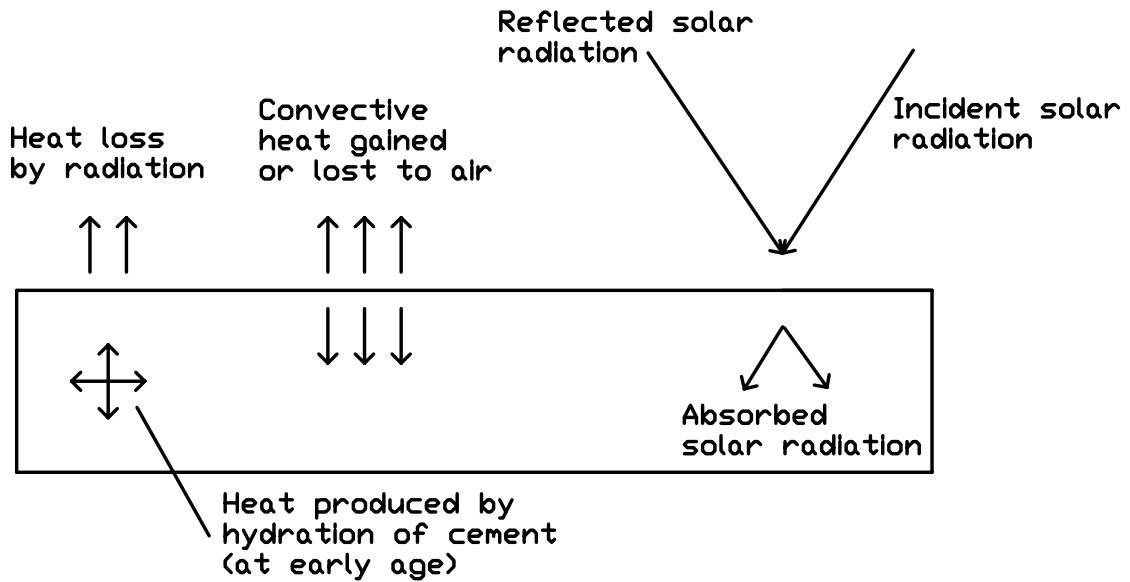


Figure 2.7. Heat Transfer Processes for a Bridge Deck During a Summer Day (Ghali and Favre 1994)

A typical positive and negative thermal gradient for a standard bridge system measured in Missouri is illustrated in Figure 2.8. As shown, these thermal gradients can be significant. The temperature difference between the surface of the deck and the bottom of the girder for this particular bridge is 36 °F (20 °C) for the positive gradient and 9 °F (5 °C) for the negative gradient. These thermal gradients alone are capable of causing stresses large enough to produce thermal related cracks if not considered in design. Figure 2.9 illustrates the thermal stresses for a MoDOT Type III pre-stressed concrete girder. The figure plots distance from bottom of member vs. stress for positive and negative gradients both restrained and unrestrained. As illustrated, the level of restraint can significantly affect the thermal related stresses that develop in a bridge cross-section.

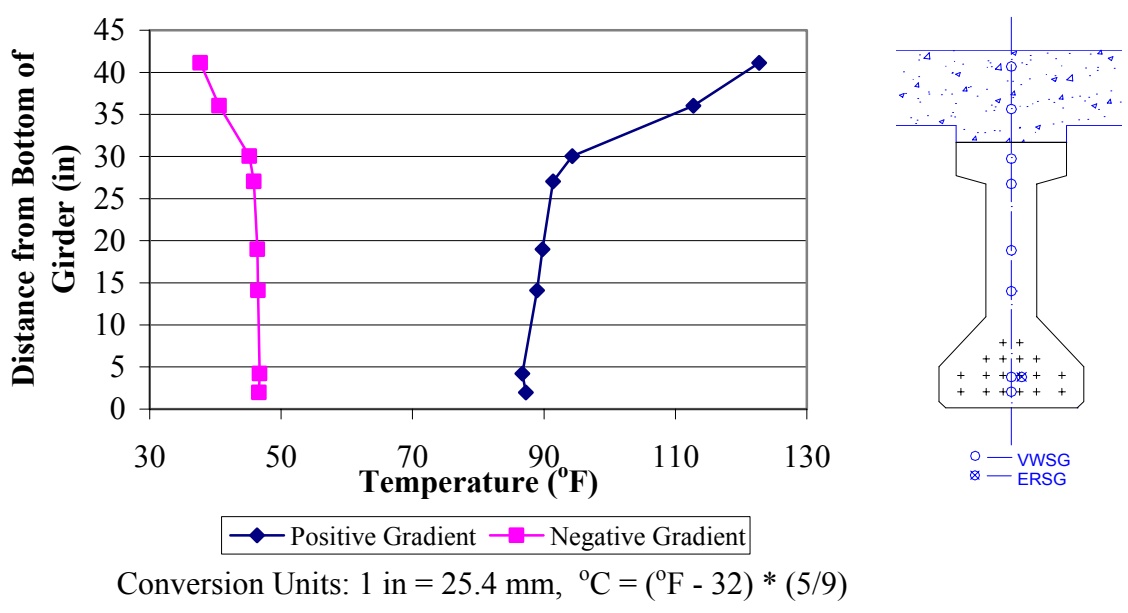


Figure 2.8. Typical Thermal Gradient for a Standard Bridge System in Missouri (Yang and Myers 2003)

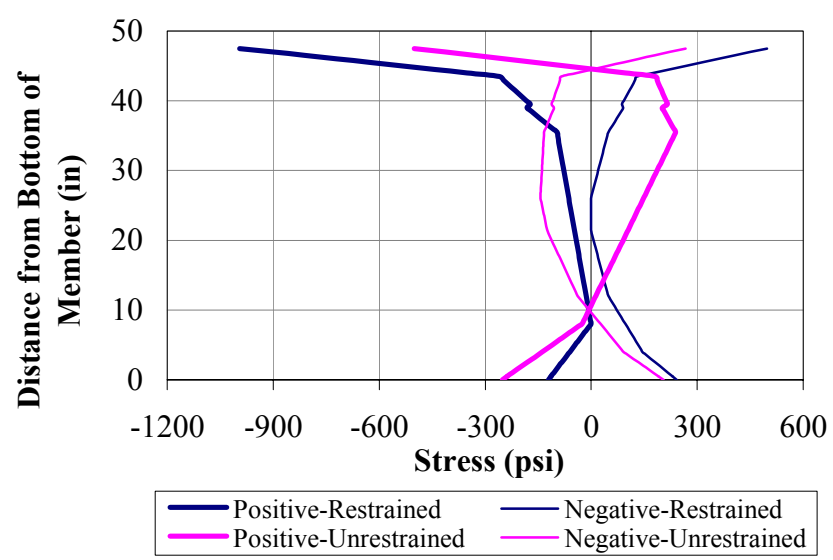


Figure 2.9. Thermal Stressed for a MoDOT Type III Girder (Myers et al. 2001)

The temperature distribution of a bridge cross-section varies with time and depends on the following variables (Ghali and Favre 1994):

1. Geometry of the cross-section
2. Thermal conductivity, specific heat and density of the material
3. Nature and color of the exposed surfaces, expressed in terms of solar radiation absorptivity, emissivity, and convection coefficients
4. Orientation of the bridge axis, location latitude and altitude
5. The season and time of the day
6. Variation of ambient air temperature and wind velocity
7. Degree of cloudiness and turbidity of the atmosphere

Concrete thermal expansion is greatly influenced by aggregate type and thermal properties since it makes up 65 – 75% of the total volume. An average thermal coefficient of expansion of plain concrete is roughly 0.055% per 100° F (0.100% per 100° C) (Portland 1982) Thus, for a 100 ft section that experiences a temperature change of 100° F will experience a length change of 0.66 in. (or 5 mm for a 10-m-long section with a 50° C temperature change). Of course, this average does not apply to all types of concrete. Table 2.2 shows some concrete thermal coefficient of expansions made with various aggregates based on laboratory experimentation. The concrete coefficient of thermal expansion (CTE) varies greatly due to the changes in the thermal coefficient of the aggregate as shown in Table 2.3. The primary factor influencing the thermal expansion of aggregate, and therefore of concrete, is the proportion of quartz (Portland 1982). The higher the quartz contents, the higher the coefficient. Siliceous aggregates such as chert, quartzite, and sandstone have higher thermal coefficients between 4.5 and

6.5 millionths per degree Fahrenheit (2.5 and 3.6 millionths per degree Celsius), while the coefficients for pure limestone, basalt, granite, and gneiss may vary between 1.2 and 4.5 millionths per degree Fahrenheit (0.7 and 2.5 millionths per degree Celsius) (Dobrowolski 1998).

2.2.4. Plastic Shrinkage Cracks. The extreme environmental conditions in hot arid regions greatly influence the properties of fresh concrete or concrete in the plastic state. Plastic shrinkage cracking is the predominate problem with fresh concrete under dry arid environmental conditions. These cracks of random patterns and lengths leave an unsightly appearance on the concrete surface and are difficult to repair. Plastic shrinkage cracks are commonly wide at the surface but only a few inches in depth, a few inches to a few feet in length, spaced a few inches to two feet apart, discontinuous, and are usually perpendicular to the wind (ACI Committee 224-89 and Dobrowolski 1998). These cracks provide paths for moisture and oxygen to penetrate the concrete that promote reinforcement corrosion and concrete deterioration which decreases service life.

Table 2.2. Thermal Coefficient of Expansion of Concrete Depending on Aggregate Type (Portland 1982)

Aggregate type (from one source)	Coefficient, %	
	Per 100° F	Per 100° C
Quartz	0.006	0.119
Sandstone	0.065	0.117
Gravel	0.060	0.108
Granite	0.053	0.095
Basalt	0.048	0.086
Limestone	0.038	0.068

Table 2.3. Aggregate Coefficient of Thermal Expansion Range (Portland 1982)

Aggregate Type	Coefficient, %	
	Per 100° F	Per 100° C
Marble	0.006 – 0.009	0.011 – 0.160
Gravel, chert	0.041 – 0.073	0.074 – 0.131
Quartzite	0.073	0.131
Gravel	0.059 – 0.071	0.106 – 0.128
Sands	0.060 – 0.070	0.108 – 0.126
Granite	0.010 – 0.066	0.018 – 0.119
Sandstone	0.066	0.119
Limestone	0.019 – 0.064	0.034 – 0.115
Slag	0.051	0.092
Traprock	0.043 – 0.047	0.077 – 0.085
Basalt	0.045	0.081

Soon after placement and before curing when concrete still remains in a plastic state, an excessive loss of water can cause cracking. Plastic shrinkage cracks form when water evaporates from the fresh concrete faster than the concrete can bleed or water can rise naturally to the surface. The most common source of water loss is due to excessive evaporation at the surface, but absorption from the formwork or subbase also contributes to the water loss. In fresh concrete, the vacant spaces between particles are filled with water. As this water is removed from the paste by exterior influences, such as evaporation, a series of complex menisci are formed producing negative capillary pressures that cause the paste volume to contract. The negative capillary pressure within the paste continues to increase until a critical “breakthrough” pressure is reached (Mindess et al. 2003). At this point the water is no longer evenly distributed throughout

the paste matrix and rearranges to form discrete zones of water with void in between (Mindess et al. 2003). Just prior to the “breakthrough” pressure is when the maximum rate of plastic shrinkage occurs. Typically, freshly placed concrete has not developed enough tensile strength to resist the contracting stresses induced by the capillary pressure resulting cracks.

Factors that influence plastic shrinkage cracks: Plastic shrinkage cracking is usually associated with hot weather, but it can occur at any time when the environmental conditions results in extreme evaporation rates that exceeds 0.2 lb per square foot per hour (1 kg/m²/hr). Depending on concrete properties, cracking is possible if the evaporation rate exceeds 0.1 lb per square foot per hour (0.5 kg/m²/hr). Factors that increase the evaporation rate and the potential for plastic shrinkage cracking are high concrete temperatures, high ambient temperatures, higher air temperatures than concrete temperatures, low relative humidity, and high wind velocity. The following are important precautions to minimize the evaporation rate and the potential for plastic shrinkage cracking (Babaei and Fouladgar 1997 and Portland 1982).

1. Keep aggregate cool by shading
2. Moisten aggregates if dry or absorptive
3. Use cold mix water, possible ice replacement if necessary
4. Moisten forms and subgrade
5. Erect temporary wind breakers to reduce wind velocity
6. Erect temporary sunshades to lower the surface concrete temperature
7. Place concrete at lower temperature, such as night

8. Minimize evaporation by using fog (not spray) nozzles to maintain a sheen of moisture between time of placement and start of curing
9. Cure concrete promptly after placement
10. Use suitable curing material such as curing compound, wet burlap, plastic sheeting, or curing paper

“Plastic cracking cannot be controlled by provision of reinforcement; it can only be achieved by attention to mix design and avoidance of conditions which produce rapid drying during the first hour after placement” (Ghali and Favre 1994). Concretes that contain admixture that reduce the rate of bleeding are extremely susceptible to plastic shrinkage cracking. For high-strength concrete, the use of silica fume can increase plastic shrinkage cracking by increasing the free plastic shrinkage strain, acceleration the setting rate and reducing the bleeding of concrete (Soroushian and Ravanbakhsh 1998).

2.3. SHRINKAGE REINFORCEMENT

Concrete cracking is best controlled during the design and construction phases. In many cases, with the proper selection of materials, cracking may be avoided, provided that the anticipated expected environmental conditions are taken into account. Most cracks are caused by high tensile stresses due to internal or external restraints produced by shrinkage or temperature differentials (Leonhardt 1977). The stresses caused by temperature are much more important than most engineers are aware of. As many engineers believe, cracks can not be prevented by reinforcement. In fact, the restraint added by the reinforcement can actually encourage cracking, but the bond along the reinforcing bars distributes the concrete shrinkage strain which produce several fine

cracks instead of a few wide ones (Portland 1982). The finer the crack width, the less likely it is to contribute to durability problems. The ACI Code limits on crack control are based on a maximum width of 0.016 in. (0.41 mm) for interior exposure and 0.013 in. (0.33 mm) for exterior exposure (MacGregor 1997). Larger crack widths are tolerable for bridge deck systems reinforced entirely with FRP rebar since corrosion is not a concern. According to ACI 224R-89 Code (Control of Cracking in Concrete Structures), Table 2.4 gives the tolerable crack widths at the tensile face of reinforced concrete structures for the listed exposure condition that should be used during the design process.

Table 2.4. Tolerable Crack Widths for Reinforced Concrete (ACI Committee 224-89)

Exposure Condition	Tolerable Crack Width	
	(in.)	(mm.)
Dry air or protective membrane	0.016	0.41
Humidity, moist air, soil	0.012	0.30
Deicing chemicals	0.007	0.18
Seawater and seawater spray; wetting and drying	0.006	0.15
Water retaining structures	0.004	0.10

Limiting the concrete cover, using smaller bars with closer spacing, and designing at smaller service stress levels are common methods of controlling cracks during the design phase. The use of joints is the most effective method of preventing the formation of unsightly cracking. Saw-cut groove joints, “engineered cracks”, are commonly used in slabs, pavements, and floors to create a weakened plane to relieve tension to

predetermine the location and spacing of cracks. Bridge decks usually have expansion joints that allow longitudinal movement due to expansion and contraction in the direction of the bridge axis.

As concrete shrinks, an axial tensile restraining force develops and produces the first crack once the tensile capacity of the member has been exceeded. If no longitudinal steel is present, an unsightly wide crack forms causing the restraining force to drop to zero. If a small quantity of reinforcement is present, the steel yields at the crack and also opens widely. The restraining force drops to $A_s f_y$, which may be only a small fraction of what it was prior to cracking. If a large quantity of reinforcement is present, the steel at the crack does not yield, the crack remains small because the loss of member stiffness at cracking is not great, and the restraining force remains high (Gilbert 1992). Members with a large amount of steel will eventually suffer many cracks that are fine and well controlled. Figure 2.10 illustrates the reinforcement behavior of concrete undergoing expansion and contraction. Crack widths depend on the quantity of steel reinforcement, size and distribution of bars, bond between steel and concrete, concrete quality, and degree of restraint (Gilbert 1992).

Shrinkage can have the same effect on deflection as creep. If a concrete member contains no reinforcement, then it is allowed to shrink or shorten in all directions without causing any curvature. However, if reinforcement is present then the shrinkage is restrained from the bond between the concrete and the rebar creating the potential for deflection. “Thus, a singly reinforced beam, having its shrinkage restrained at the reinforced face and unrestrained at the unreinforced face, will have considerable curvature” (Wang 1998). Commonly, it is difficult to determine whether curvature is the

result of shrinkage or creep. Although, 90% of shrinkage occurs within the first year while it can take up to five years for 90% of the creep to occur (Wang and Salmon 1998).

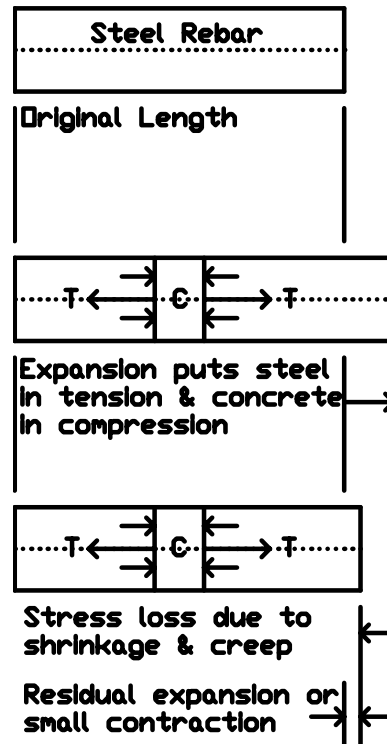


Figure 2.10. Reinforcement Behavior for Concrete Expansion and Contraction (ACI Committee 224-89)

2.3.1 ACI 318 Code Requirements for Mild Steel. Section 7.12, Shrinkage and Temperature Reinforcement, of the current ACI 318 Building Code Requirements for Structural Concrete using mild steel states “reinforcement for shrinkage and temperature stresses normal to flexural reinforcement shall be provided in structural slabs where the flexural reinforcement extends in one direction only” (ACI Committee 318-02). This secondary reinforcement is placed at right angles to the principal reinforcement to

prevent harmful cracking due to volume change and to maintain the full continuity of the structure. Also, ACI 318 requires that bar spacing should not exceed five times the member thickness or 18 in. (460 mm). As stated in the ACI 318 Code dating back to the 1963 edition, “The amount specified are empirical but have been used satisfactorily for many years” (ACI Committee 318-63). The following are the current shrinkage and temperature reinforcement requirements as stated in Chapter Seven of ACI 318-02.

7.12.2.1 – Area of shrinkage and temperature reinforcement shall provide at least the following ratio of reinforcement area to gross concrete area, but not less than 0.0014;

(a) Slabs where Grade 40 or 50 deformed bars are used	0.0020
(b) Slabs where Grade 60 deformed bars or welded wire fabric (plain or deformed) are used	0.0018
(c) Slab where reinforcement with yield stress exceeding 60,000 psi (414 MPa) measured at a yield strain of 0.35 percent is used	$\frac{0.0015 \times 60,000}{f_y}$

2.3.2 ACI 440 Code Recommendations for FRP. Chapter Ten, Temperature and Shrinkage Reinforcement, of the current ACI 440 “Guide for the Design and Construction of Concrete Reinforced with FRP Bars” states the guidelines for secondary reinforcement when FRP bars are used. Since no experimental research is available to determine an appropriate minimum FRP reinforcement ratio for shrinkage and temperature, the ACI 440 guideline uses the ACI 318 minimum reinforcement ratio of 0.0018 for steel as a base value and incorporates the stiffness and strength of the FRP

material into a FRP minimum reinforcement ratio design equation. The design tensile strength of FRP is much larger than steel, yet the modulus of elasticity (stiffness) of FRP is much less than steel. The following are the current temperature and shrinkage reinforcement requirements as stated in chapter ten of ACI 440-03.

$$\rho_{f,ts} = 0.0018 \times \frac{60,000}{f_{fu}} \frac{E_s}{E_f} \leq 0.0036 \quad (\text{Equation 2-1})$$

Equation 10-1 (ACI Committee 440-03)

“Due to limited experience, it is recommended that the ratio of temperature and shrinkage reinforcement given by Eq. (10-1) be taken not less than 0.0014, the minimum value specified by ACI 318 for steel shrinkage and temperature reinforcement. Spacing of shrinkage and temperature FRP reinforcement should not exceed three times the slab thickness or 12 inches (300 mm), whichever is less” (ACI Committee 440-03).

Table 2.5 summarizes an analysis of the ACI 440-03 secondary reinforcement ratio for the GFRP rebar used in this study. As shown in the table, the calculated reinforcement ratios ranging from 0.0044 to 0.0055 are significantly larger than 0.0018 which is required for steel; approximately 2.5 to 3 times larger. For this reason, ACI 440-03 set the maximum secondary reinforcement ratio to be 0.0036. If stiffness alone was used to determine an equivalent reinforcement ratio, 4.9 times more GFRP reinforcement would be required compared to steel reinforcement. Recognizing that a secondary reinforcement ratio of 0.0088 is extremely excessive, the ratio of steel to FRP tensile strength was placed in Equation 2-1. This tensile strength ratio was merely applied to reduce the significance of the stiffness ratio.

Table 2.5. ACI 440-03 Secondary Reinforcement Ratio Analysis

Bar No.	f_{tu} (psi)	E_f (psi)	E_s (psi)	$\rho_{f,ts}$ (Eq. 2-1)	$\frac{E_s}{E_f}$	$(0.0018)\frac{E_s}{E_f}$
2	120,000	5.92×10^6	29×10^6	0.0044	4.9	0.0088
3	110,000	5.92×10^6	29×10^6	0.0048	4.9	0.0088
4	100,000	5.92×10^6	29×10^6	0.0053	4.9	0.0088
5	95,000	5.92×10^6	29×10^6	0.0055	4.9	0.0088

2.4. PREVIOUS RESEARCH

After an extensive literature search, minimal research regarding temperature and drying shrinkage reinforcement was discovered. Although, several papers covering crack control in terms of flexural loading and plastic shrinkage were found. A majority of previous research regarding plastic shrinkage cracks focused on the effects of mix design, concrete temperature, air temperature, relative humidity, wind velocity, and fiber reinforcement.

Over the past 40 plus years, the ACI 318 code requirements for temperature and shrinkage cracks are based on empirical field experience instead of experimental test results. Apparently, since the requirements for steel performed well in the field for several decades, it was never necessary to support the code requirements with laboratory testing. A long time prior to 1963, ACI had recommended a steel reinforcement ratio of 0.0025 for plain bars. The requirements for temperature and shrinkage in the 1963 code still required a reinforcement ratio of 0.0025 for plain bars, yet the required ratio for deformed bars lowered to 0.0020 when $f_y < 60,000$ psi (414 MPa) and 0.0018 when $f_y >$

60,000 psi (414 MPa). This change gave benefit for increased yield strength and the use of deformed bars that possessed better bond characteristics.

In efforts to reduce the width, length, and amount of plastic shrinkage cracks in concrete slabs, considerable research on fiber reinforced concrete (FRC) has been performed. The different types of fibers studied include steel, polyolefin, polypropylene, cellulose, etc. The fiber lengths range from 0.5 to 2.0 in. (12 to 51 mm) with average diameters between 0.006 and 0.02 in. (0.15 and 0.50 mm). Typically, the amount of fibers mixed into the fresh concrete extends between 0.05 to 0.7% by volume. Previous research indicates a reduction in plastic shrinkage crack area for fiber reinforced concrete slabs compared to unreinforced control slabs.

As previously mentioned, there have been several research programs that have addressed crack control for reinforced concrete exposed to flexural loading. Common equations have been developed to calculate crack width, crack spacing, and required rebar spacing to prevent cracks of a desired width. The statistical evaluation of experimental crack data performed by Gergely and Lutz is probably the most well known. Gergely and Lutz used test results from Hognestad, Kaar and Mattock, Kaar and Hognestad, Clark, and Rusch and Rehm to develop the Gergely-Lutz equation (see Equation 2-2) to calculate crack widths at the tensile surface. It should be noted that within this experimental evaluation, the maximum concrete cover d_c tested was only 3.31 in. (84 mm) and only three specimens had clear covers greater than 2.5 in. (64 mm) (Frosch 1999). Noticing this, Frosch investigated crack control for specimens with larger concrete covers and based on a physical model Equation 2-3 was developed to predict the maximum crack width of uncoated reinforcement.

$$w = 0.076\beta f_s \sqrt[3]{d_c A} \quad (\text{Equation 2-2})$$

Equation 9-7 (MacGregor 1997)

$$w_c = 2 \frac{f_s}{E_s} \beta \sqrt{d_c^2 + \left(\frac{s}{2}\right)^2} \quad (\text{Equation 2-3})$$

Equation 6 (Frosch 1999)

3. EXPERIMENTAL PROGRAM

This section provides details of the experimental program. These details include: description of test specimens, form development, mix procedure, concrete placement and finishing, curing procedure, concrete and reinforcement properties, test setups, and procedures. All specimens were cast and tested in the High-Bay Structural Engineering Research Laboratory (SERL) at UMR. Additional details will be provided throughout this section to aid in any future research on the same or similar topic.

3.1. TEST PROGRAM

As previously mentioned in Section One, the objective of this research was to develop a recommendation for the amount of GFRP secondary reinforcement needed to adequately provide shrinkage and temperature crack control. Knowing that the ACI 318 required secondary reinforcement ratio of 0.0018 has adequately worked in the field for steel, finding an equivalent ratio for GFRP with similar crack control characteristic was desired.

Selection of Test Variables: The following are several variables that could affect the crack control capabilities of different types of reinforcement.

- Reinforcement properties (tensile strength, modulus of elasticity, deformation pattern, bond, etc.)
- Reinforcement ratio ($\rho = A_s/bh$)
- Reinforcement bar size
- Reinforcement bar spacing

- Concrete strength
- Concrete age (early/late)
- Concrete cover
- Concrete/reinforcement bond
- Environmental conditions

For this study, four of these variables were implemented in the experimentation.

They were reinforcement ratio, reinforcement bar size, concrete age, and various environmental conditions. The rebar manufacturer, concrete strength, and cover distance remained constant for all specimens of the same phase. With the variables taken into account, the laboratory testing was separated into three distinctive phases to gain the best understanding of secondary reinforcement for steel and GFRP rebar. These three phases of study included: Phase I – Early-age tensile test subjected to environmental conditions, Phase II – Later-age tensile test, and Phase III – Cracks control of panels tested in flexure. The following three tables (Table 3.1, Table 3.2, and Table 3.3) list the testing program matrixes for the three phases of this project. Further specimen and reinforcement properties are provided later in this section.

Table 3.1. Phase I Test Program Matrix

Specimen ID (Phase – Specimen #)	Reinforcement (#/Specimen – Bar Type)
I-1	2 - #3 Steel Rebar
I-2	2 - #3 GFRP Rebar
I-3	3 - #3 GFRP Rebar
I-4	4 - #3 GFRP Rebar

Table 3.2. Phase II Test Program Matrix

Specimen ID (Phase – Specimen #)	Reinforcement (#/Specimen – Bar Type)
II-1	4 - #3 Steel Rebar
II-2	2 - #3 GFRP Rebar
II-3	3 - #3 GFRP Rebar
II-4	4 - #3 GFRP Rebar
II-5	2 - #4 Steel Rebar
II-6	2 - #4 GFRP Rebar
II-7	3 - #4 GFRP Rebar
II-8	4 - #4 GFRP Rebar

Table 3.3. Phase III Test Program Matrix

Specimen ID (Phase – Specimen #)	Dimensions (in.)	Reinforcement (#/Specimen – Bar Type)	Reinforcement Ratio
III-1	5 x 23.25 x 72	3 - #2 Steel Rebar	0.0016
III-2	5 x 23.25 x 72	3 - #2 GFRP Rebar	0.0017
III-3	5 x 23.25 x 72	5 - #2 GFRP Rebar	0.0029
III-4	5 x 23.25 x 72	7 - #2 GFRP Rebar	0.0040
III-5	7 x 23.25 x 72	2 - #5 Steel Rebar	0.0046
III-6	7 x 23.25 x 72	2 - #5 GFRP Rebar	0.0051
III-7	7 x 32 x 72	2 - #5 GFRP Rebar	0.0037
III-8	7 x 32 x 72	3 - #5 GFRP Rebar	0.0056
III-9	5 x 23.25 x 72	2 - #3 Steel Rebar	0.0025
III-10	5 x 23.25 x 72	2 - #3 GFRP Rebar	0.0030
III-11	5 x 23.25 x 72	3 - #3 GFRP Rebar	0.0044
III-12	7 x 23.25 x 72	2 - #4 GFRP Rebar	0.0034
III-13	7 x 32 x 72	2 - #4 Steel Rebar	0.0021
III-14	7 x 32 x 72	2 - #4 GFRP Rebar	0.0024

Conversion Units: 1 in. = 2.54 cm

3.2. TEST SPECIMENS

3.2.1. Phase I Specimens. There were a total of four specimens tested in Phase I. The type and amount of reinforcement was the variable for this phase. Specimen one (I-1) contained 2-#3 steel bars, specimen two (I-2) with 2-#3 GFRP bars, specimen three (I-3) had 3-#3 GFRP bars, and specimen four (I-4) contained 4-#3 GFRP bars. Figure 3.1 illustrates specimen three (I-3) on the left and specimen four (I-4) on the right. Specimens were 48 in. (122 cm) long, 12 in. (30.5 cm) wide, and 5 in. (13 cm) in thickness. To predetermine the crack location, a weakened plane was created at mid-span by reducing the cross-sectional area. This was done using a thin cold-formed steel angle. The legs 1.31 in. (3.3 cm) long extended into the cross-section the full specimen height at 24 in. (61 cm) from each end (see Figure 3.2). Continuous steel chairs 2.25 in. (5.7 cm) tall were placed 5 in. (12.7 cm) from each end to support the reinforcement bars and threaded rods. The reinforcement bars, threaded rods, lifting hooks, and chairs were all attached using wire ties. A strain gauge was attached to the center most reinforcement bar of each specimen 24 in. (61 cm) from the end by leveling a spot and gluing it to the bar. To evenly subject the specimens to pure tension, two 0.75 in. (1.9 cm) threaded steel rods spaced 4.5 in. (11.4 cm) on center were embedded in the concrete 7.5 in. (19 cm) from each end. As Figure 3.3 illustrates, a 0.75 in. (1.9 cm) grade 8 hex nut and washer were attached to the end of each threaded rod embedded in the concrete to increase the pull out capacity. To minimize any type of bond between the concrete and forms, the sides of the forms were oiled and two layers of 6-mil plastic sheeting were placed on the bottom of the formwork.



Figure 3.1. Common Phase I Specimens Before Concrete Placement



Figure 3.2. Steel Angle Used to Predetermine Crack Location



Figure 3.3. Embedded Threaded Rod with Hex Nut and Washer

3.2.2. Phase II Specimens. Phase II consisted of eight specimens that were very similar in dimensions and reinforcement compared to the four specimens cast for Phase I. The specimen dimensions, continuous chair layout, reinforcement bar height, threaded rod setup/location, lifting hook location, and strain gauge location were identical to Phase I specimens as detailed in Section 3.2.1. The method of reducing the concrete cross-sectional area to predetermine the first crack location was the only modification compared to Phase I specimens. In lieu of casting concrete around a thin cold-formed steel angles, grooves (control joints) were cut at mid-span on both sides of the 5 in. (12.7 cm) thick face once the concrete had set (see Figure 3.4). The grooves, approximately 0.188 in. (0.5 cm) wide, were cut 1 in. (2.5 cm) deep by using a hand held circular saw with a masonry/concrete blade. To prevent the concrete from bonding to the forms, all sides in contact with the concrete were lightly oiled. Before testing, a light coat of white

spray paint was applied to the surface of the concrete specimens to better see and measure crack formation and width.

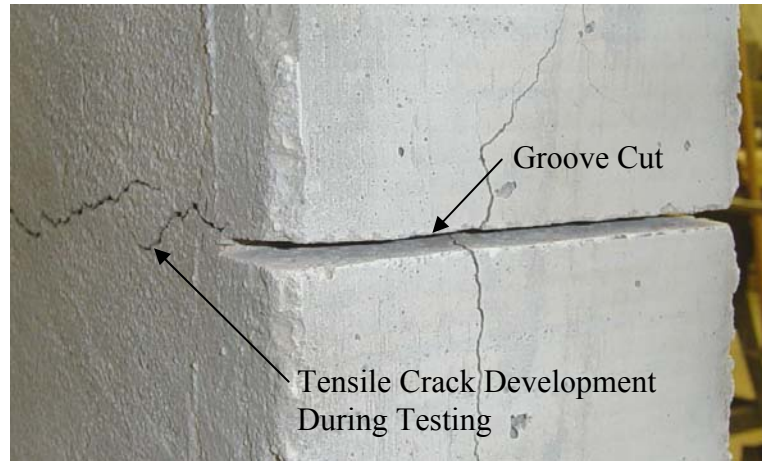


Figure 3.4. Grooves Cut to Predetermine Crack Location (Specimen shown during testing after crack development)

3.2.3. Phase III Specimens. A total of fourteen specimen panels were constructed and tested in Phase III of the research study. The variables within the phase included reinforcement bar type (steel or GFRP) and size (#2, #3, #4, #5), and panel size. Three different panel sizes were used to get desirable reinforcement ratios for the four different rebar sizes. The dimensions of the three panel sizes were 5 in. (12.7 cm) thick, 23.25 in. (59 cm) wide, and 72 in. (183 cm) long; 7 in. (17.8 cm) thick, 23.25 in. (59 cm) wide, and 72 in. (183 cm) long; and 7 in. (17.8 cm) thick, 32 in. (81cm) wide, and 72 in. (183 cm) long.

To insure a uniform concrete clear cover for all panels, 1 in. (2.5 cm) continuous steel chairs were used. For the panels containing #4 and #5 rebar, a single row of chairs

were placed the full panel width 16.5 in. (42 cm) for each end. Due to the flexibility of the #2 and #3 rebar, two rows of chairs were placed the full width on both sides of the panels. The first row of chairs were placed 4.5 in. (11.4 cm) from the panel ends, and 16.5 in. (42 cm) for the second row. To move the panels after the concrete has properly set, lifting hooks were placed in the concrete 10.5 in. (26.7 cm) from the ends of each panel. All rebar, chairs, and lifting hooks were attached using wire ties. Figure 3.5 illustrates a common Phase III panel before concrete placement.



Figure 3.5. Common Phase III Panel Before Concrete Placement

To predetermine the location of flexural cracks, the cross-section was reduced by cutting five small grooves on both sides of the extreme tensile surface in the constant moment region. As shown in Figure 3.6, the centerline located 39 in. (99 cm) from both ends of the panel was the location of groove C. With respect to groove C, A was cut 18

in. (45.7 cm) to the left, B was cut 9 in. (22.9 cm) to the left, D was cut 9 in. (22.9 cm) to the right, and E was cut 18 in. (45.7 cm) to the right. The groove depth for the panels with a thickness of 5 in. (12.7 cm) was 1.25 in. (3.2 cm), while a depth of 1.75 in. (4.4 cm) was used for the panels with a thickness of 7 in. (17.8 cm). The groove depth changed depending on panel thickness, while the groove length changed depending on panel width. A groove length of 3 in. (7.6 cm) was used for the panels 23.25 in. (59 cm) wide, and a length of 4.13 in. (10.4 cm) for the panels 32 in. (81 cm) wide. This system of different groove depths and lengths depending on panel dimensions was used to achieve the same percentage of cross-section reduction for each panel. The groove spacing was selected to be 9 in. (22.9 cm) based on ACI's estimation of crack spacing, while the groove depth was chosen to be one-fourth of the panel thickness. The groove lengths were randomly selected to provide adequate reduction in the cross-sectional area to predetermine the crack locations.

A total of four strain gauges were applied to each panel, two at mid-span and two at the quarter point. All four strain gauges were placed symmetrically in the panel on two rebar. Figure 3.7 shows the common application of a strain gauge to a GFRP rebar. To prevent the concrete from bonding to the forms, all sides in contact with the concrete were lightly oiled. Before testing, a light coat of white spray paint was applied to the tensile surface of the concrete specimens to better see and measure crack formation.

3.2.4. Form Development. Prior to batching concrete, a form system that would accommodate repeated use for all three phases needed to be designed. Once all of the various design issues were solved a system of five platforms was constructed. Figure 3.8 shows the platform system retrofitted for Phase III panels. The bottoms of the forms

were made of 0.75 in. (1.9 cm) plywood. Dimensional lumber was placed around the plywood and intermittently spaced in the center to elevate the bottom of the forms. The sides and platform specimen dividers were constructed of dimensional lumber 1.5 in. (3.8 cm) thick of various widths. All parts of the forms were connected using 2 in. (5.1 cm) wood screws that could be fastened and unfastened for form reuse. Upon construction completion, any major cracks or seams in the form joints were filled with clear silicon rubber sealant.

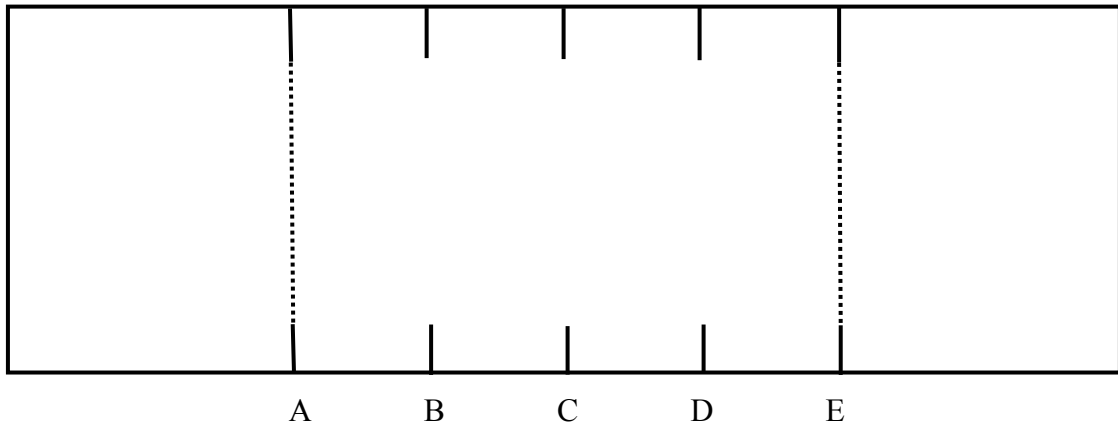


Figure 3.6. Illustration of Phase III Groove Pattern

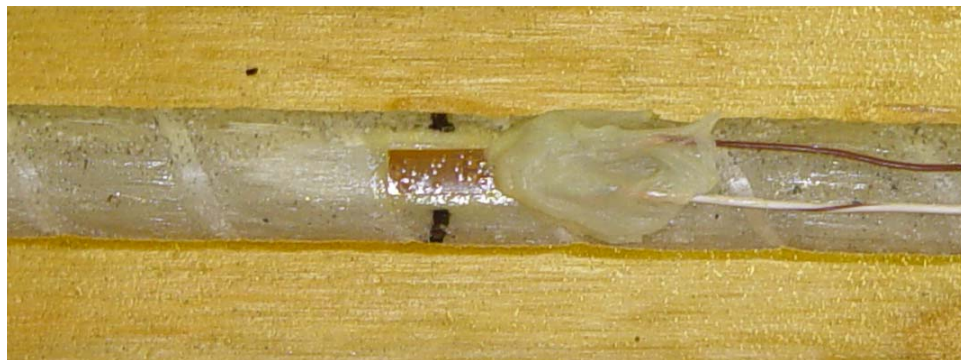


Figure 3.7. Common Strain Gauge Application to GFRP Rebar



Figure 3.8. Platform System Retrofitted for Phase III

3.2.5. Mixing Procedure. To insure consistency between laboratory batches, ASTM C 192-00 mixing specifications were followed. The mechanical mixer used had a maximum capacity of 9 ft^3 (0.17 m^3). Prior to starting the rotation of the mixer, all of the coarse aggregate and half of the mix water were added. The mixer was then turned on and the fine aggregate, cement, and remaining water were added while the mixer was rotated. Once all of the ingredients were in the mixer, the concrete was mixed for a minimum of 5 minutes for proper distribution of mix constituents. Then the mixer was turned off for 3 minutes of rest, a slump test was conducted, followed by a 2 minute final mixing. Upon completion, the batched fresh concrete was transported from the Materials Lab to the High-Bay SERL at UMR for placement and finishing.

3.2.6. Concrete Placement and Finishing. Once the fresh concrete was fully mixed, the slump test was performed according to ASTM C 192-00 specification. For determining the concrete compressive and flexural strengths, both cylinders and flexural beams were cast according to ASTM C 192-00 specification. Cylinders were

consolidated using a 0.375 in. (10 mm) diameter rod in two lifts. Plastic cylinder molds having a diameter of 4 in. (10.2 cm) and height of 8 in. (20.3 cm) were used for compression evaluation. Upon cylinder consolidation and surface finishing, white plastic caps were placed on the top of the molds to prevent moisture loss and geometry. Beams were cast to determine the modulus of rupture (MOR) of the concrete in metal forms that hinged to dimensions of 6 in. (15.2 cm) wide, 6 in. (15.2 cm) tall, and 24 in. (61 mm) long. The beams were consolidated using a wand type vibrator and finished with a steel trowel. The fresh concrete was placed in the specimen forms in two lifts, vibrating each lift with a wand type vibrator. Once the concrete was properly vibrated, a leveling bar was used to properly level the surface and screed away any excess concrete (see Figure 3.9). The concrete was then finished using a steel trowel.



Figure 3.9. Specimen Leveling of Fresh Concrete

3.2.7. Curing Procedure. Once Phase I specimens were cast, they cured uncovered for approximately 30 hours at room temperature and relative humidity (~60%). After 30 hours, the environmental cycling (see Section 4.4) started in the chamber exposing the specimens to high temperatures, low relative humidity, and high wind velocities. The environmental cycling continued for the 3 days of early-age testing; then the specimens were allowed to cure at laboratory conditions for the remainder of testing. Phase II specimens were cured at room temperature and relative humidity uncovered. After 5 days, the forms were stripped and the specimens were stacked until the time of testing. Since Phase II was not an early-age study, the date for form removal was arbitrary. As Figure 3.10 illustrates, Phase III panels were cured in their forms for four to five days under 4 mil plastic sheeting to avoid moisture loss. Then the forms were removed and the panels were stacked and allowed to cure at room temperature and relative humidity until time of testing. In the field, grooves are typically sawed no later than 18 hours of curing once the slab can support the weight.

3.3. MATERIALS

3.3.1. Concrete Mixes and Properties. Within the three phases of this study all of the specimens cast for each phase consist of different mix designs. The concrete for Phase I specimens consisted of two small batches that were mixed in the Materials Laboratory at UMR. The course aggregate (CA) used was a 0.75 in. (19 mm) maximum gradation gravel from the Little Piney Creek in central Missouri. The fine aggregate (FA) was natural river sand from the Tick Creek at the Gasconade River also in central Missouri. The mix water was potable laboratory water from Rolla Municipal Utilities in

Rolla, Missouri. Lastly, the Portland cement used was an ASTM Type I produced by Monarch. Tables 3.4 and 3.5 shows the mixture proportions in pounds per cubic yard and the batch weights for the two mix designs used in Phase I.



Figure 3.10. Phase III Concrete Curing

Phase II specimens were all cast from a single mix design provided by Parker Ready Mix Company located in Rolla, MO. The 0.75 yd³ of ready mix concrete contained coarse aggregate gravel and natural sand from the Tick Creek in central Missouri, Type I Portland cement, Rolla Municipal Utilities water, and a small dosage of an air-entraining agent. Table 3.6 shows the mixture proportions in pounds per cubic yard and the batch weights for the mix design used in Phase II.

The concrete for the fourteen panels of Phase III was provided by Breckenridge Ready Mix Company located in Rolla, Missouri in two different batches of the same mix

design. The first batch was used to cast the panels containing #2 and #5 reinforcing bars (Slab No. 1 to 8), while the second batch was used to cast the panels containing #3 and #4 reinforcing bars (Slab No. 9 to 14). This particular mix design contained gravel and natural sand both from the Little Piney Creek in central Missouri, Type I Portland cement, and mix water provided by Rolla Municipal Utilities. The admixtures included were Daravair 1400 air-entraining agent and Daracem 65 water reducer. Tables 3.7 and 3.8 show the mixture proportions in pounds per cubic yard and the batch weights for the two mix designs used in Phase III. For each of these phases, the selected mix designs were representative of designs used in bridge decks or floor systems.

Table 3.4. Phase I Laboratory Mix Design Batched on 01/28/03

Material	Mix Design (lb/yd ³)	Batch Weights (lb)
Type I Portland Cement	620	103
Little Piney Creek Gravel (CA)	1666	278
Tick Creek Natural Sand (FA)	1083	181
Water	360	60
Batch Volume = 4.5 ft ³		
Water/Cement Ratio = 0.58		
Slump = 3.0 in.		

Conversion Units: 1 lb/yd³ = 0.593 kg/m³, 1 lb = 0.454 kg, 1 in. = 25.4 mm

Table 3.5. Phase I Laboratory Mix Design Batched on 02/07/03

Material	Mix Design (lb/yd ³)	Batch Weights (lb)
Type I Portland Cement	620	113
Little Piney Creek Gravel (CA)	1666	302
Tick Creek Natural Sand (FA)	1083	197
Water	349	63
Batch Volume = 4.9 ft ³		
Water/Cement Ratio = 0.56		
Slump = 2.5 in.		

Conversion Units: 1 lb/yd³ = 0.593 kg/m³, 1 lb = 0.454 kg, 1 in. = 25.4 mm

Table 3.6. Phase II Ready Mix Design Batched on 01/14/03

Material	Mix Design (lb/yd ³)	Batch Weights (lb)
Type I Portland Cement	564	423
Little Piney Creek Gravel (CA)	1733	1300
Tick Creek Natural Sand (FA)	1311	983
Water	167	125
Air-Entraining Agent	3.0 oz.	2.25 oz.
Batch Volume = 3/4 yd ³		
Water/Cement Ratio = 0.3		
Slump = 3.0 in.		

Conversion Units: 1 lb/yd³ = 0.593 kg/m³, 1 lb = 0.454 kg, 1 in. = 25.4 mm

Table 3.7. Phase III Ready Mix Design Batched on 09/11/02

Material	Mix Design (lb/yd ³)	Batch Weights (lb)
Type I Portland Cement	564	1974
Little Piney Gravel (CA)	1586	5551
Little Piney Natural Sand (FA)	1302	4557
Water	256	896
AEA – Daravair 1400	3.0 oz.	10.5 oz.
Water Reducer – Daracem 65	16.92 oz.	59.2 oz.
Batch Volume = 3.5 yd ³		
Water/Cement Ratio = 0.45		
Slump = 5.0 in.		

Conversion Units: 1 lb/yd³ = 0.593 kg/m³, 1 lb = 0.454 kg, 1 in. = 25.4 mm

Table 3.8. Phase III Ready Mix Design Batched on 09/17/02

Material	Mix Design (lb/yd ³)	Batch Weights (lb)
Type I Portland Cement	564	1410
Little Piney Gravel (CA)	1586	3965
Little Piney Natural Sand (FA)	1302	3255
Water	256	640
AEA – Daravair 1400	3.0 oz.	7.5 oz.
Water Reducer – Daracem 65	16.92 oz.	42.3 oz.
Batch Volume = 2.5 yd ³		
Water/Cement Ratio = 0.45		
Slump = 3.75 in.		

Conversion Units: 1 lb/yd³ = 0.593 kg/m³, 1 lb = 0.454 kg, 1 in. = 25.4 mm

3.3.2. Steel Rebar. The steel rebar used for all three phases of the project were obtained from UMR's laboratory inventory remaining from past research projects. The rebar sizes used included No. 2, 3, 4, and 5. The No. 3, 4, and 5 sizes were deformed rebar containing the typical type S ribbed pattern while the No. 2 rebar was more similar to a smooth rod with intermittent grooves to increase the concrete bond. Since the manufactured properties were unavailable for the laboratory inventory, tensile coupon tests were performed according to ASTM A 307-02 specification to obtain material properties. As Table 3.9 illustrates, based on the laboratory tensile yielding and ultimate strength results, each rebar size was classified according to ASTM 615-01 standards. All test results can be found in Section 4.3 of this report.

Table 3.9. ASTM A 615-01 Steel Rebar Design Properties

Bar No.	Diameter (in)	Area (in ²)	Grade	f _y (psi)	f _u (psi)
2	0.250	0.05	Grade 75	75,000	100,000
3	0.375	0.11	ASTM A 615 Grade 40	40,000	60,000
4	0.500	0.20	ASTM A 615 Grade 40	40,000	60,000
4	0.625	0.31	ASTM A 615 Grade 60	60,000	90,000

Conversion Units: 1 in = 25.4 mm, 1 in² = 645 mm², 1 psi = 0.0069 MPa

3.3.3. GFRP Rebar. The FRP reinforcing materials were made of glass fibers embedded in a resin matrix. The GFRP rebar had a round solid cross-sectional shape with a sand-coated surface and a wrapped deformation pattern. The four rebar sizes used included No. 2, 3, 4, and 5. All GFRP rebar was Aslan 100 manufactured by Hughes Brothers, Inc. in Seward, Nebraska. For all research calculations, the GFRP rebar

properties published by Hughes Brothers were used as detailed in Table 3.10. As Table 3.10 indicates, the modulus of elasticity (E) or stiffness of the GFRP rebar is much lower than traditional steel rebar. This reduced stiffness for the GFRP rebar demotes its ability to control crack widths. As illustrated in Table 3.10, as the rebar size increases the design tensile strength decreases. Due to shear lag that develops between fibers in the larger sizes, the tensile stress varies as diameter increases (Hughes 2001).

Table 3.10. Aslan 100 GFRP Rebar Design Properties

Bar No.	Diameter (in)	Area (in ²)	f _{tu} (psi)	E (psi)
2	0.25	0.0515	120,000	5.92 x 10 ⁶
3	0.375	0.1307	110,000	5.92 x 10 ⁶
4	0.50	0.2245	100,000	5.92 x 10 ⁶
5	0.625	0.3372	95,000	5.92 x 10 ⁶

Conversion Units: 1 in = 25.4 mm, 1 in² = 645 mm², 1 psi = 0.0069 MPa

3.4. TEST SETUP AND PROCEDURES

All testing was performed in the High-Bay SERL at UMR. Experimental test setups were connected and anchored to the laboratory strong floor using Dywidag plates, nuts, and 1.41 in. (3.6 cm) threaded rods. A 50-kip (222 kN) and 100-kip (445 kN) load cells were used to measure the force applied by the hydraulic pump and jack. Strain gauges were read from individual strain indicators, while deflection was measured using analog dial gauges. A digital thermometer with humidity gauge was used to measure chamber environmental conditions. The crack widths were measured using a crack scope with a 0.13 in. (3.30 mm) field of view and a 0.12 in. (3.0 mm) measuring range with

increments every 0.002 in. (0.05 mm). All data was read and recorded by hand, then transferred into spreadsheets for further analysis.

3.4.1. Phase I Test Setup. The objective of Phase I testing was to determine how crack behavior is affected by different amounts of reinforcement at early-age under severe environmental conditions. The specimens were subjected to a constant restraining force and allowed to crack on their own due to drying shrinkage. To increase the rate and amount of concrete drying shrinkage and the effects of temperature, an environmental chamber was constructed to expose the specimens to cycles of high temperatures, low humidity, and high wind velocity. The cycling of extreme environmental exposure was to simulate pouring concrete on a hot and dry summer day. Approximately 40% or more of the total drying shrinkage was estimated to occur within the first week. The environmental chamber was constructed of cold-formed steel members that were covered with 6 mil plastic sheeting. The chamber dimensions were 10 ft (3.1 m) deep, 9 ft (2.7 m) wide, and 6 ft (1.8 m) tall. The chamber was heated by an 8 ft (2.4 m), 2500 watt baseboard heater elevated 18 in. (46 cm) and five 500 watt portable halogen work lights elevated 4 ft (1.2 m) above the specimens. The air was circulated using four 20 in. (51 cm) 3-speed box fans placed in front of the baseboard heater. Figure 3.11 illustrates the environmental chamber with the front open.

Due to testing Phase I specimens at early-age, the concrete was cast with the loading setup already in place around the forms. To load the specimens in pure tension, 3 ft. (91 cm) beams were attached to each end of the specimen and separated using a hydraulic jacks (see Figure 3.12). The beams consisted of two C-sections (C 10 x 30) built-up by placing the webs back-to-back with a 2 in. (5.1 cm) separation. To attach the

specimens to the beams, the threaded rods from the specimens were extended through the 2 in. (5.1 cm) separation in the beam and secured on the other side by a steel plate with a tightened washer and nut. The beams were separated by placing a hydraulic jack, a 2 ft. (61 cm) long steel circular tube section, and Dywidag plates between the beams and elongating the ram of the jacks with the hydraulic pump. The jack, tube, and plates on each side were centered and held in place between the beams by placing a Dywidag rod through them. The force applied to each specimen was determined by a load cell with a digital readout. As Figure 3.13 illustrates, the load cell was placed between two steel plates to measure the amount of force being transferred from the beams being separated, through the threaded rod and into the specimen.

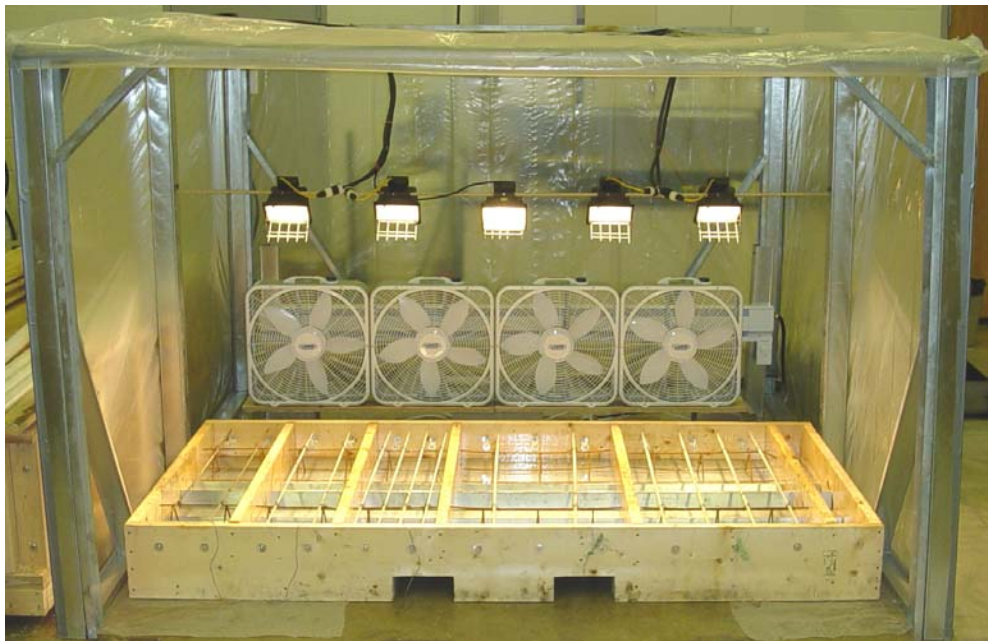


Figure 3.11. Environmental Chamber

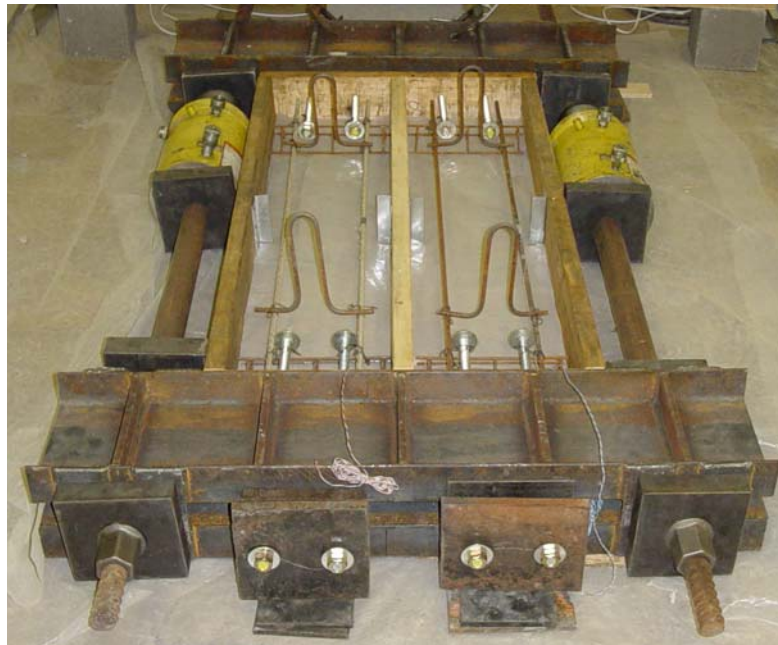
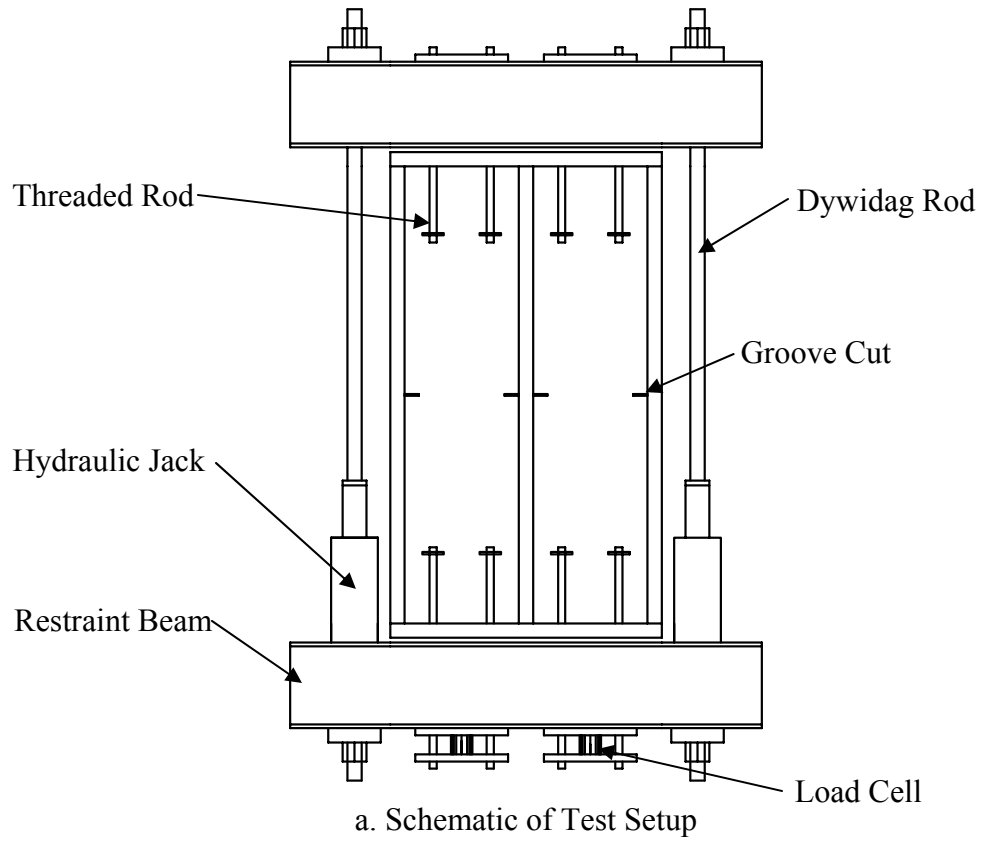


Figure 3.12. Phase I Test Setup

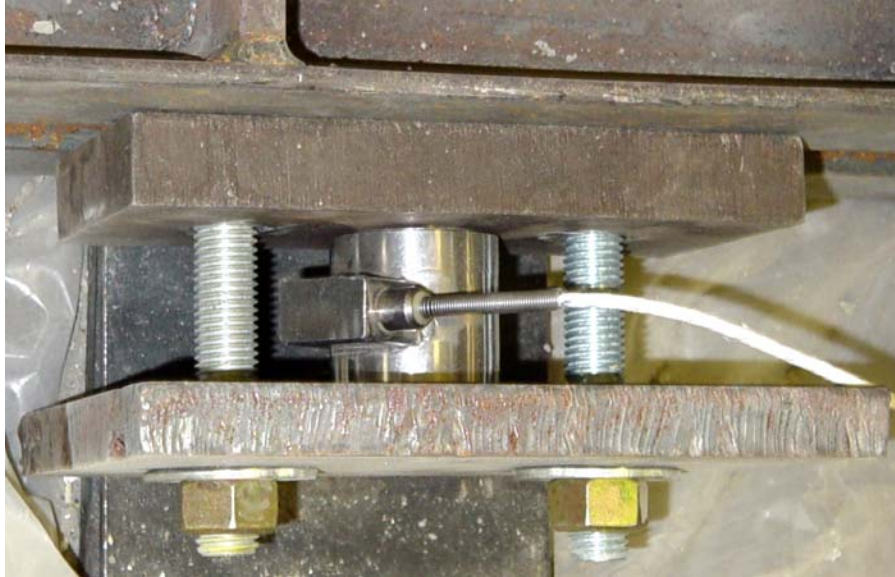


Figure 3.13. Load Cell Used in Phase I Testing

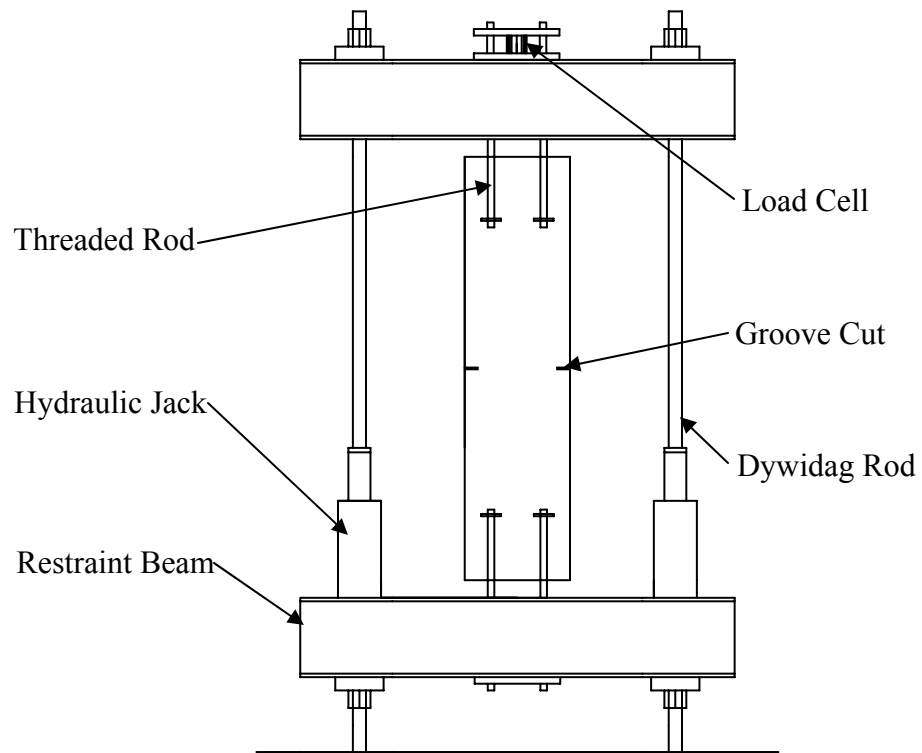
3.4.2. Phase I Test Procedure. The following steps summarize the environmental chamber cycling and test procedure for Phase I specimens.

- Test specimens were cast in the environmental chamber and allowed to cure uncovered at room temperature and humidity for approximately 30 hours for the concrete to develop minimal strength.
- After 30 hours, the concrete tensile strength was estimated by multiplying the average cylinder compressive strength by ten percent. Knowing the cross-sectional area of the weakened plane and the tensile strength of the concrete, the axial force required to produce the first crack was calculated.
- The specimens were then loaded to a restraining force slightly lower than the required amount to produce the first crack. The load was applied in increments of 1000 lbs (225 N) with the strain gauges being read each time.

- With the restraining force held constant, the environmental chamber was closed and the baseboard heater, halogen lamps, and fans were turned on to increase the drying shrinkage.
- The chamber remained on for approximately 5 hours with data being recorded every 1 to 2 hours. The recorded data included temperature, humidity, restraining load, strain, and crack width. The crack width was measured in three different locations per specimen.
- After 5 hours of extreme environmental conditions, data was recorded and the chamber was turned off for 12 hours until the next morning.
- The next morning, the chamber was turned on for 8 hours with data being recorded in 4 hour intervals. Following the 8 hours, the chamber was turned off for 16 hours until the next morning simulating daily conditioning.
- The following morning, the chamber was again turned on for an 8 hour cycle with data being recorded every 4 hours. Following the 8 hour cycle, the chamber was turned off approximately 45 hours.
- After exposing the specimens to environmental cycling for approximately 94 hours with the restraint held constant, the load was increased until specimen failure. The restraint was increased in increments of 1000 lb (225 N) with data being recorded for each. Upon reaching failure, pulling out of threaded rods, the tests were concluded and the specimens were discarded.

3.4.3. Phase II Test Setup. The objective of Phase II testing was to study how the amount and type of reinforcement affects the crack control characteristics of the specimens when subjected to tensile loading at later-ages. This study was a deformation

based experimental program. The significant variation between Phase I and Phase II testing was the environmental cycles and concrete age at the time of testing. Phase II specimens were allowed to cure uncovered for approximately three weeks at room temperature before testing. As illustrated in Figure 3.14, the Phase II setup is identical to Phase I except for testing vertically instead of horizontally on the floor. The test setup was supported vertically by threading the Dywidag rods into the inserts in the laboratory strong floor. The specimens were elected to be tested vertically so that cracks could be observed and measured from both sides since conditioning was not implemented. The specimens were placed in the test setup by removing the top restraint beam and setting them on the lower beam with the threaded rods extending between the 2 in. (5.1 cm) separation. Next, the top beam was set back into place with the threaded rods also extending through the beam separation. Once the specimen was in place, it was attached to the beams by securing steel plates with a washer and nut tightened on each threaded rod. Similar to Phase I, the load cell was placed between two steel plates to measure the amount of force being transferred from the beams to the actual specimen. To record the amount of specimen deformation, analog dial gauges on magnetic stands were attached to each hydraulic jack to measure the relative displacement of each side (see Figure 3.15). The dial gauges record the deflection in increments of 0.001 in (0.025 mm). The specimen elongation was determined to be the average elongation of both sides.



a. Schematic of Test Setup



b. Image of Test Setup

Figure 3.14. Phase II Test Setup



Figure 3.15. Phase II Method of Measuring Deformation

3.4.4. Phase II Test Procedure. The following steps summarize the test procedure followed for Phase II specimens.

- The test specimens were allowed to cure uncovered at room temperature for approximately three weeks before being placed in the test setup.
- Prior to testing, the concrete tensile strength was estimated by multiplying the average cylinder compressive strength by ten percent. Knowing the cross-sectional area of the weakened plane and the approximate tensile strength of the concrete, the axial force required to produce the first crack was estimated.
- Once the specimen was placed in the test setup, the dial gauges were set in place and zeroed, the strain gauge was attached to the indicator and balanced, and the load cell was zeroed.

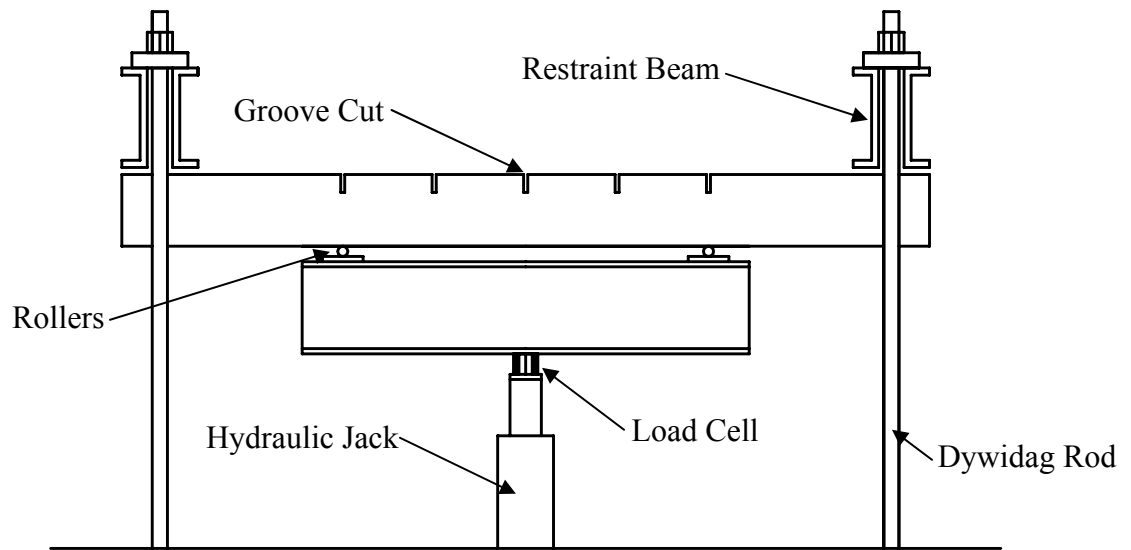
- Until the first crack was produced, the specimens were loaded in tension in increments of 1000 lbs (225 N) with data being recorded at each increment. The data being recorded included the tensile force, strain, and dial gauges.
- Once the specimen cracked, the crack widths were measured in three locations on each side of the specimen.
- After cracking, the specimen continued to be loaded in increments of 1000 lbs (225 N) with the tensile force, strain, dial gauges, and crack widths recorded each increment until ultimate failure.

3.4.5. Phase III Test Setup. The objective of Phase III testing was to develop a relationship between GFRP secondary reinforcement ratio and crack control for panels subjected to flexural loading. A steel secondary reinforcement ratio of 0.0018 was used as a benchmark for comparison of the various GFRP reinforcement ratios. The Phase III test setup was an inverted four-point flexure test setup. The end reactions consisted of steel rollers with a 1.5 in. (3.8 cm) diameter tack welded beneath the built-up C-section beams to create point bearing reactions. The end reactions were restrained by securing the built-up beams to the laboratory strong floor with Dywidag rods, plates, and nuts. The test setup had a total span length of 6 ft. (1.8 m). The panels were loaded through a built-up loading device and hydraulic jack which reacted against the laboratory floor. The built-up loading device consisted of two W-shaped sections placed side-by-side with two steel rollers tack welded 3 ft. (0.9 m) apart. When the jack ram was extended, the built-up loading device and end reactions created perfect four-point loading the full panel width with a 3 ft. (0.9 m) constant moment region in the center.

The load produced by the hydraulic jack was measured by placing a load cell between the built-up loading device and the hydraulic jack. To produce a level bearing surface, the load cell was placed between two steel plates. Knowing the load cell reading, the two upward point loads were calculated as being the load cell reading minus the weight of the panel and loading device all divided by two. During testing, the panel deflection was measured at the center, above both upward point loads, and at both end reactions. As illustrated in Figure 3.16, the deflections were measured with dial gauges that were mounted on a square tube section that spanned between the end reactions. A schematic and image of the Phase III test setup is shown in Figure 3.17.



Figure 3.16. Phase III Method of Measuring Deflection



a. Schematic of Test Setup



b. Image of Test Setup

Figure 3.17. Phase III Test Setup

3.4.6. Phase III Test Procedure. The following steps summarize the test procedure followed for Phase III panels.

- The test panels were allowed to cure at room temperature for five to seven weeks before being placed in the test setup.
- Once the panels were placed in the test setup, the dial gauges were set in place and zeroed, the strain gauges were attached to the indicators and balanced, and the load cell was zeroed.
- Depending on the calculated ultimate capacity, the panels were loaded in increments of 250 lb (56 N) to 2000 lb (450 N) until the first crack was produced. The load cell, strain gauges, and dial gauges were read and recorded each increment.
- Once the panel cracked, the crack widths were measured in three locations per crack on the tensile surface of the panel.
- After cracking, the panels continued to be loaded in increments of 250 lb (56 N) to 2000 lb (450 N) with load, strain, deflection, and crack widths recorded each increment until ultimate failure.

3.5. SUPPLEMENTAL TEST METHODS INVESTIGATED

As previously mentioned, currently there is no standard test method to evaluate secondary reinforcement. For this reason, preliminary test methods were investigated to develop the three phases of the project. Initially, the project addressed the effects of reinforcement on plastic shrinkage cracks. The formwork contained a sheet metal floor with three intermediate risers to reduce the cross-section and predetermine the location of

the first crack (see Figure 3.18). Previous research studies at other universities have experienced success studying plastic shrinkage crack using similar formwork. The results from this preliminary study were very limited. The water-to-cement (w/cm) for the mix designs used to simulate cast-in-place bridge decks were too high to produce adequate plastic shrinkage cracks to study the influence of FRP bars. The specimens were even unaffected when fans were used to increase the wind velocity over the specimens.



Figure 3.18. Specimen Forms to Investigate Plastic Shrinkage Cracks

For the second part of the preliminary test method investigation, the same formwork containing risers was used with a minimal degree of restraint added. The restraint was provided by 3/8 in. (9.5 mm) threaded rods with a washer secured to the end (see Figure 3.19). The specimens were tested in the environmental chamber to increase

the severity of the ambient temperature, relative humidity, and wind velocity. Likewise to the previous preliminary study, difficulties propagated with the test procedure. It was concluded that the degree of restraint was not significant enough to exceed the tensile capacity of the concrete to produce the first crack. The wood formwork did not provide a rigid enough system. The restraint system used in Phase I and II test was developed from the preliminary conclusions of this test investigation.

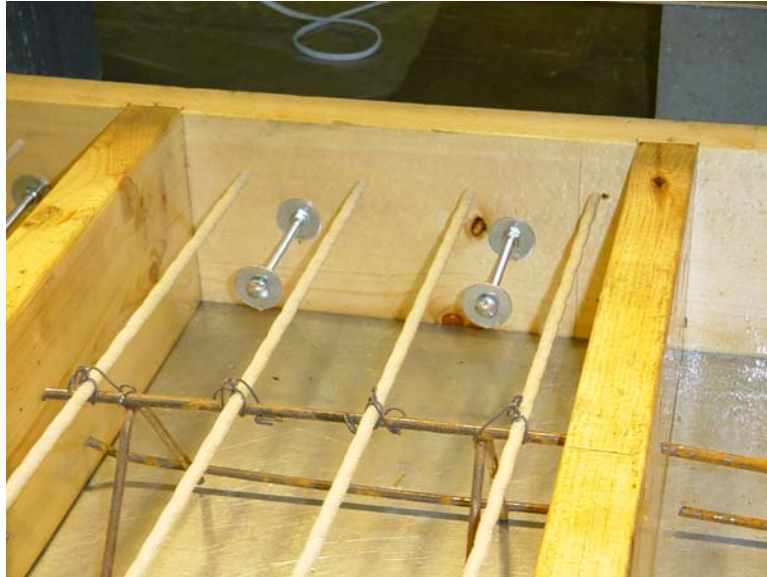


Figure 3.19. Specimen Forms with Minimal Restraint to Investigate Shrinkage Cracks

4. TEST RESULTS AND DISCUSSIONS

This section presents the results and discussion for all the tests performed. The results of the mechanical properties including concrete compressive strength, concrete flexural strength, and reinforcing steel tensile strength tests will be presented first. The main focus of this section will be on the crack control characteristics of the GFRP and steel reinforced specimens obtained from the tensile and flexural tests performed throughout the three phases of the project.

4.1. CONCRETE COMPRESSIVE STRENGTH TESTS

The compressive strengths of the concrete specimens were determined according to ASTM C 39-01 specification. The only deviation in the specification was the number of cylinders tested per batch of concrete. Due to batch size limitations, three representative QC/QA cylinders were not always tested per test age. The cylinders were tested using neoprene pads as the capping method in a 600,000 lb (2670 kN) Forney Testing Machine (see Figure 4.1). Cylinders were tested at the beginning and ending of each test program to obtain a window of compressive strengths for the duration of testing in each phase. Table 4.1 gives the average compressive strengths for each set of cylinders tested. As the results indicate, the concrete strength for all three phases was 4000 to 5000 psi (28 to 35 MPa) at 28 days. Figure 4.2 shows a representative compressive strength gain curve with time for the Phase III mix design batched on 09/17/02. This is a representative illustration of the other mixes utilized.



Figure 4.1. Forney Testing Machine

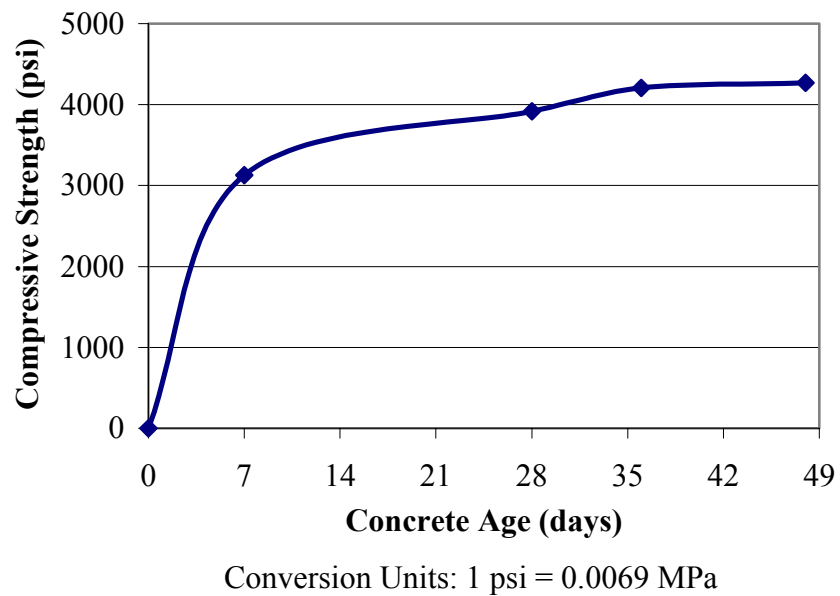


Figure 4.2. Compressive Strength Gain Curve for Phase III Concrete

Table 4.1. Cylinder Compressive Strength Results

Specimen ID (Phase – Specimen #)	Batch Date	Concrete Age	Number of Cylinders	Avg. Strength (psi)
I-1, I-2	01/28/03	1-day	2	1930
		5-day	2	3530
		28-day	2	4770
I-3, I-4	02/07/03	1-day	4	1900
		5-day	4	3470
		28-day	4	4420
II-1, II-2, II-3, II-4, II-5, II-6, II-7, II-8,	01/14/03	7-day	3	4070
		19-day	4	4790
		21-day	4	4790
		28-day	4	4890
III-1, III-2, III-3, III-4, III-5, III-6, III-7, III-8	09/11/02	36-day	4	5020
		42-day	2	5180
		54-day	6	5470
III-9, III-10, III-11, III-12, III-13, III-14	09/17/02	7-day	2	3130
		28-day	3	3920
		36-day	3	4200
		48-day	4	4270

Conversion Units: 1 psi = 0.0069 MPa

4.2. CONCRETE FLEXURAL STRENGTH TESTS

To estimate the flexural cracking moment of the Phase III panels, flexural beams were tested in third-point loading to determine the modulus of rupture. A 200,000 lb (890 kN) Universal Tinius–Olson Hydraulic Testing Machine was used according to

ASTM C 78-02 specification to determine the maximum applied load. Figure 4.3 illustrates the third-point test setup for flexural beams. For each of the Phase III concrete mix designs, four beams were cast and tested. To obtain a window of flexural strengths for the testing duration, two beams were tested prior to panel testing and two were tested after. Table 4.2 details the average modulus of rupture values for the Phase III panels.



Figure 4.3. Third-Point Loading of Flexural Beam

Table 4.2. Flexural Beam Modulus of Rupture Results

Specimen ID (Phase – Specimen #)	Batch Date	Concrete Age	Number of Beams	Avg. Strength (psi)
III-1 to 8	09/11/02	36-day	2	595
		54-day	2	590
III-9 to 14	09/17/02	36-day	2	645
		48-day	2	540

Conversion Units: 1 psi = 0.0069 MPa

4.3. REINFORCING STEEL TENSILE STRENGTH CHARACTERIZATION

As previously mentioned in Section 3.3.2, rebar tensile tests were performed since the manufactured properties were unavailable for the laboratory inventory. The coupon specimens were tested according to ASTM A 307-02 specification to obtain the yield and ultimate strengths for each rebar size. The strengths shown in Table 4.3 are the average results of three coupon tests. The steel coupon specimens were tested with a Tinius-Olsen Testing Machine in the Engineering Research Laboratory (ERL) at UMR. As the image in Figure 4.4 shows, an electronic extensometer was attached to the center of the steel rebar to measure the elongation of a 2 in. (5.1 cm) section. To prevent damaging the extensometer, it was removed from the specimen before reaching ultimate failure. The tensile load and elongation were recorded by a data acquisition system to develop stress-strain graphs for each specimen. From the graphs the yield and ultimate strengths were determined for each rebar size. Figure 4.5 shows a typical stress-strain graph for a No. 5 rebar specimen with the elastic, inelastic, and strain hardening regions clearly illustrated.

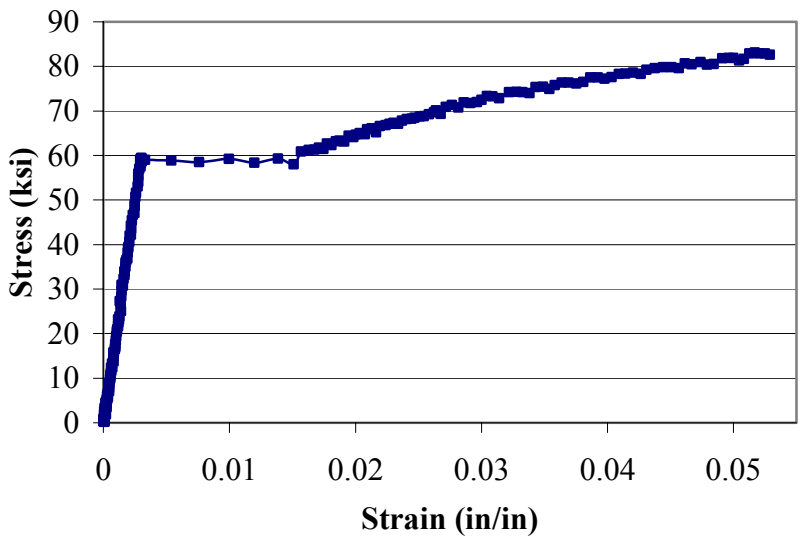
Table 4.3. Steel Rebar Strength Results

Bar No.	Diameter (in)	Area (in ²)	Grade	f _y (psi)	f _u (psi)
2	0.250	0.05	Grade 75	91,500	103,500
3	0.375	0.11	ASTM A 615 Grade 40	48,300	70,800
4	0.500	0.20	ASTM A 615 Grade 40	57,000	82,500
5	0.625	0.31	ASTM A 615 Grade 60	60,000	93,800

Conversion Units: 1 in = 25.4 mm, 1 in² = 645 mm², 1 psi = 0.0069 MPa



Figure 4.4. Steel Rebar Tensile Coupon Test



Conversion Units: 1 ksi = 6.9 MPa

Figure 4.5. Typical Stress-Strain Curve for a No. 5 Steel Rebar

4.4. PHASE I TESTS

This section provides results for the four specimens of Phase I exposed to environmental cycles while being subjected to a tensile restraining force. The purpose of this phase was to compare the crack characteristic of the steel reinforcement to GFRP reinforcement.

As previously mentioned in Section 3.4.1, the specimens were subjected to extreme environmental cycles by performing all tests in a controlled environmental chamber. As shown in Figure 4.6, the temperature in the environmental chamber cycled between 70° F (21° C) and 105° F (41 °C). Approximately 30 hours after concrete placement the chamber was initiated for the remainder of the day. To simulate natural daily heating cycles, the chamber was turned off over night. The following days, the chamber cycled by turning it on in the morning and turning it off in the evenings. Two specimens were tested simultaneously for each testing period; the 2-#3 steel and 2-#3 GFRP specimens were tested together, and the 3-#3 GFRP and 4-#3 GFRP specimens were also tested together. Even though the specimens were tested at two different times, the same procedure was followed resulting in very similar cycles as shown in Figure 4.6. Using the same weather measuring instrumentation, the relative humidity was also recorded throughout the environmental cycling. Figure 4.7 shows the humidity readings for the chamber cycling for the two testing period. Similar to the temperature readings, the humidity cycles were very similar for each testing period. In general, the humidity readings cycled between 30% and 15% with the minimum occurring when the temperature peaked. Before the chamber was initially activated, the humidity reading greatly depended on the conditions of the laboratory.

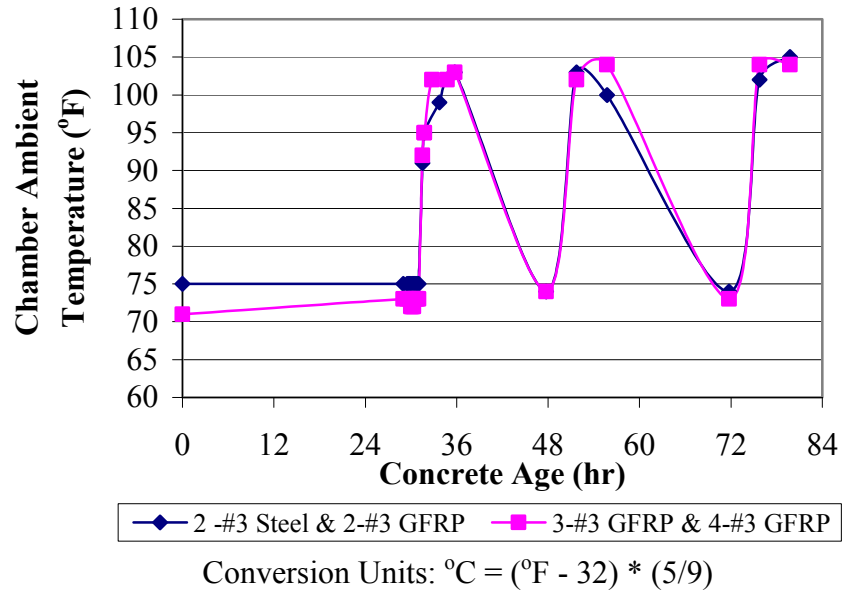


Figure 4.6. Phase I Environmental Chamber Ambient Temperature Cycles

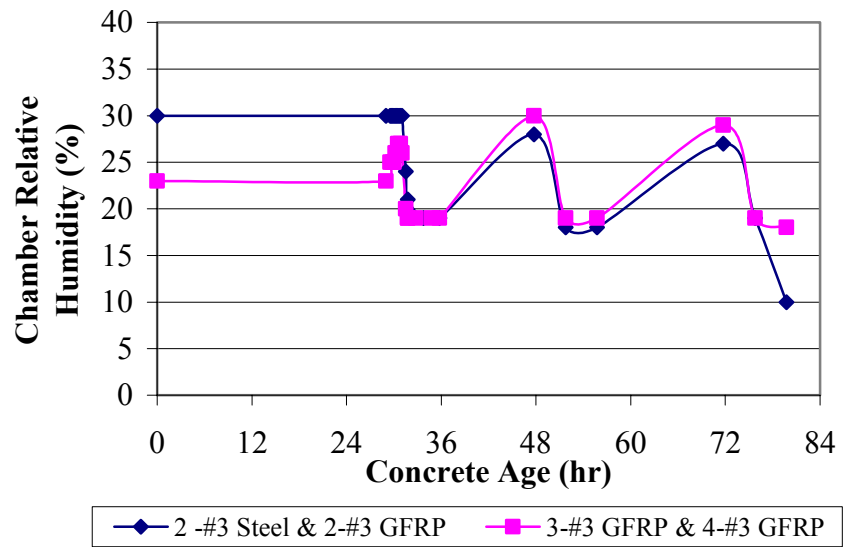


Figure 4.7. Phase I Environmental Chamber Relative Humidity Cycles

To measure the amount of strain in the steel and GFRP reinforcement, a strain gauge was applied to one of the rebar at mid-span. For all four specimens, the first crack formed at the notched mid-span location so the strain readings indicated the strain in the rebar directly at the crack. Figure 4.8 illustrates the strain in the rebar for the duration of the test. Approximately 45 minutes after starting the environmental conditioning the specimens cracked at mid-span. Prior to cracking the strain level remained under 100 micro-strain, but once the mid-span crack formatted it reflected a dramatic increase in strain. As predicted, the strain in the steel rebar remained relatively low compared to the GFRP rebar. In general, the strain measured in the specimen with two GFRP rebar was about twice as large as the strain in the specimen with four GFRP rebar. At each daily peak temperature, the maximum strain resulted in the rebar after the shrinkage crack developed.

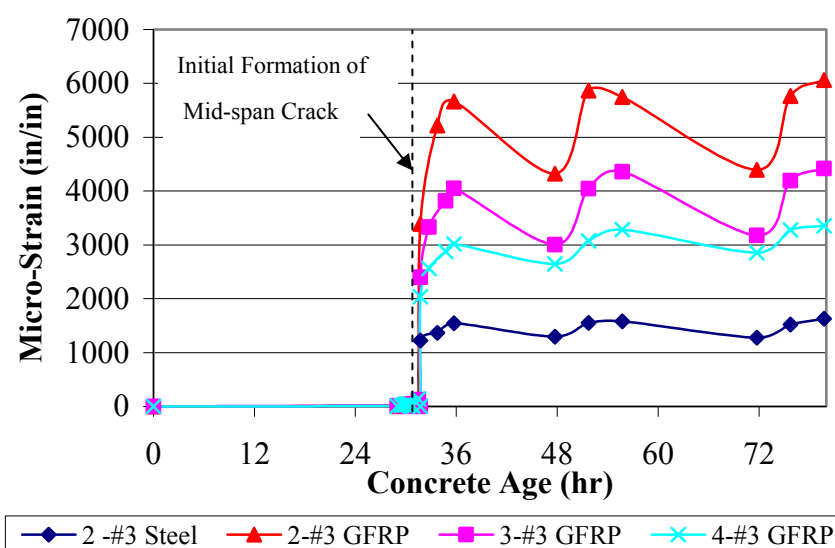


Figure 4.8. Phase I Micro-Strain vs. Concrete Age

The crack width characteristics for the four specimens are summarized in Figure 4.9. For each specimen type, the average crack width is plotted for each restraint load within the testing cycle. The average crack width was calculated by averaging three crack readings for each load. Similar to the rebar strain results, the specimen with steel rebar produced the smallest crack widths while the crack widths for specimens with GFRP rebar increased as the amount of reinforcement decreased. Both the peak restraint load and peak average crack width occurred when the chamber reached its peak temperature. As it is shown in Figure 4.9, the crack width increased the most during the first conditioning cycle. After this initial peak, the crack width slightly increased after the second and third environmental cycle as the shrinkage continued. For this reason, the peak crack width after the first heating cycle was determined for each specimen and primarily used for the data analysis portion of Phase I results.

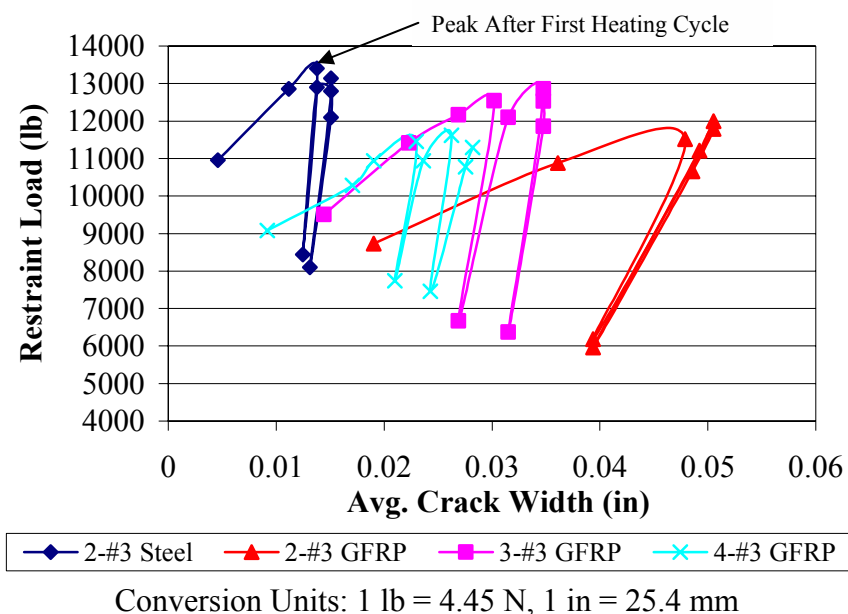


Figure 4.9. Phase I Restraint Load vs. Average Crack Width

Based on the peak crack widths after one conditioning cycle, the crack width for specimens of varying number of rebar and modulus of elasticity could be estimated. The peak crack widths are listed in Table 4.4 and illustrated using a bar chart in Figure 4.10. Based on the observed test results for the GFRP bar used in this investigation, it may be concluded that the specimen reinforced with two GFRP rebar produced a crack width about 3.4 times larger than the specimen reinforced with two steel rebar. Even the specimen with four GFRP rebar had an average crack width larger than the specimen with only two steel rebar. Although, slightly larger crack widths are acceptable since corrosion is not a concern with GFRP.

Table 4.4. Phase I Data Analysis Results

No. of Bars	Rebar Type	Crack Width (in)	Rein. Area (in ²)	Crack Width / Rein. Area (1/in)	Crack Width * Rein. Area (in ³)
2	#3 Steel	0.014	0.221	0.062	0.003
3	#3 Steel	0.009	0.330	0.028	0.003
4	#3 Steel	0.007	0.440	0.016	0.003
5	#3 Steel	0.006	0.550	0.010	0.003
6	#3 Steel	0.005	0.660	0.007	0.003
7	#3 Steel	0.004	0.770	0.005	0.003
2	#3 GFRP	0.048	0.262	0.183	0.013
3	#3 GFRP	0.030	0.393	0.077	0.012
4	#3 GFRP	0.023	0.524	0.044	0.012
5	#3 GFRP	0.019	0.655	0.028	0.012
6	#3 GFRP	0.015	0.786	0.020	0.012
7	#3 GFRP	0.013	0.917	0.014	0.012

Conversion Units: 1 in = 25.4 mm, 1 in² = 645 mm², 1/in = 1/25.4 mm, in³ = 16.4 cm³

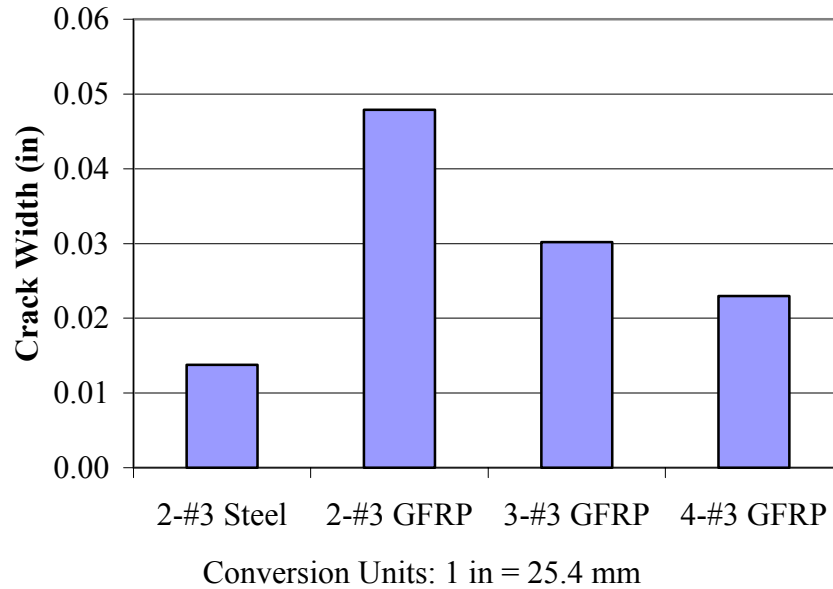


Figure 4.10. Phase I Average Peak Crack Width After First Heating Cycle

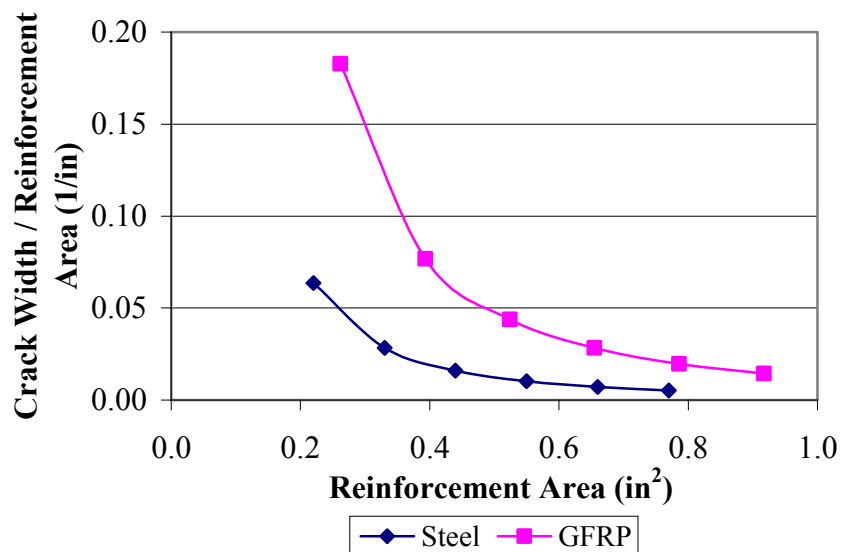
During the data analysis, it can be shown that a similar constant was produced when the crack width was multiplied by the reinforcement area. This relationship was illustrated by the following derivation:

1. Stress (σ) is equal to the modulus of elasticity (E) multiplied by strain (ϵ) for a linear elastic material; $\sigma = E\epsilon$
2. Stress (σ) is also equal to force (P) divided by area (A); $\sigma = \frac{P}{A}$
3. Strain (ϵ) is equal to deflection (Δ) divided by length (L); $\epsilon = \frac{\Delta}{L}$
4. Substituting line 2 and line 3 into line 1 results $\frac{P}{A} = E \frac{\Delta}{L}$
5. Rearranging equation in line 4 results $\Delta A = \frac{PL}{E}$

6. Therefore, assuming the applied force (P), length (L), and modulus of elasticity (E) are similar for all specimens, the deflection (Δ) or measured crack width multiplied by the reinforcement area (A) is constant for all. The previous six steps are summarized in Equation 4.1.

$$\left(\sigma = E\varepsilon \rightarrow \sigma = \frac{P}{A} \rightarrow \varepsilon = \frac{\Delta}{L} \rightarrow \frac{P}{A} = E \frac{\Delta}{L} \rightarrow \Delta A = \frac{PL}{E} \right) \quad (\text{Equation 4.1})$$

With this relationship, the crack width multiplied by reinforcement area was selected to the 0.003 in³ (49.2 mm³) for specimens reinforced with #3 steel rebar and 0.012 in³ (197 mm³) for specimens reinforced with #3 GFRP rebar. With these selected values, the crack widths of additional specimens with increased amounts of reinforcement were estimated by dividing the selected value by the reinforcement area. It must be noted that this crack width estimation is only for a specimen with the same dimensions, applied tensile load after one heating cycle, and modulus of elasticity as the specimens tested within this phase. Now having the calculated crack width and knowing the reinforcement area for the additional specimens, the efficiency of the reinforcement was calculated by dividing the crack width by the reinforcement area. Figure 4.11 illustrates the plot of crack width / reinforcement area vs. reinforcement area for specimens containing two to seven steel and GFRP rebar. As illustrated in Figure 4.11, the steel rebar is about four times more efficient at controlling crack widths than GFRP. According to ACI 440-03, 2.5 to 3 times more GFRP reinforcement is required than steel.



Conversion Units: 1/in = 1/25.4 mm, 1 in² = 645 mm²

Figure 4.11 Phase I Crack Width / Reinforcement Area vs. Reinforcement Area

Up to this point, all of the crack width results and predicted estimates for specimens containing GFRP rebar were based on a modulus of elasticity of 5.92×10^6 psi (40,800 MPa). As previously mentioned, the modulus of elasticity of the reinforcement is the most significant material property which governs temperature and shrinkage crack control. Placing significance on this property, the crack widths for the three GFRP test specimens were calculated for the GFRP modulus of elasticity range. Typically, the modulus of elasticity of GFRP rebar extends from 5.1×10^6 psi (35,200 MPa) to 7.4×10^6 psi (51,000 MPa). The three parts of Equation 4.2 were used to calculate the expected crack widths for the range of stiffness. Part one of the equation was previously described in this section. Since we were solving for crack width (Δ) in this direct tension/restraint test, the specimen length (L) was the only unknown. Part two of Equation 4.2 was then used to determine the effective length for each of the three test specimens. The effective

rebar length was calculated to account for the bond between the rebar and concrete. The full rebar length could not be used since the rebar was not allowed to uniformly elongate the full length. After calculating the effective lengths, the remaining values were substituted into part three of Equation 4.2 to calculate the crack width for varying stiffness.

$$1) \frac{P}{A} = E \frac{\Delta}{L}, \quad 2) L = \frac{\Delta AE}{P}, \quad 3) \Delta = \frac{PL}{AE} \quad (\text{Equation 4.2})$$

The effective lengths and calculated crack widths after the first conditioning cycle for the modulus of elasticity range are listed in Table 4.5 for the three different specimens. Figure 4.12 presents the results in a bar chart while the graph in Figure 4.13 plots crack width vs. reinforcement area. Both figures show an increase in crack width as the modulus of elasticity decreases. Even when the reinforcement area is held constant, the GFRP modulus of elasticity range results in a 45% to 50% increase in crack width. This drastic increase in crack width alone emphasizes the significance of stiffness for temperature and shrinkage crack control.

Table 4.5. Phase I Calculated Crack Widths for Modulus of Elasticity Range

Specimen	Restraint Load (lb)	Effective Length (in)	Crack Width (in) for various E (psi) values		
			E = 5.1 x 10 ⁶	E = 5.92 x 10 ⁶	E = 7.4 x 10 ⁶
2-#3 GFRP	11520	6.4	0.056	0.048	0.038
3-#3 GFRP	12540	5.6	0.035	0.030	0.024
4-#3 GFRP	11460	6.2	0.027	0.023	0.018

Conversion Units: 1 lb = 4.45 N, 1 in = 25.4 mm, 1 psi = 0.0069 MPa

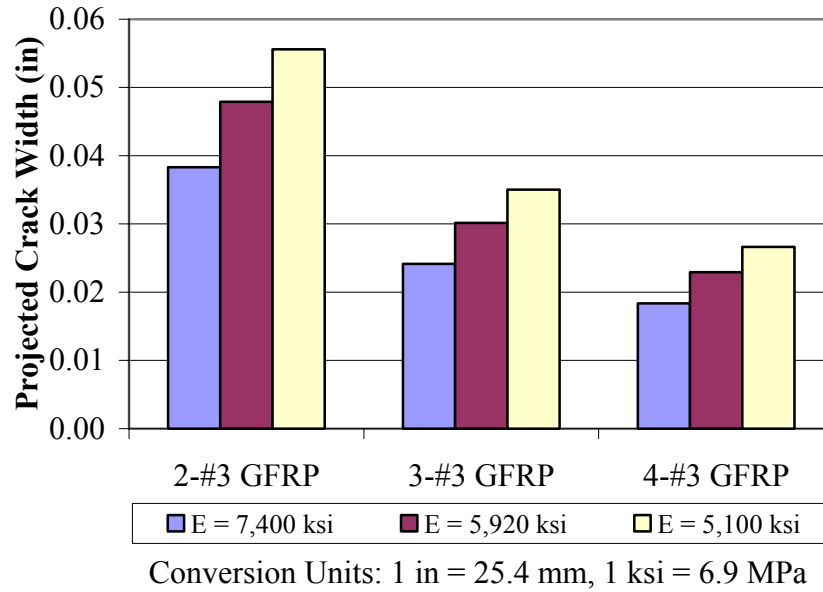


Figure 4.12 Phase I Expected Peak Crack Widths After First Condition Cycle for GFRP Modulus of Elasticity Range

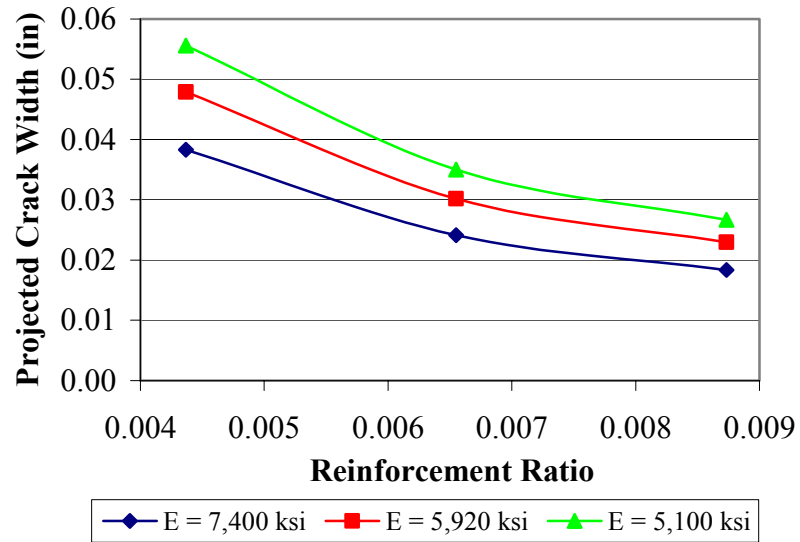


Figure 4.13 Phase I Peak Crack Width vs. Reinforcement Area for GFRP Modulus of Elasticity Range

4.5. PHASE II TESTS

This section provides the test results and discussion of the eight Phase II specimens. The specimens were tested in pure tension with crack width, elongation, and reinforcement strain recorded each loading increment. The purpose of this phase was to compare the later-age crack control characteristic of the steel reinforcement to GFRP reinforcement so a better understanding of shrinkage and temperature reinforcement could be gained using a deformation controlled tensile test method.

The laboratory testing program followed through as expected. For each specimen the first crack formed at the predetermined center location. Once the first crack developed, additional cracks formed on both sides of the specimen as the load continued to be increased. As observed in several specimens, multiple cracks formed on the front and back of the panel face. Figure 4.14 illustrates a typical crack pattern of a Phase II specimen during testing. Appendix A contains illustrations of crack patterns for all specimens at ultimate failure. Due to slight eccentric loading, crack widths on one side of the specimen were wider than on the other side for several specimens. For this reason, crack widths were measured on both sides to calculate a total crack area on the surface. Due to stress concentration, the failure of each specimen occurred at the point where the tensile load was transferred from the threaded rod to the concrete. This failure mode occurred prior to reinforcement rupture.

The deformation of each specimen was measured with dial gauges. A gauge was positioned on each hydraulic jack to measure the ram extension for each load interval as described in Section 3.4.3. During the testing of a few specimens, it was noticed that one ram extended more than the other until the load increased and the hydraulic pressure

evened out and stabilized. The specimen deformation was calculated by averaging the two dial gauge readings. Figure 4.15 plots tensile load vs. elongation for all eight specimens. The elongation of all specimens followed a similar trend until that first crack formed at a tensile load of 14,000 to 15,000 lbs (62 to 67 kN). Once the concrete cracked, the two specimens with steel rebar continued to follow the same trend, while the remaining specimens containing GFRP rebar significantly elongated. Due to the low modulus of elasticity, the GFRP specimens elongated approximately two times more than the steel specimens. The specimens containing large amounts of GFRP area achieved higher tensile loads than specimens with less area at similar elongation measurements.



Figure 4.14. Phase II Typical Specimen Crack Pattern

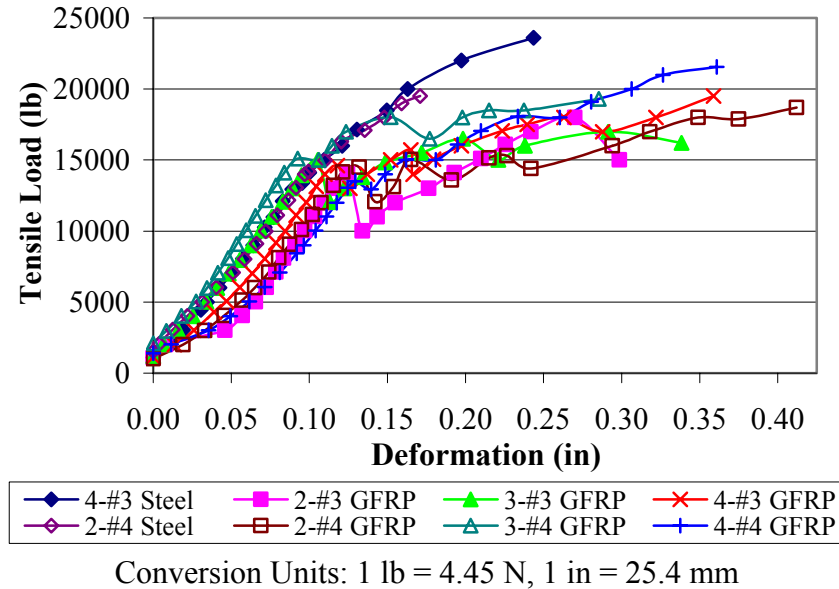


Figure 4.15. Phase II Tensile Load vs. Deformation

A strain gauge placed at mid-span measured the strain in the rebar for each specimen at the instrumented location. As previously mentioned, for all specimens the first crack formed at the notched location so the strain results are that of the rebar directly at the crack. A plot of tensile load vs. micro-strain is illustrated in Figure 4.16. As also seen with the elongation, the strain results of all specimens followed a similar trend until the first crack formed. It remained under 200 micro-strain until the first crack when it drastically increased. The first crack formation caused the strain in the steel rebar to increase to approximately 1000 micro-strain while the GFRP jumped to 2500 to 6000 micro-strain. Lower strain values were expected for specimens containing steel rebar due to its increased stiffness. After cracking, the specimens containing GFRP rebar resulted in strain values three to ten times greater than specimens with steel rebar. Likewise, as

the amount of reinforcement increased, the tensile load increased and the strain decreased.

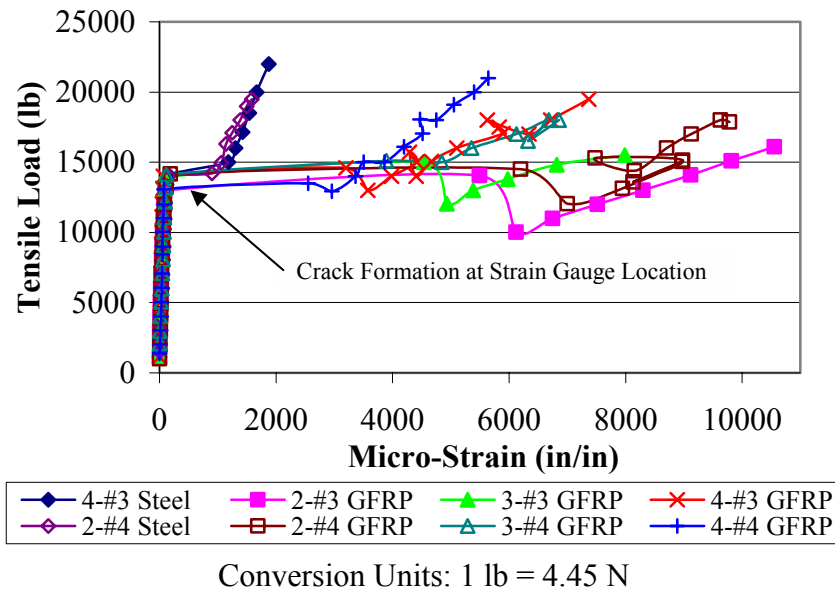
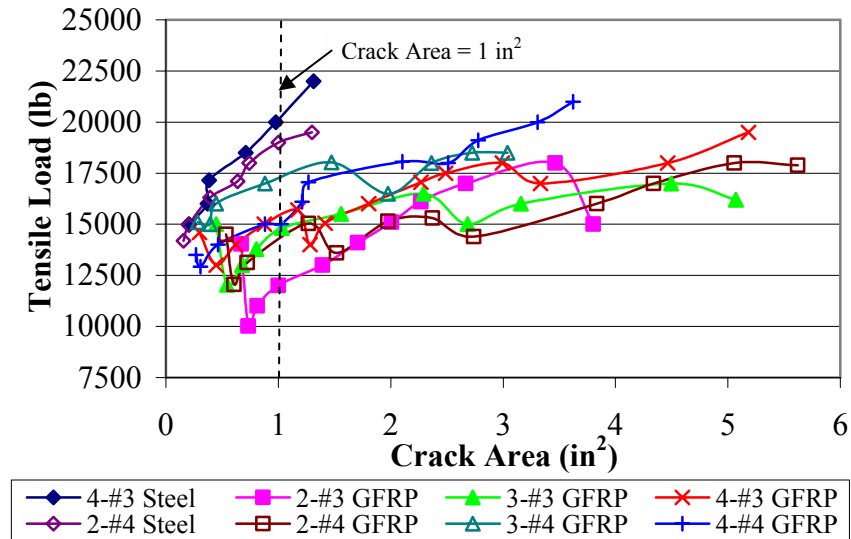


Figure 4.16. Phase II Tensile Load vs. Micro-Strain

Similar to the other phases of the project, the crack width and crack area analysis were the primary focus of the study. For this reason, the crack widths were measured on both sides of the specimens and the total crack area was calculated for each load increment. Figure 4.17 plots the crack area vs. tensile load for Phase II specimens. This particular figure illustrates higher tensile loads for specimens with steel rebar than GFRP rebar at the same crack area. In Figure 4.17, the two specimens with steel reinforcement have a steeper slope, while the slope for the six GFRP reinforced specimens is less steep. The steeper plots represent less crack area for increasing tensile load. Due to additional crack formation causing the load to decrease, the load cycles up and down for several

specimens while the crack area increases. In general, as the reinforcement area increases, the crack area decreases for a given load.



Conversion Units: 1 lb = 4.45 N, 1 in² = 6.45 cm²

Figure 4.17. Phase II Tensile Load vs. Crack Area

To perform a comparison of steel reinforcement to GFRP reinforcement and to determine how reinforcement area affects concrete cracking at later-age, the tensile loads were selected at a crack area equal to one square inch (6.45 cm²) for further analysis. Knowing the reinforcement area and tensile load of each specimen, a term referred to as efficiency was defined as the tensile load divided by crack area. Table 4.6 lists the reinforcement area, tensile load, and calculated efficiency for each specimen. A visual comparison of the tensile load at a crack area of 1 in² (6.45 cm²) is illustrated in Figure 4.18 as an example. For the two steel specimens, the tensile capacity increases as the amount of reinforcement area increases. Comparing the six GFRP specimens, the load

capacity generally increases as the amount of GFRP area increases except for the specimen containing 4-#4 rebar. For this exception, the tensile capacities for the 4-#3 and 3-#4 specimens were greater even though the reinforcement area was less.

The reinforcement efficiency calculations resulted in excellent trends for both the steel and GFRP. As seen in Figure 4.19, each material has a linear relationship for the efficiency vs. reinforcement area plot. The given test specimens result a decrease in efficiency for both steel and GFRP as the reinforcement area increases. This is partially due to the small specimen cross section and increased reinforcement ratios. To more accurately compare the efficiency of steel to GFRP, linear trend lines were generated for both sets of data. The equations for both trend lines are listed on the graph in Figure 4.19. The two trend line equations conclude that the steel reinforcement is 1.3 times more efficient than the GFRP reinforcement.

Table 4.6. Phase II Efficiency at a Selected Crack Area

Specimen	Reinforcement Area (in ²)	Load (lb) at Crack Area = 1in ²	Efficiency (lb/in ²)
4-#3 Steel	0.442	20140	45590
2-#3 GFRP	0.262	12000	45800
3-#3 GFRP	0.393	14860	37810
4-#3 GFRP	0.524	15290	29180
2-#4 Steel	0.393	19000	48380
2-#4 GFRP	0.449	14100	31400
3-#4 GFRP	0.674	17200	25540
4-#4 GFRP	0.898	15000	16700

Conversion Units: 1 in² = 6.45 cm², 1 lb/in² = 0.69 N/cm²

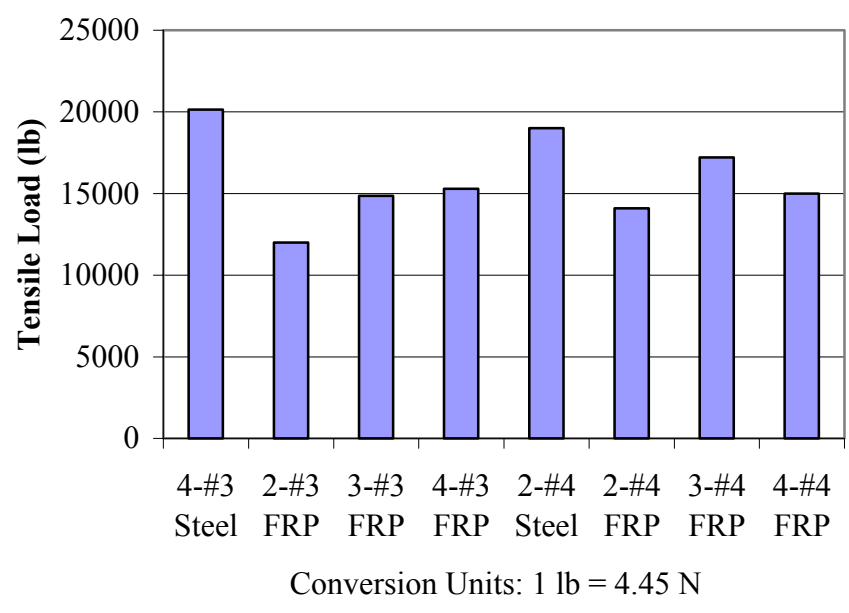


Figure 4.18. Phase II Tensile Load at a Given Crack Area = 1 in²

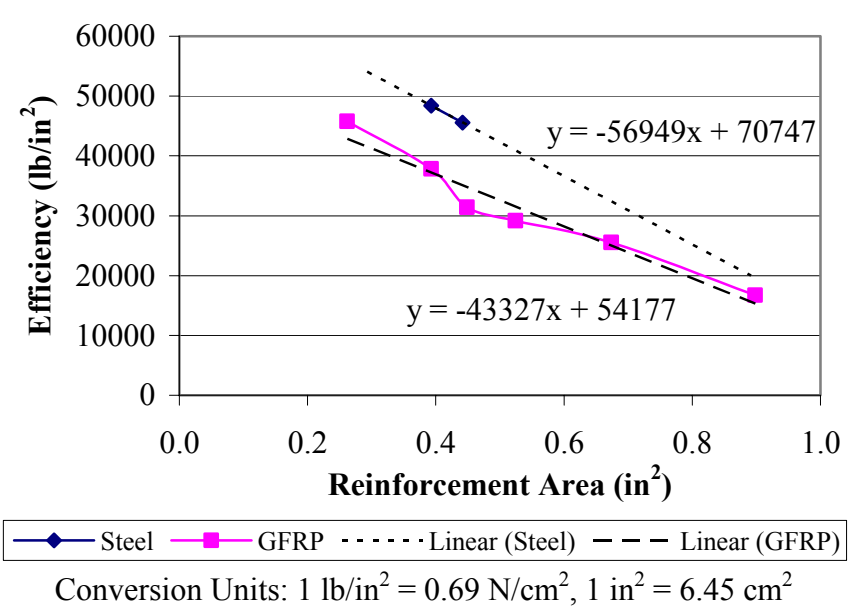


Figure 4.19. Phase II Efficiency vs. Reinforcement Area at Crack Area = 1 in²

4.6. PHASE III TESTS

This section of the report provides the test results and discussion for the fourteen panel specimens of Phase III. The panels were subjected to flexural loading with crack width, deflection, and reinforcement strain recorded for each incremental load. The purpose of this phase was to develop a relationship between GFRP reinforcement ratio and crack control for panels subjected to flexure.

The laboratory testing of the panels followed through as expected. All of the initial cracks formed at the notches placed on the tensile face of the panels. In general, the first couple of cracks formed at the notch locations and additional ones formed between the notches as the panels approached ultimate capacity. Figure 4.20 shows a panel being tested where the first five cracks formed at the predetermined locations. Panels which resulted in shorter crack spacing were ones with smaller rebar spacing. No overall trend in crack spacing was observed due to the prelocated notches altering the placement and spacing. Appendix B contains illustrations of the ultimate crack patterns for all Phase III panels.

For most of the panels, the first crack formation occurred at the quarter points where the point loads were applied (groove A and E) at a location of maximum moment. Commonly, once one of these end cracks formed additional cracks began to form at the remaining grooves. The panels of low GFRP reinforcement ratios usually failed at groove A or E due to FRP rupture. Slab number two containing only 3-#2 GFRP rebar formed a single crack at groove E and failed due to FRP rupture below the estimated capacity. Some of the larger panels experienced reinforcement pullout with failure occurring near one of the end reactions. Diagonal shear cracks were produced near the

end reactions on two of the largest panels. Overall, actual cracking loads were fairly close to the calculated, yet the actual ultimate loads achieved were less than the calculated due to localized failure at the end reactions. Table 4.7 summarizes the predicted failure load, actual tested failure load, and failure mode for the fourteen Phase III test panels.

During the testing procedure, the panel deflection and reinforcement strain were recorded for each load increment. The deflection was measured at five locations; the center, each quarter point, and the interior side of each end reaction. Figure 4.21 illustrates a representative deflection graph for Phase III testing. The remaining deflection graphs for each panel test are located in Appendix B. Typically, the amount of deflection decreased as the reinforcement area increased. As expected, the maximum deflection occurred at the center of the panel. The strain in the reinforcement was measured in four locations per panel; two at the center and two at one of the quarter points (notch location A and C). Similar to previous test results, the strain slightly increased until a crack formed at the location of the gauge. Figure 4.22 illustrates a representative load vs. micro-strain graph for Phase III testing. Appendix B contains the remaining load vs. micro-strain graphs for each panel. Each graph contains two curves, one is the average strain of the two center gauges and the other is the average strain of the two gauges at the quarter point. Even though the strain gauges were positioned directly below the notches, cracks did not always form at these two locations. For this reason, it is difficult to compare the strain data of one panel to another. To be able to properly compare the strain between panels at a given load, both panels must have the same formation and location of cracks with respect to the location of the strain gauge.

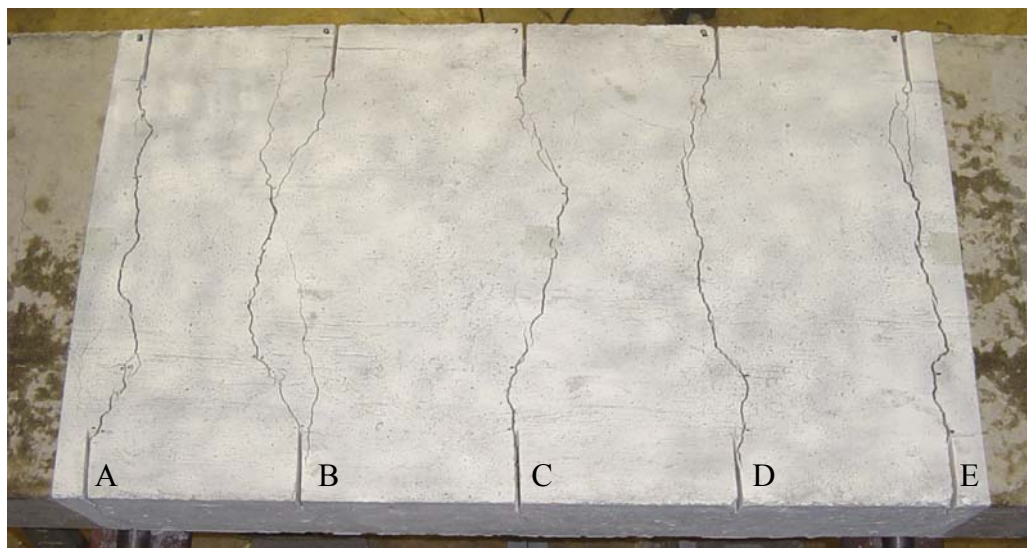


Figure 4.20. Phase III Typical Panel Crack Pattern

Table 4.7. Phase III Test Results

Specimen ID (Phase – Specimen #)	Predicted Failure Load (kip)	Actual Failure Load (kip)	Failure Mode
III-1	6.4	6.8	Steel Yielding
III-2	7.7	6.2	GFRP Rupture
III-3	12.8	8.7	GFRP Rupture
III-4	16.8	11.2	GFRP Rupture
III-5	34.6	30.9	Steel Yielding
III-6	38.5	34.3	GFRP Pullout
III-7	38.5	34.4	GFRP Rupture
III-8	57.7	27.8	Failure at End Reaction
III-9	6.4	4.6	Steel Yielding
III-10	11.7	7.1	GFRP Rupture
III-11	15.4	13.3	GFRP Rupture
III-12	27.3	16.9	GFRP Rupture
III-13	20.5	21.0	Steel Yielding
III-14	27.3	18.5	NA

Conversion Units: 1 kip = 4.45 kN

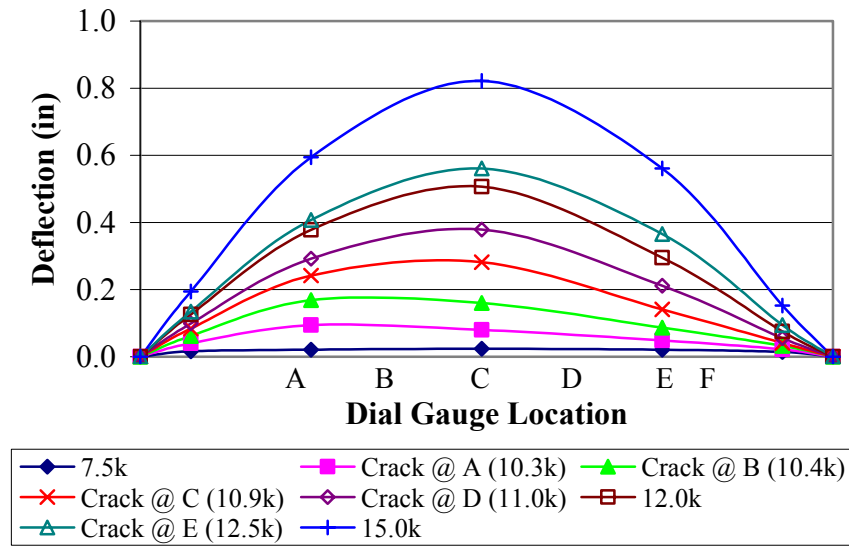


Figure 4.21. Phase III Typical Deflection Graph

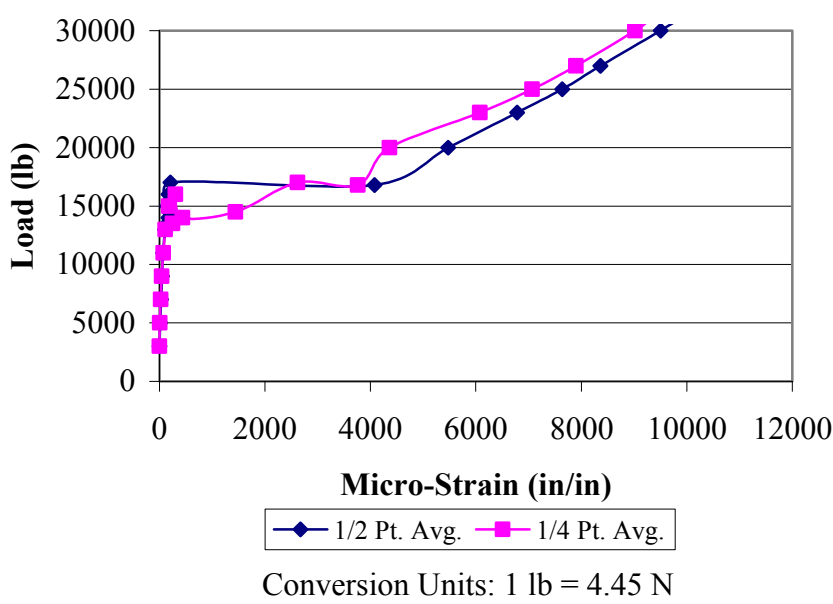


Figure 4.22. Phase III Typical Load vs. Micro-Strain Graph

The total crack area for each panel was calculated by summing the average width of each crack multiplied by the panel width. All crack widths were measured at the tensile surface instead of on the side at the location of the reinforcement. The following three figures plot load vs. crack area for the three different panel sizes. For comparison, each graph contained at least two plots for GFRP and one plot for steel reinforcement. As shown in Figure 4.23, panels with a GFRP reinforcement ratio twice as large as steel resulted in similar crack control characteristics. For example, Figure 4.23 shows a panel with a steel reinforcement ratio of 0.0016 performing very similar to a GFRP panel of 0.0029. Likewise, the panel containing a GFRP ratio of 0.0040 is performing better than both. Slab 9 containing a steel reinforcement ratio of 0.0025 is shown producing the largest crack area for the lowest flexural load. The excessive crack widths and deflection are due to reinforcement yielding. The number three rebar in this panel contained the lowest steel yield strength.

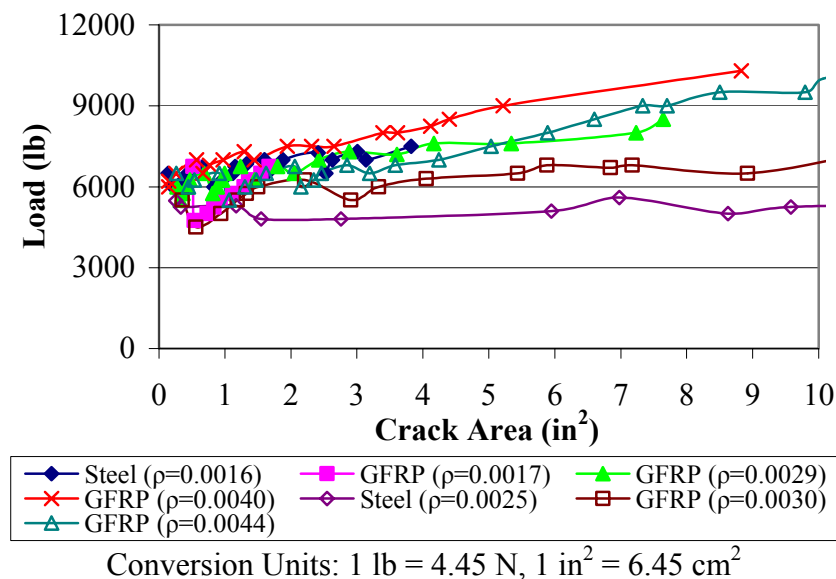


Figure 4.23. Phase III Load vs. Crack Area for 23.25''x5''x78'' Panels

Figure 4.24 presents the crack control characteristics for the three medium size panels. Unfortunately, the analysis of this particular set of test data is more difficult. Unlike the other two figures, the steel reinforcement ratio is higher or very similar to the two GFRP reinforcement ratios. The results of the three panels are as expected, yet no equivalent GFRP ratio compared to steel can be selected.

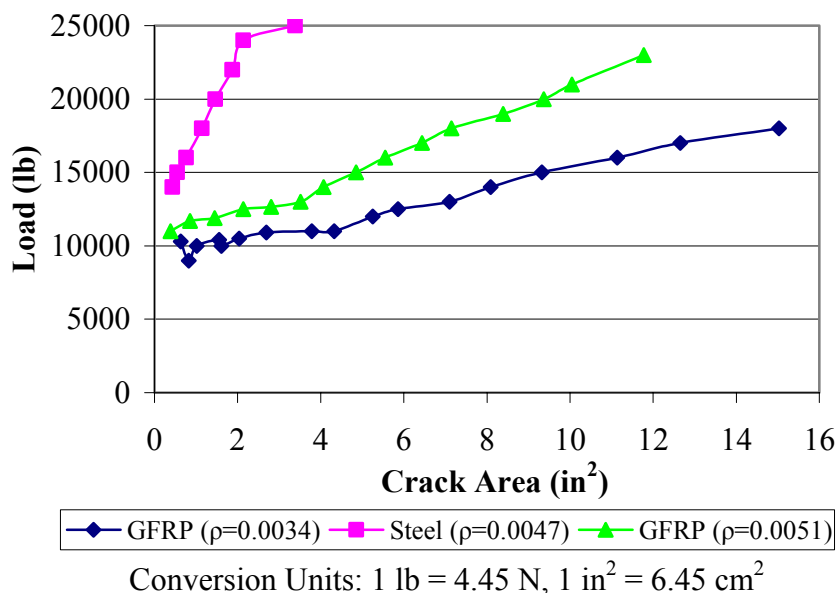


Figure 4.24. Phase III Load vs. Crack Area for 23.25”x7”x78” Panels

The crack control results of the largest panel size are presented in Figure 4.25. These four panel tests have produced excellent results for GFRP and steel comparison. As expected, as the GFRP reinforcement ratio increased the crack area decreased for a given flexural load. As you can see, when comparing the steel and GFRP panels of similar low reinforcement ratios, the panel with steel reinforcement has better crack control. Similar to the small panel tests, a GFRP reinforcement ratio twice as large as

steel yields similar crack control characteristics. Figure 4.25 shows the panel with a steel reinforcement ratio of 0.0022 performing similar to a panel with a GFRP ratio of 0.0037, yet not as well as the panel with a GFRP ratio of 0.0056.

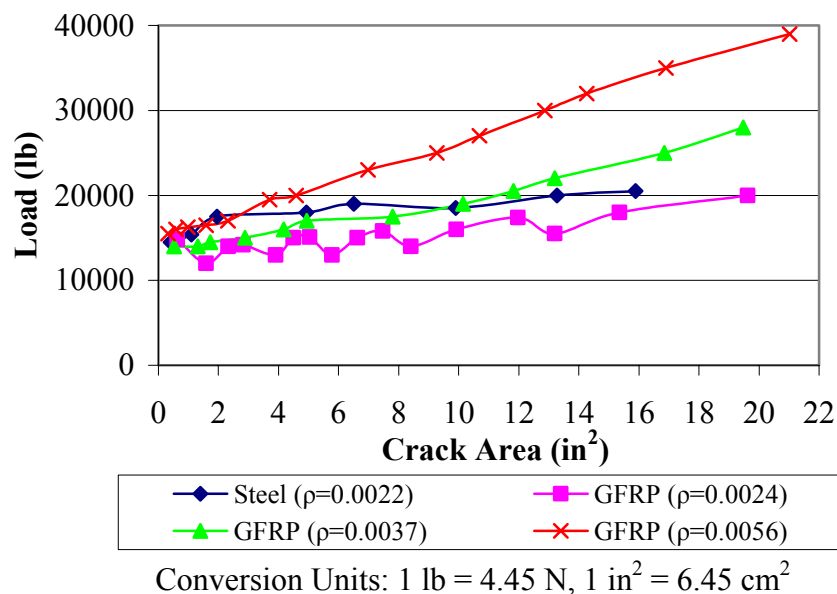


Figure 4.25. Phase III Load vs. Crack Area for 32''x7''x78'' Panels

The following three figures plot load vs. mid-span deflection for the three panel sizes. Similar to the previous three graphs, each graph contained at least two plots for GFRP and one plot for steel reinforcement for comparison between steel and GFRP. As illustrated in all three figures, panels reinforced with GFRP have higher mid-span deflections than panels reinforced with steel rebar at similar loads. Figure 4.26 and Figure 4.28 provides an excellent comparison to determine an equivalent reinforcement ratio between GFRP and steel for mid-span deflection. For both figures, approximately two and half times more GFRP area is needed to provide similar deflection

characteristics for panels reinforced with steel. For example, Figure 4.26 shows a panel with a steel reinforcement ratio of 0.0016 performing very similar to a GFRP panel of 0.0040. Likewise, Figure 4.28 shows the panel with a steel reinforcement ratio of 0.0022 performing slightly less than a panel with a GFRP ratio of 0.0056. Both of these examples conclude that two and a half times more GFRP reinforcement area is needed compared to steel reinforcement. Unfortunately, the analysis of Figure 4.27 is more difficult since the steel reinforcement ratio is higher or very similar to the two GFRP reinforcement ratios. The results of the three panels are as expected, yet no equivalent GFRP ratio compared to steel can be selected.

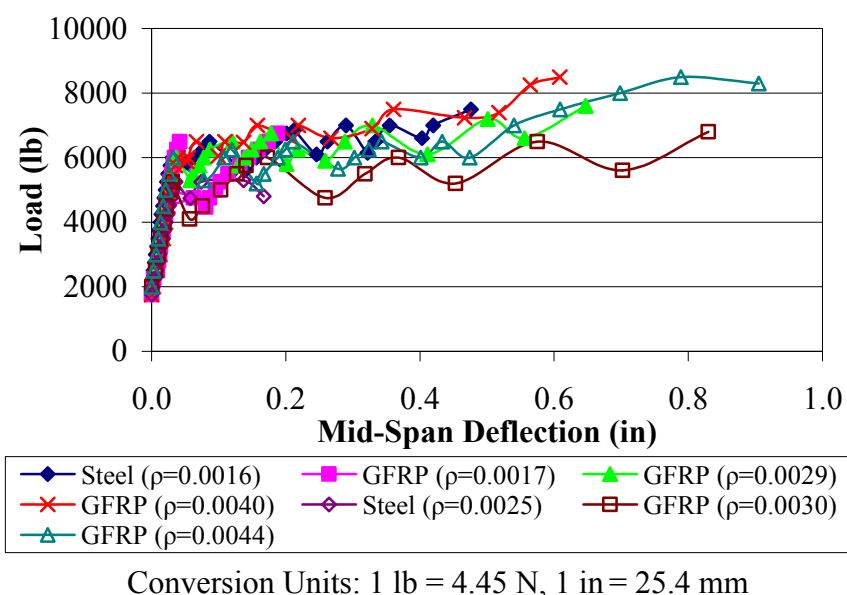


Figure 4.26. Phase III Load vs. Mid-Span Deflection for 23.25''x5''x78'' Panels

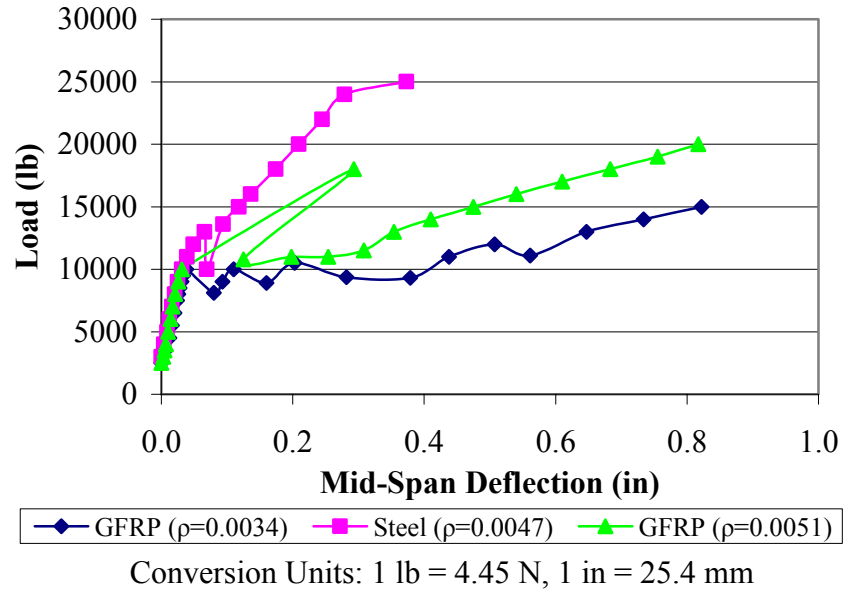


Figure 4.27. Phase III Load vs. Mid-Span Deflection for 23.25''x7''x78'' Panels

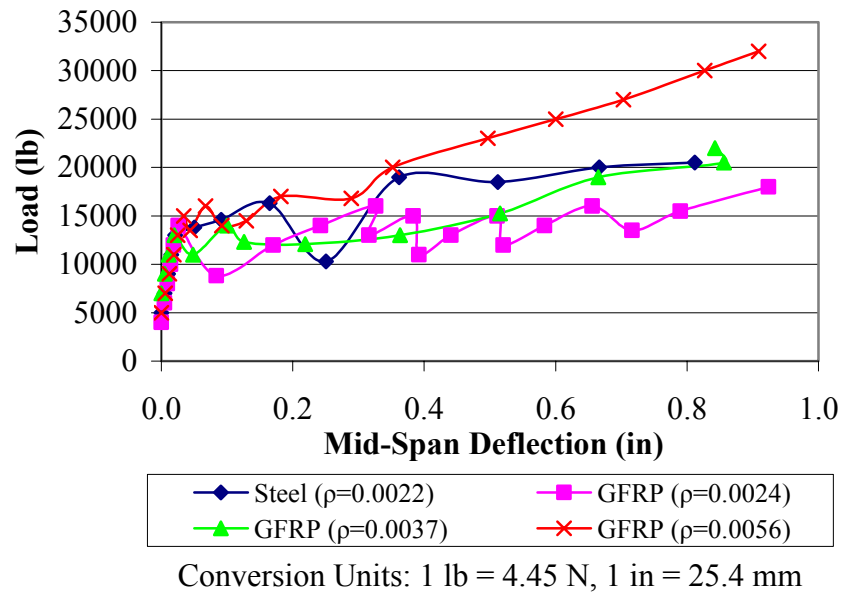


Figure 4.28. Phase III Load vs. Mid-Span Deflection for 32''x7''x78'' Panels

4.7. SUMMARY

This section has compared the crack control characteristics of concrete reinforced with GFRP to the acceptable benchmark of steel rebar through three testing phases in which specimens were subjected to tensile and flexural loading. Phase I results shows GFRP specimen resulting crack widths three times larger than specimens of similar amounts of steel reinforcement when subjected to restraint and environmental cycling at early-age. The environmental conditioning subjected the specimens to increased temperature cycles, low relative humidity levels, and increased wind velocities which all increased the rate of drying shrinkage and temperature effects. Approximately 40% or more of the total drying shrinkage was estimated to occur within the first week. Phase II results present steel reinforcement being 1.3 times more efficient at crack control than GFRP at later-age. Finally, Phase III concluded that twice as much GFRP reinforcement is required to achieve similar crack control characteristics as steel when subjected to flexural loading. Also, two and half times more GFRP reinforcement yields similar mid-span deflection characteristics as steel.

Limitation of the Research Study Undertaken: Before any significant conclusions or recommendation can be made based on the results of this research study, the limitation of the project must carefully be addressed. Since there is currently no standard test method for secondary reinforcement, the results and conclusions from this research are limited to the parameters of the test program. The primary limitation of this study includes rebar manufacturer. As previously mentioned, the GFRP rebar used to reinforce all of the test specimens were provided by a single manufacturer. Variables such as tensile strength, modulus of elasticity and deformation pattern significantly affect

the crack control capabilities of a given GFRP rebar. Therefore, additional laboratory and field testing with several types of GFRP rebar is needed to develop an accurate empirical secondary reinforcement ratio for GFRP.

5. CONCLUSIONS AND FUTURE RESEARCH

5.1. CONCLUSIONS

The objective of this research project was to investigate the development of an empirical secondary reinforcement ratio for FRP based on experimental tests. Emphasis must be placed on the fact that the results and conclusions drawn from this study are limited to a single GFRP rebar type evaluated subjected to three phases of study. The following conclusions are drawn from the experimental results of this investigation:

- A significant amount of drying shrinkage, temperature, and plastic shrinkage cracks can be eliminated by following proper curing procedures.
- For a given reinforcement ratio, specimens reinforced with steel provide better crack control than specimens reinforced with GFRP.
- Specimens reinforced with steel experience less deformation than specimens reinforced with the same reinforcement ratio of GFRP.
- As the GFRP reinforcement ratio increases, the total crack area decreases.
- Larger crack widths are produced as the modulus of elasticity of the reinforcement decreases.
- For specimens subjected to a given load, the strain in the reinforcement decreases as the reinforcement ratio increases.
- Compared to steel, three times more GFRP reinforcement is required to produce similar crack control characteristics when subjected to similar axial restraint loads at early-age.

- At later-age, steel reinforcement is 1.3 times more efficient (load/area) at crack control than GFRP reinforcement.
- When tested in flexure, twice as much GFRP reinforcement is required to produce similar crack control as steel reinforcement.
- Two and a half times more GFRP reinforcement yields similar mid-span deflection characteristics as steel when subjected to flexure.
- Crack width requirements for steel are largely governed by the time of corrosion and appearance. Since FRP does not corrode, crack width limitations are governed more by aesthetic appearance in lieu of durability related concerns. For this reason, the exterior crack width limitation for FRP can be relaxed from 0.0016 in. (0.33 mm) to ACI's interior limitation of 0.0013 in. (0.41 mm); crack widths 1.25 times larger.
- Based on the three phases of study and GFRP rebar used in this experimental program, the FRP secondary reinforcement ratio equation listed in the ACI 440-03 guideline is overly conservative. The crack control characteristics of a particular rebar is unable to be accurately estimated based solely on material stiffness and tensile strength. For most cases, the minimum reinforcement ratio will be governed by the current 0.0036 upper limitation which appears excessive, in particular where restraint levels are low.

5.2. FUTURE RESEARCH

One objective of the research study was to develop a test method for future research to be performed so eventually sufficient data will be available to develop an

empirical secondary reinforcement ratio for FRP based on a sufficient data base of information. The following list is recommendations for future research:

- Perform additional laboratory testing of specimens reinforced with several types of GFRP rebar from various manufacturers (varying tensile strength, modulus of elasticity, deformation pattern and texture, etc).
- Evaluate specimens with larger cross-sectional areas so the reinforcement ratios are between 0.0018 and 0.0060.
- Determine the effects of concrete clear cover on crack control by varying the reinforcement placement.
- Vary the specimen length to determine the effects of the bond length between the concrete and reinforcement on crack control.
- Test a series of specimens with the same reinforcement ratio but of varying rebar sizes and spacing to determine its effects on crack width and spacing (e.g. 5 - #3 GFRP rebar compared to 2 - #5 GFRP rebar).
- Investigate the influence of varied restraint levels in combination with thermal changes (ΔT) and shrinkage.

APPENDIX A
SPECIMEN ULTIMATE CRACK PATTERNS

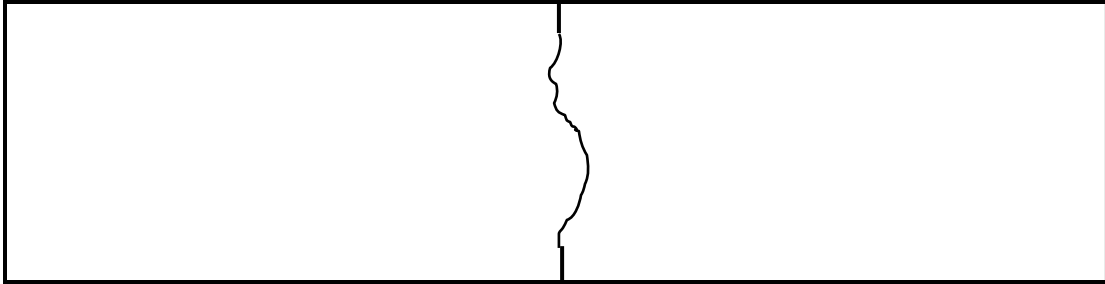


Figure A.1. Phase I: 2-#3 Steel Crack Pattern

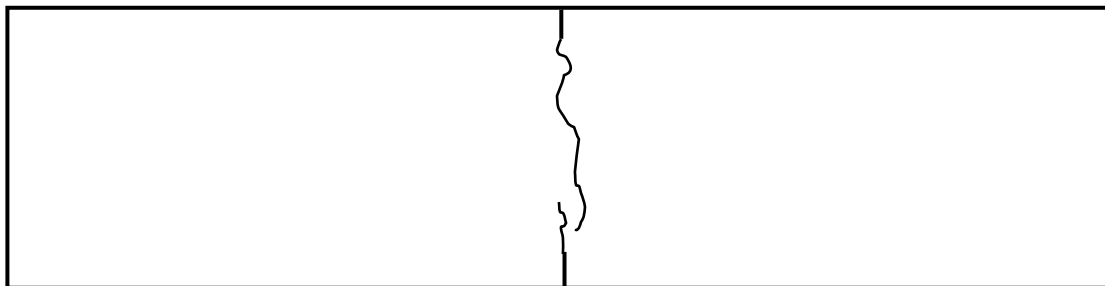


Figure A.2. Phase I: 2-#3 GFRP Crack Pattern

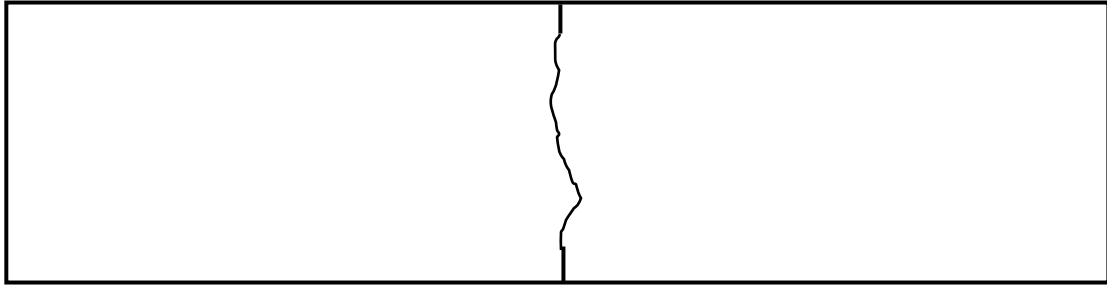


Figure A.3. Phase I: 3-#3 GFRP Crack Pattern

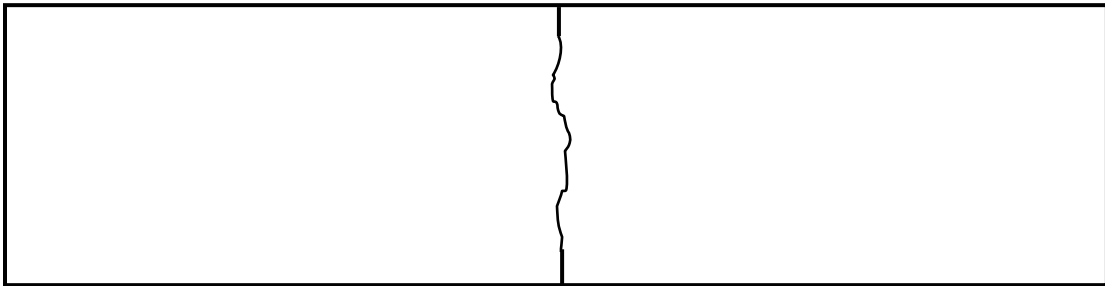


Figure A.4. Phase I: 4-#3 GFRP Crack Pattern

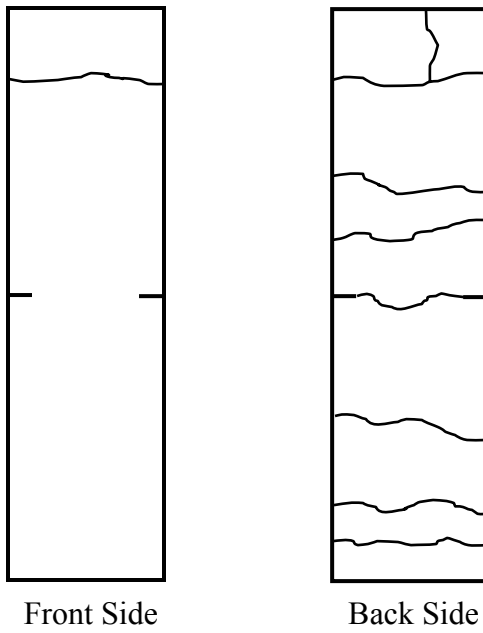


Figure A.5. Phase II: 4-#3 Steel Crack Pattern

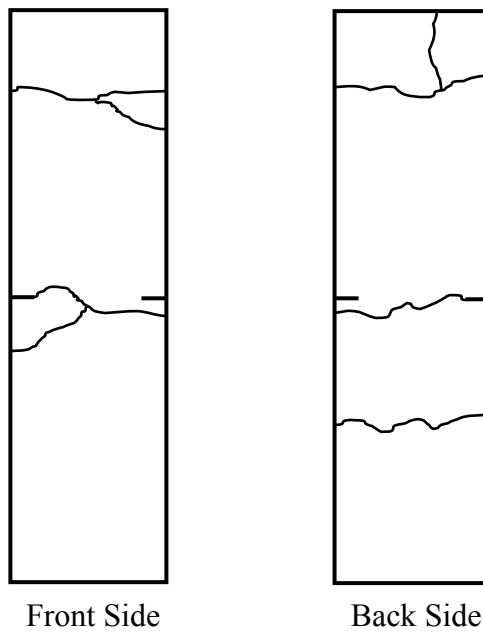


Figure A.6. Phase II: 2-#3 GFRP Crack Pattern

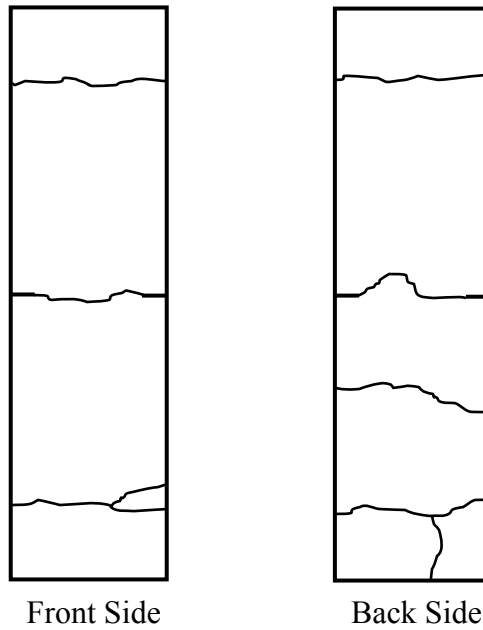


Figure A.7. Phase II: 3-#3 GFRP Crack Pattern

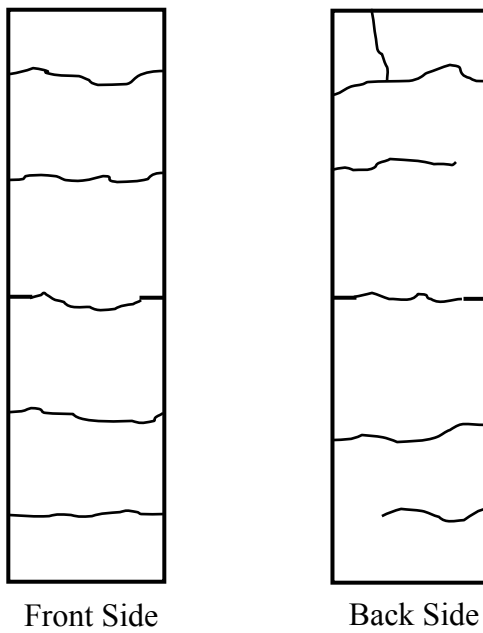


Figure A.8. Phase II: 4-#3 GFRP Crack Pattern

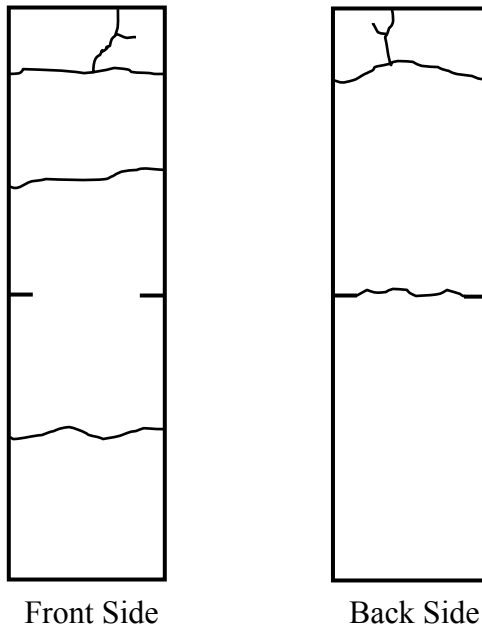


Figure A.9. Phase II: 2-#4 Steel Crack Pattern

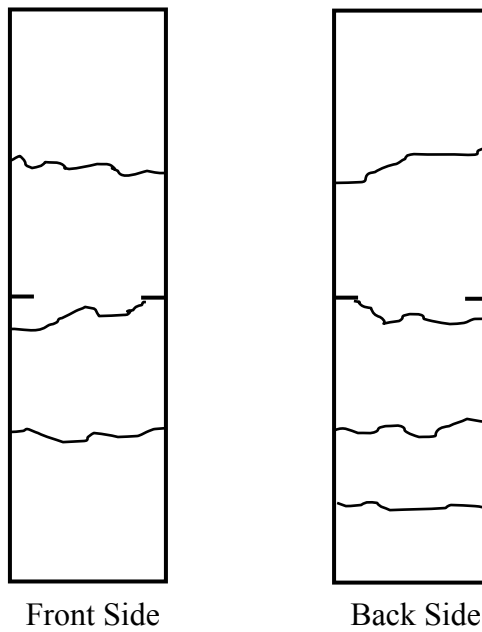


Figure A.10. Phase II: 2-#4 GFRP Crack Pattern

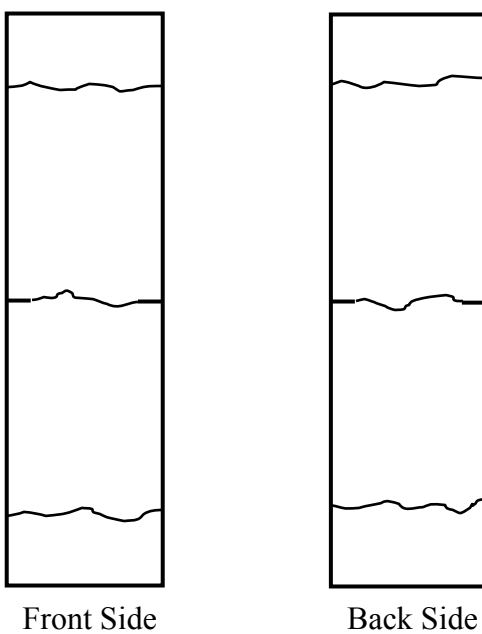


Figure A.11. Phase II: 3-#4 GFRP Crack Pattern

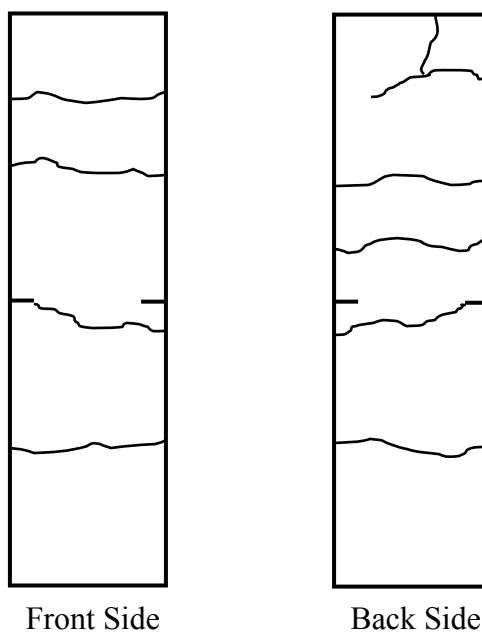


Figure A.12. Phase II: 4-#4 GFRP Crack Pattern

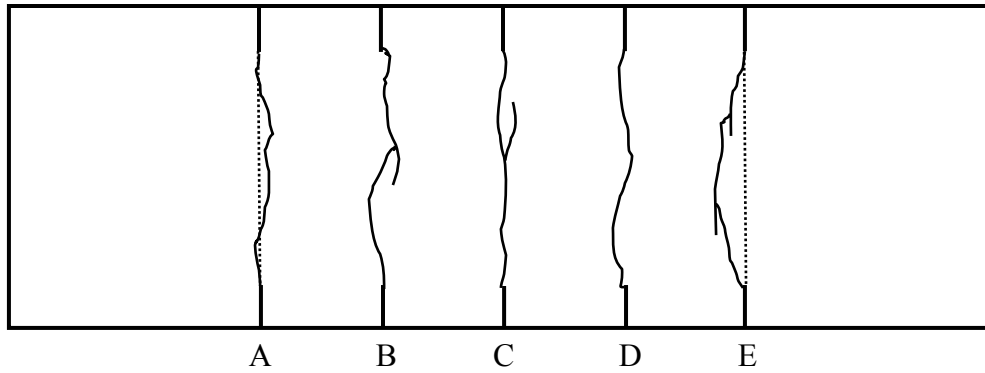


Figure A.13. Phase III: Slab 1 (3-#2 Steel) Crack Pattern

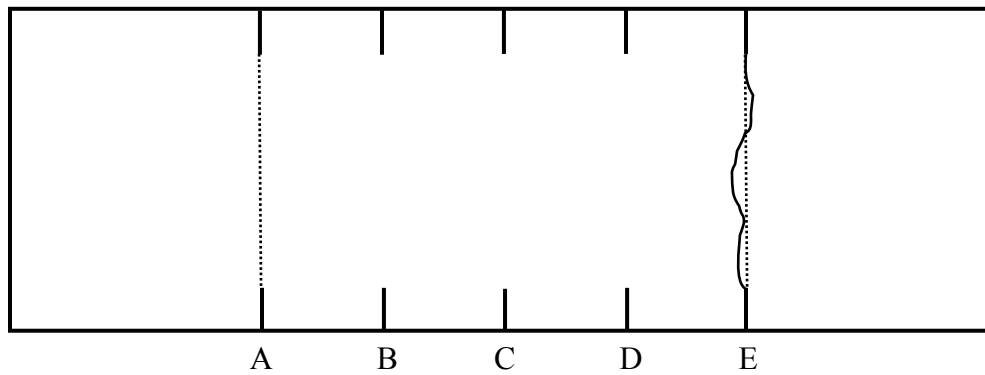


Figure A.14. Phase III: Slab 2 (3-#2 GFRP) Crack Pattern

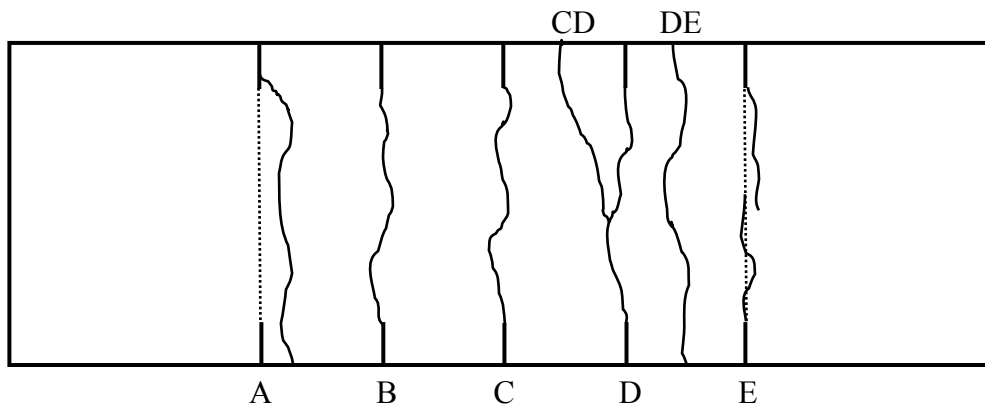


Figure A.15. Phase III: Slab 3 (5-#2 GFRP) Crack Pattern

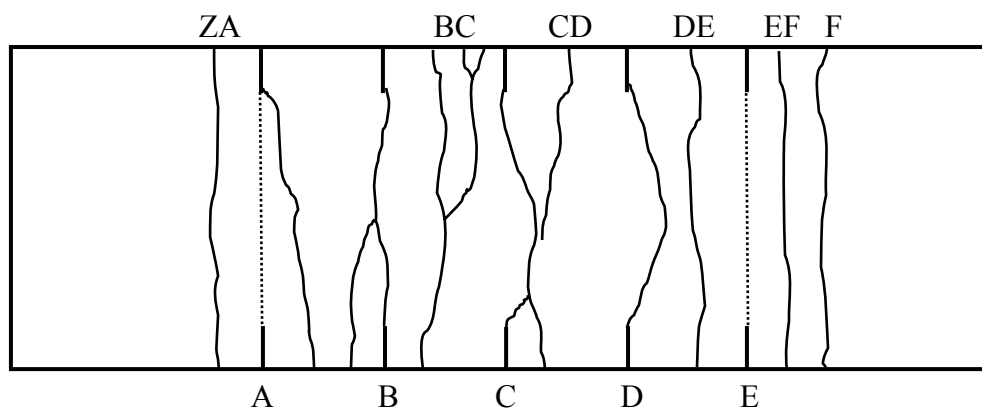


Figure A.16. Phase III: Slab 4 (7-#2 GFRP) Crack Pattern

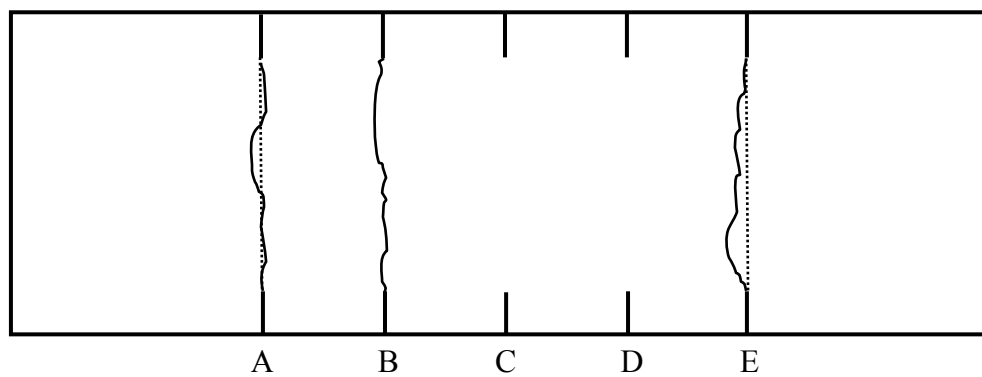


Figure A.17. Phase III: Slab 9 (2-#3 Steel) Crack Pattern

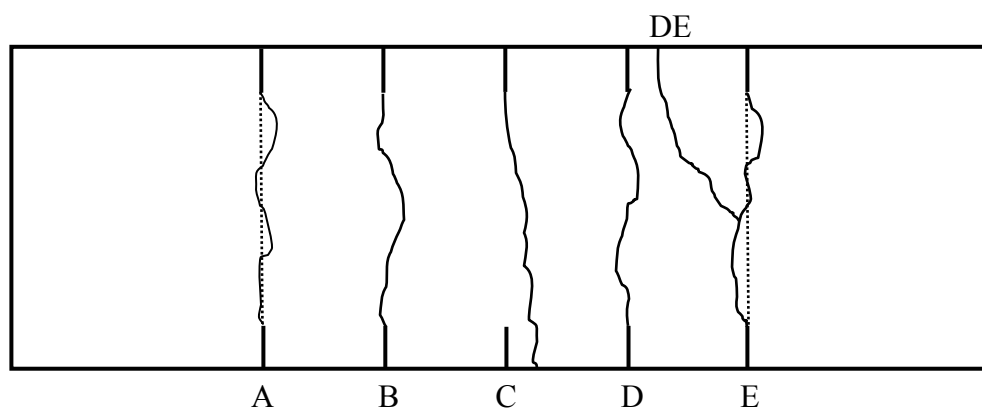


Figure A.18. Phase III: Slab 10 (2-#3 GFRP) Crack Pattern

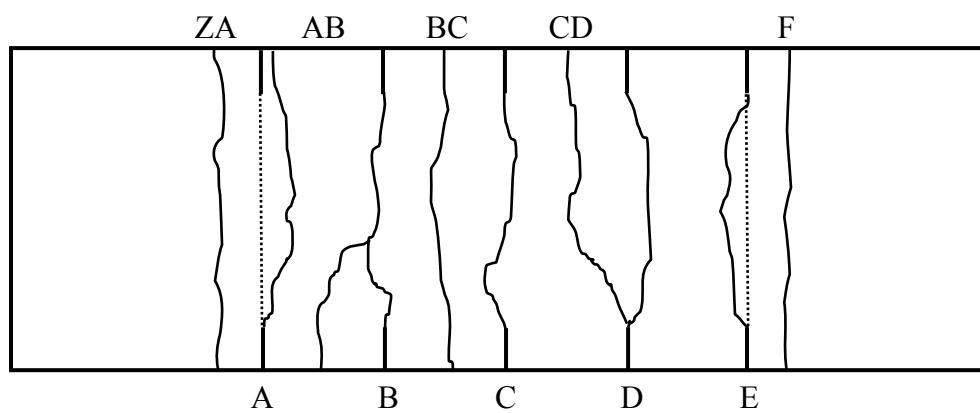


Figure A.19. Phase III: Slab 11 (3-#3 GFRP) Crack Pattern

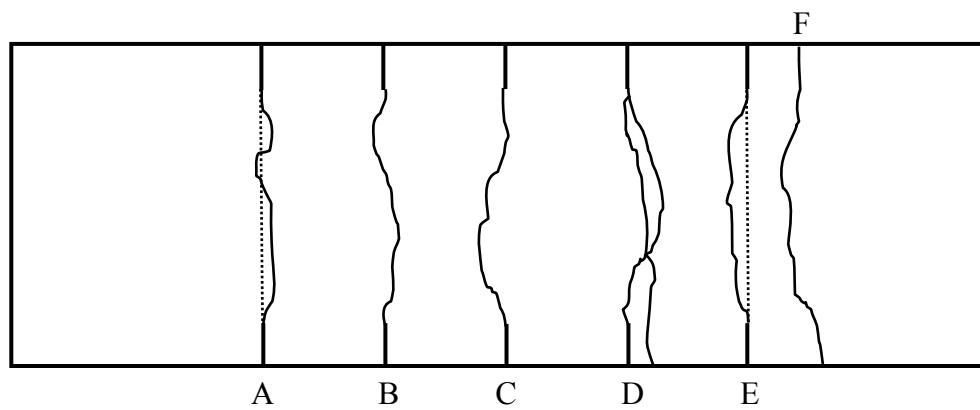


Figure A.20. Phase III: Slab 12 (2-#4 GFRP) Crack Pattern

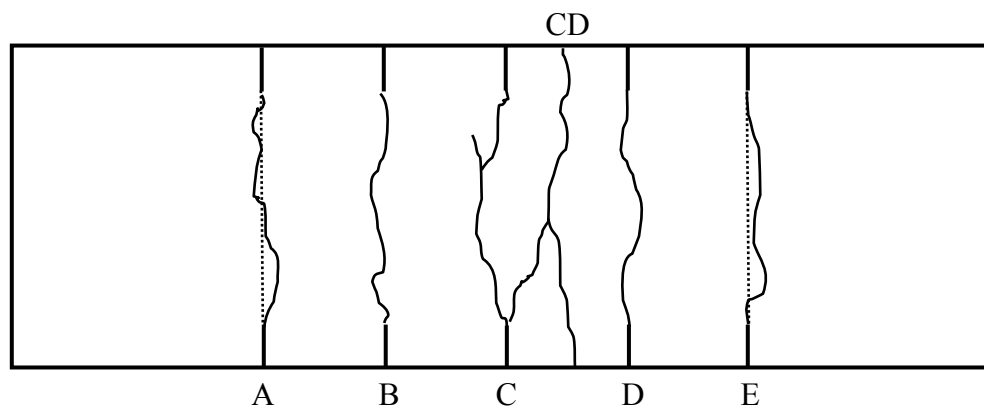


Figure A.21. Phase III: Slab 5 (2-#5 Steel) Crack Pattern

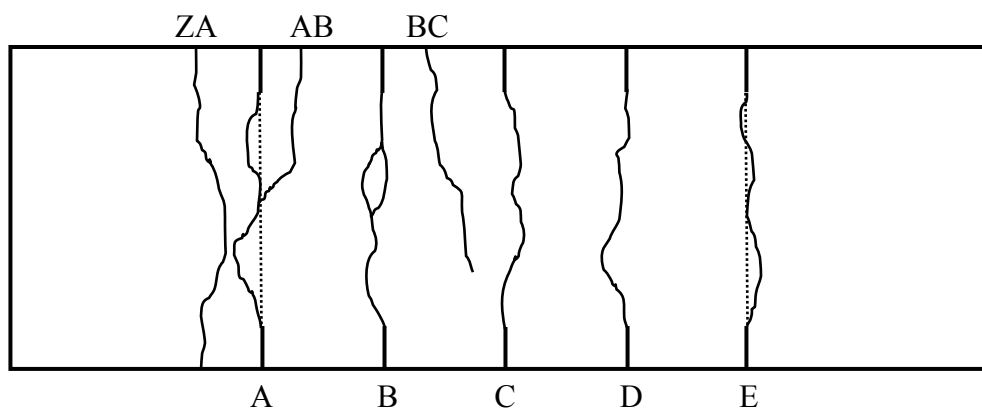


Figure A.22. Phase III: Slab 6 (2-#5 GFRP) Crack Pattern

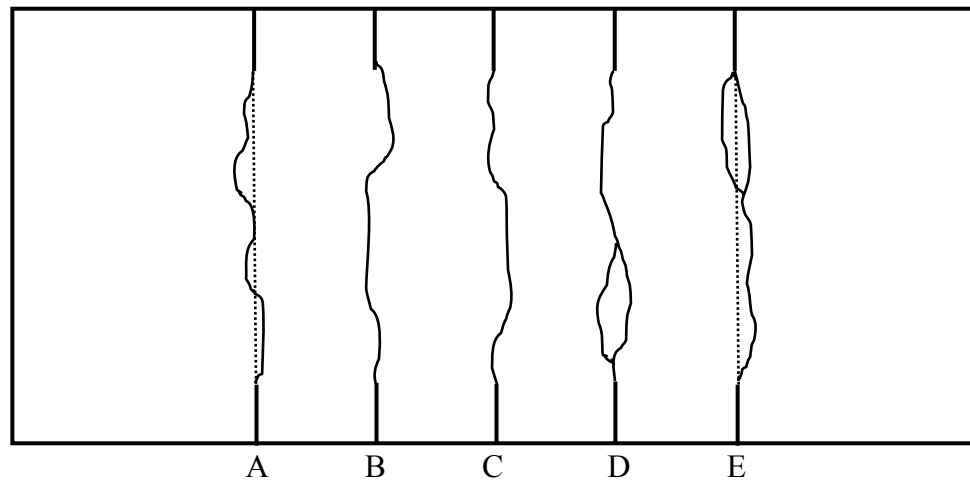


Figure A.23. Phase III: Slab 13 (2-#4 Steel) Crack Pattern

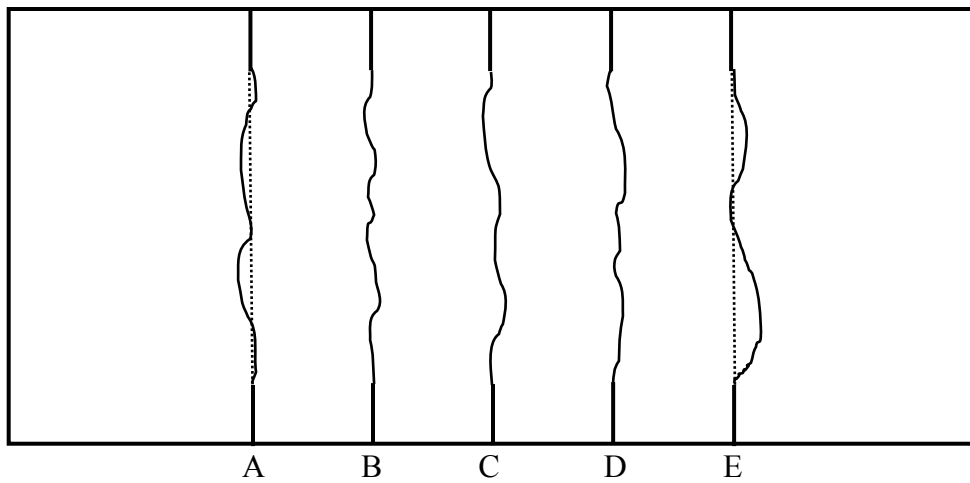


Figure A.24. Phase III: Slab 14 (2-#4 GFRP) Crack Pattern

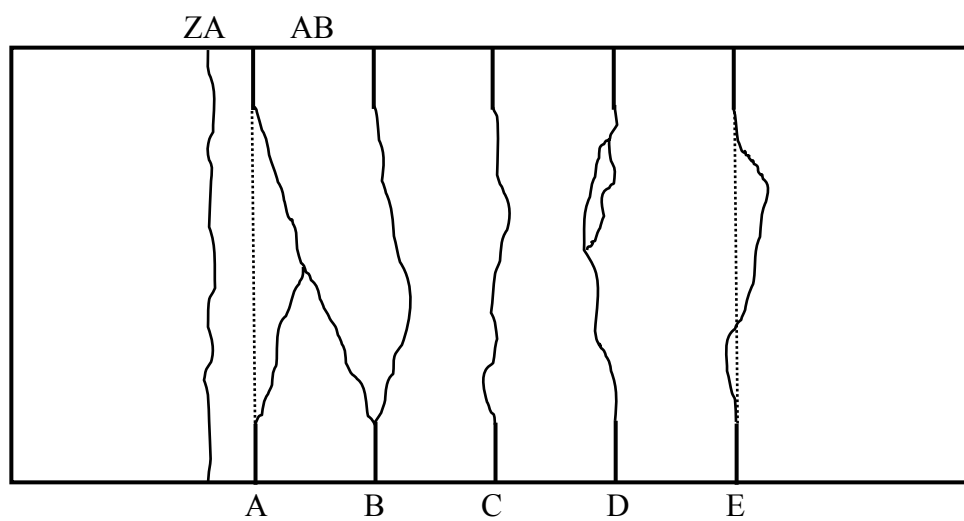


Figure A.25. Phase III: Slab 7 (2-#5 GFRP) Crack Pattern

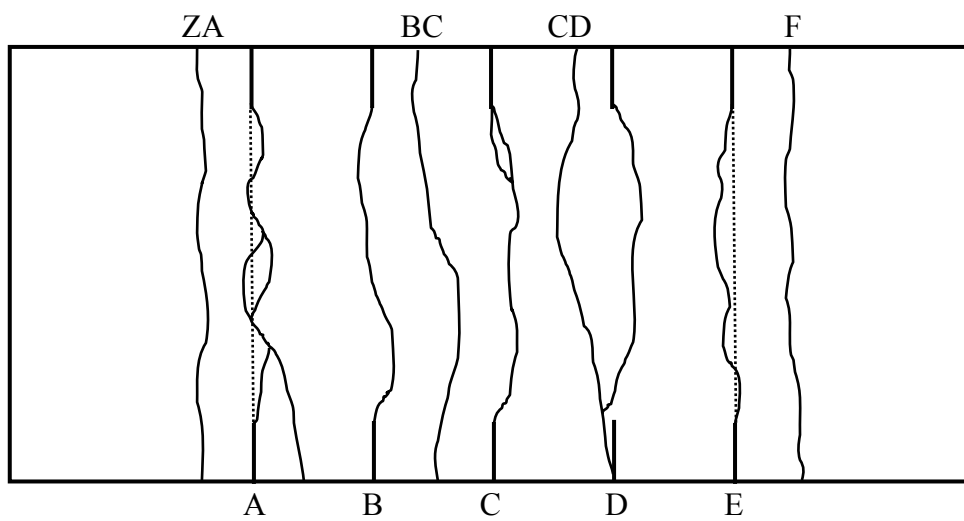


Figure A.26. Phase III: Slab 8 (3-#5 GFRP) Crack Pattern

APPENDIX B
PHASE III DEFLECTION AND LOAD VS. STRAIN GRAPHS

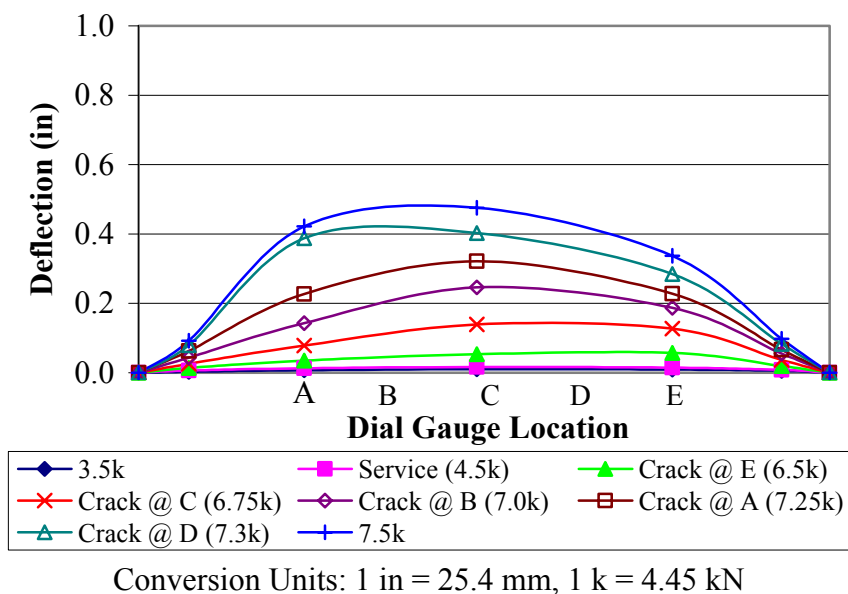


Figure B.1. Phase III: Slab 1 (3-#2 Steel) Deflection Graph

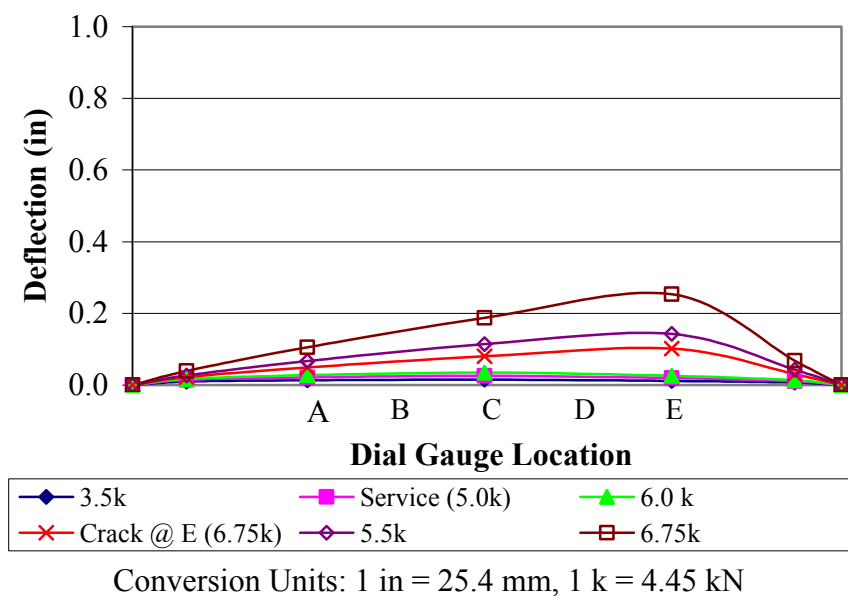
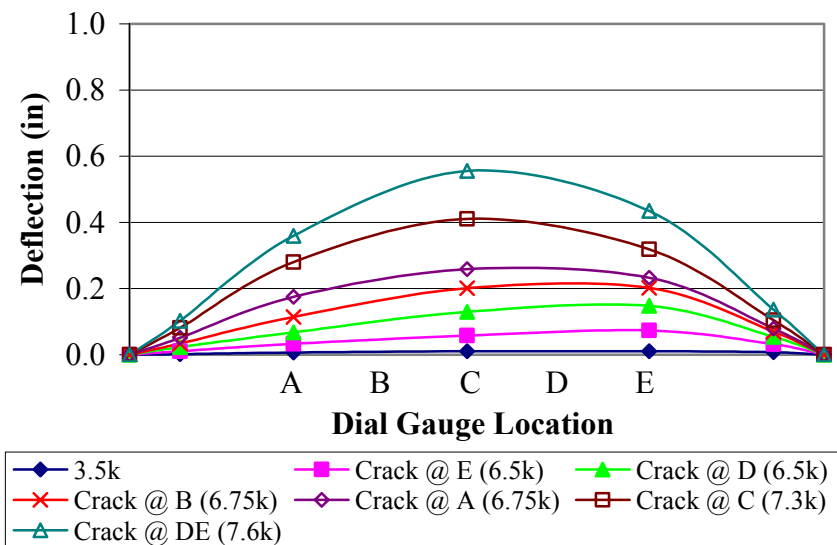
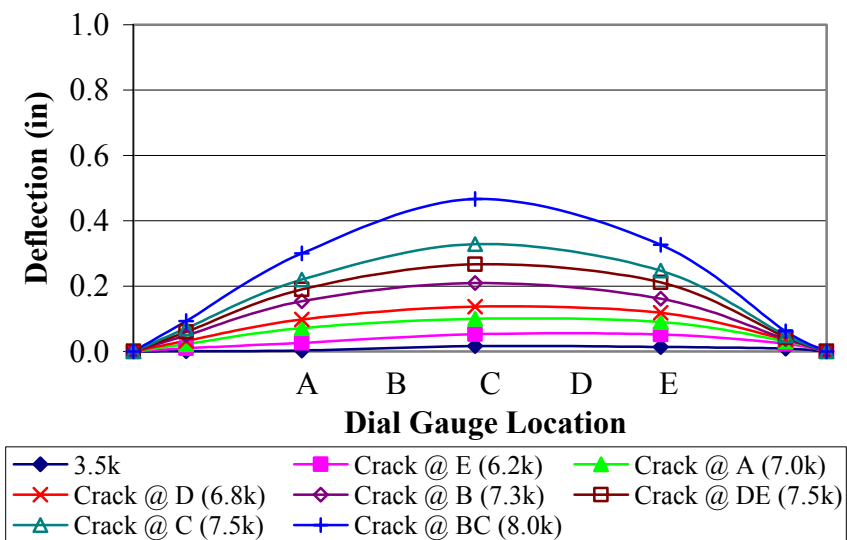


Figure B.2. Phase III: Slab 2 (3-#2 GFRP) Deflection Graph



Conversion Units: 1 in = 25.4 mm, 1 k = 4.45 kN

Figure B.3. Phase III: Slab 3 (5-#2 GFRP) Deflection Graph



Conversion Units: 1 in = 25.4 mm, 1 k = 4.45 kN

Figure B.4. Phase III: Slab 4 (7-#2 GFRP) Deflection Graph

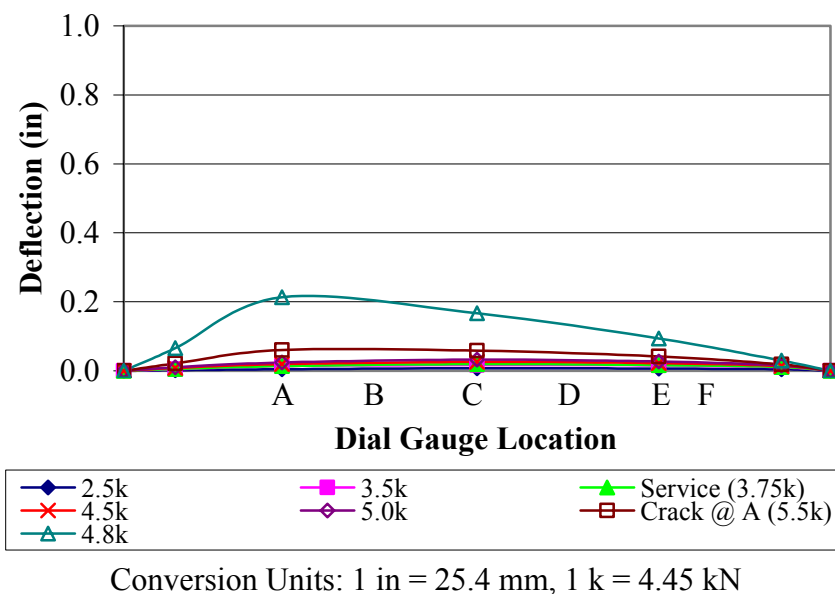


Figure B.5. Phase III: Slab 9 (2-#3 Steel) Deflection Graph

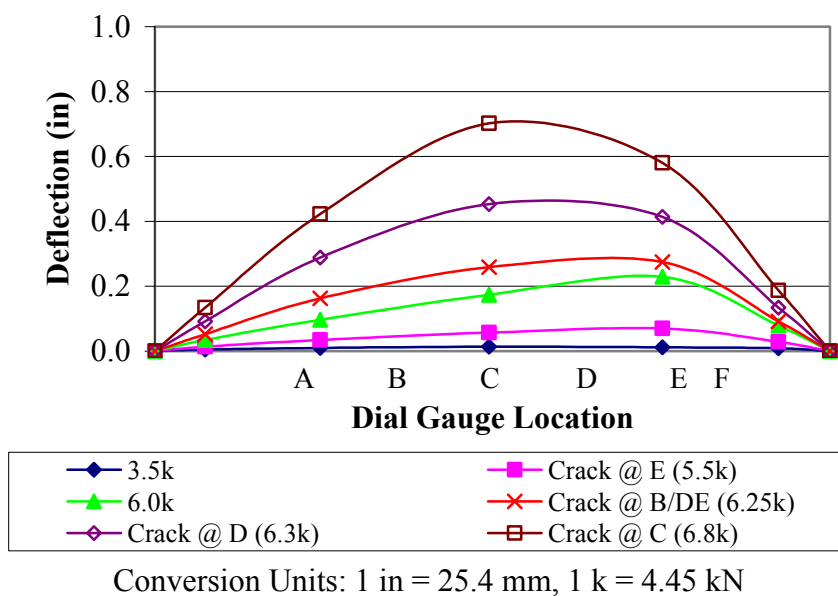


Figure B.6. Phase III: Slab 10 (2-#3 GFRP) Deflection Graph

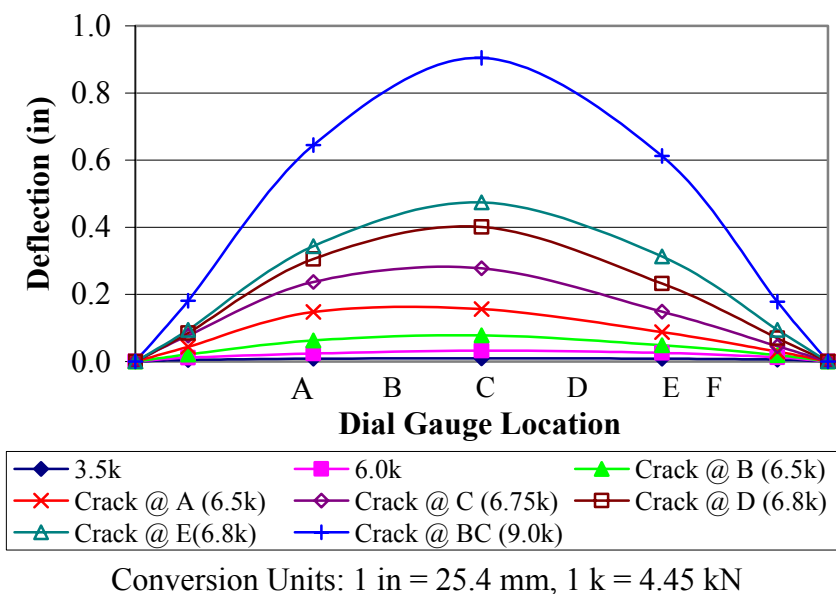


Figure B.7. Phase III: Slab 11 (3-#3 GFRP) Deflection Graph

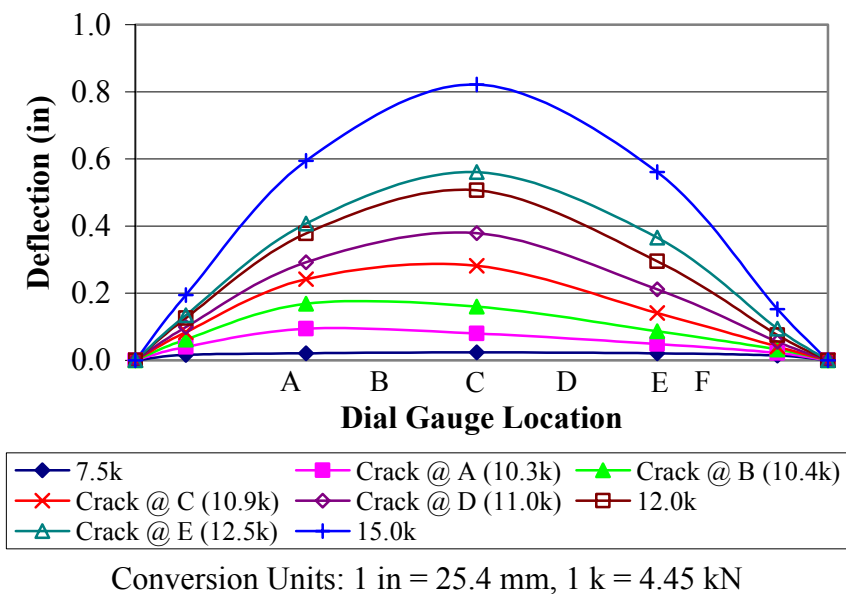
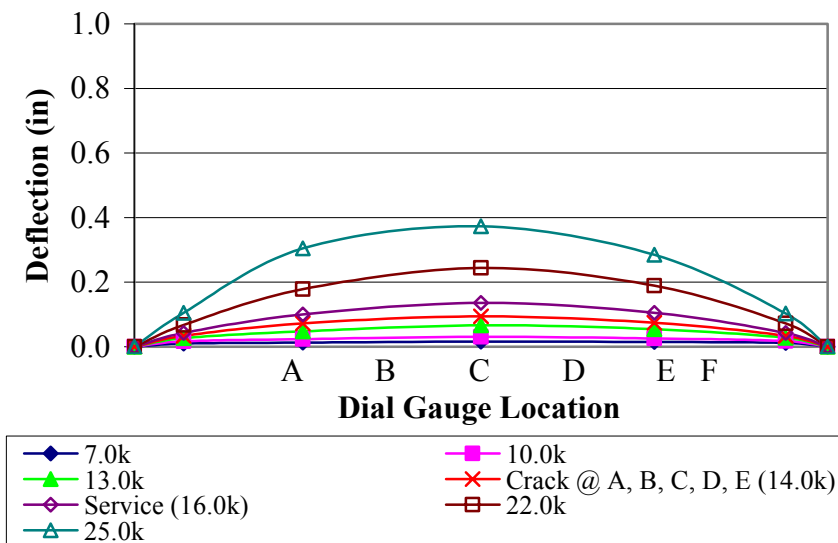
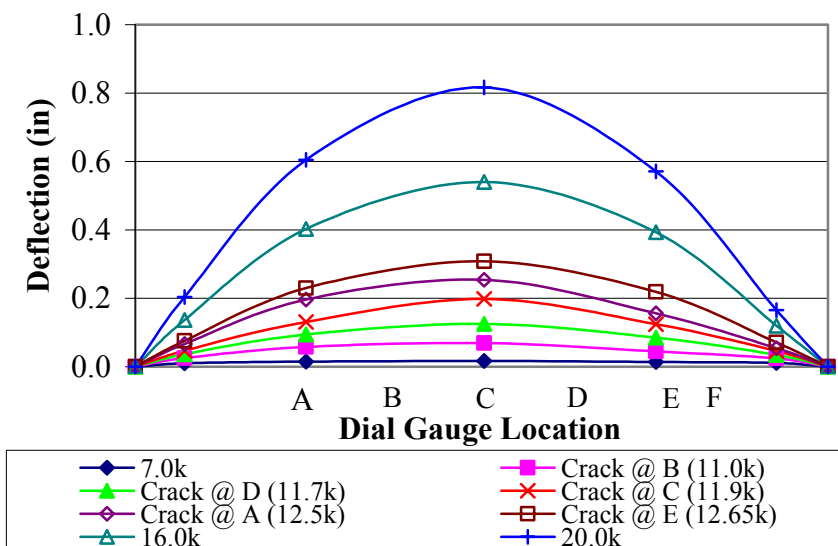


Figure B.8. Phase III: Slab 12 (2-#4 GFRP) Deflection Graph



Conversion Units: 1 in = 25.4 mm, 1 k = 4.45 kN

Figure B.9. Phase III: Slab 5 (2-#5 Steel) Deflection Graph



Conversion Units: 1 in = 25.4 mm, 1 k = 4.45 kN

Figure B.10. Phase III: Slab 6 (2-#5 GFRP) Deflection Graph

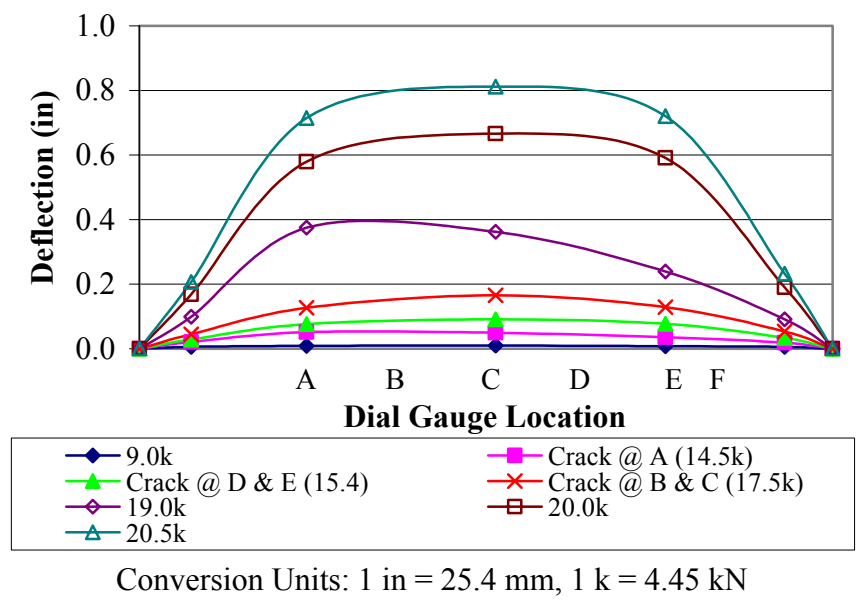


Figure B.11. Phase III: Slab 13 (2-#4 Steel) Deflection Graph

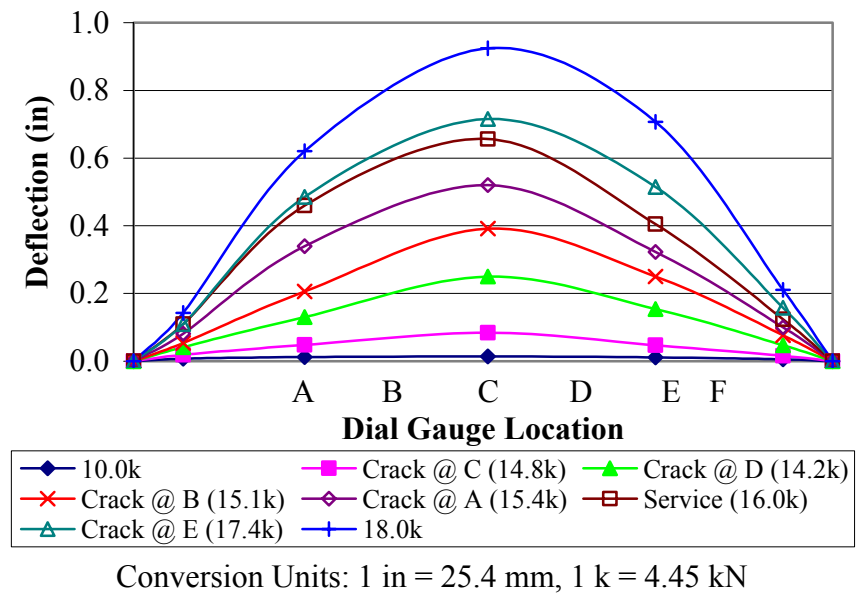


Figure B.12. Phase III: Slab 14 (2-#4 GFRP) Deflection Graph

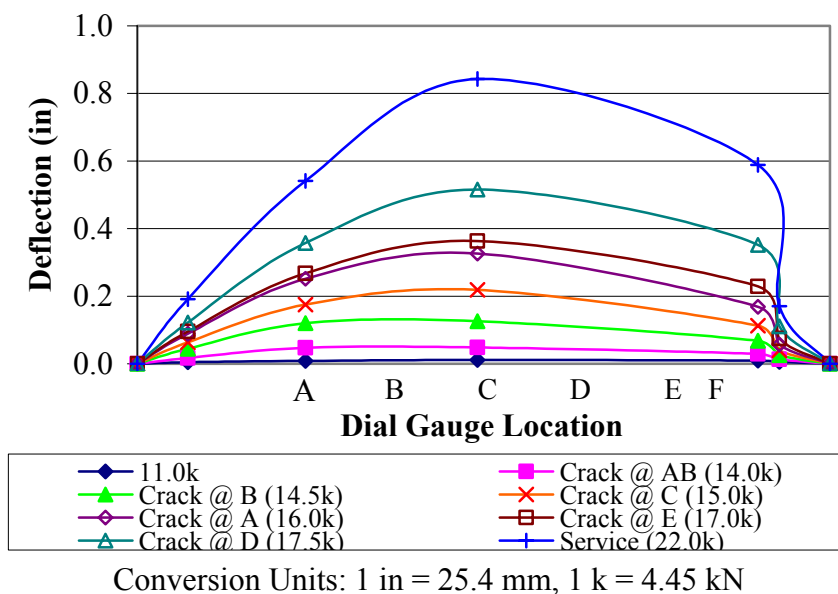


Figure B.13. Phase III: Slab 7 (2-#5 GFRP) Deflection Graph

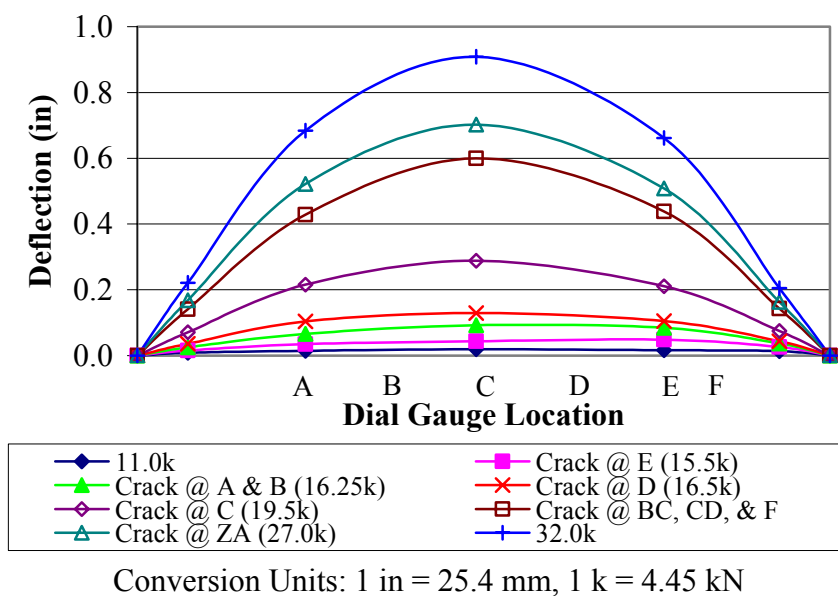


Figure B.14. Phase III: Slab 8 (3-#5 GFRP) Deflection Graph

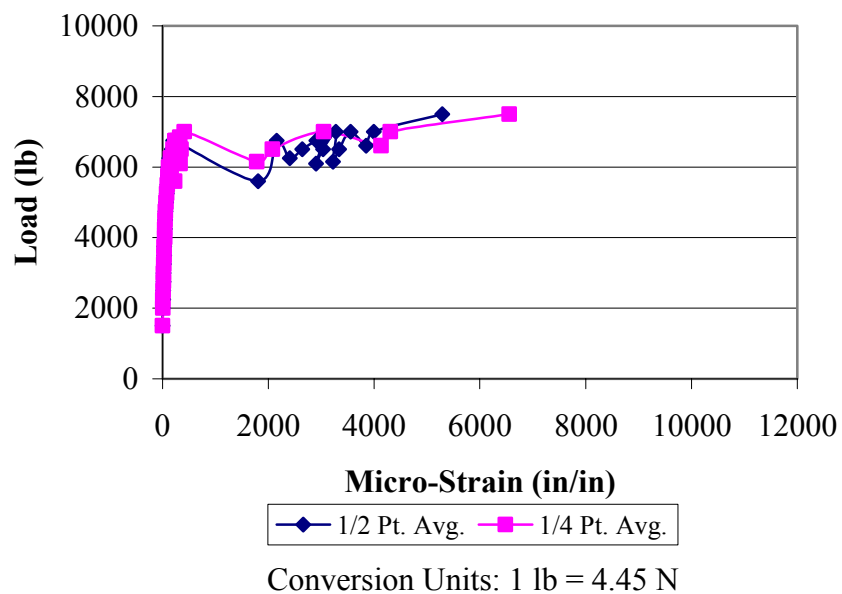


Figure B.15. Phase III: Slab 1 (3-#2 Steel) Load vs. Strain Graph

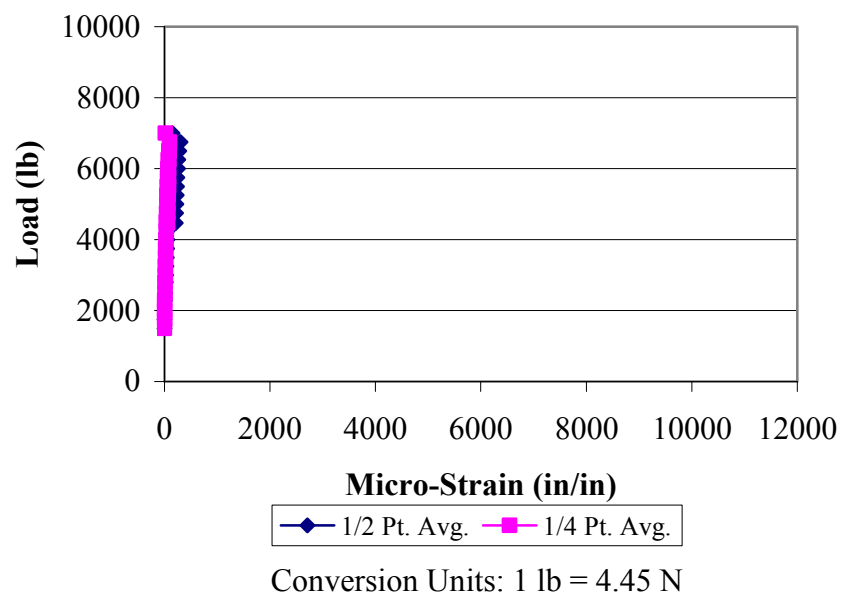


Figure B.16. Phase III: Slab 2 (3-#2 GFRP) Load vs. Strain Graph

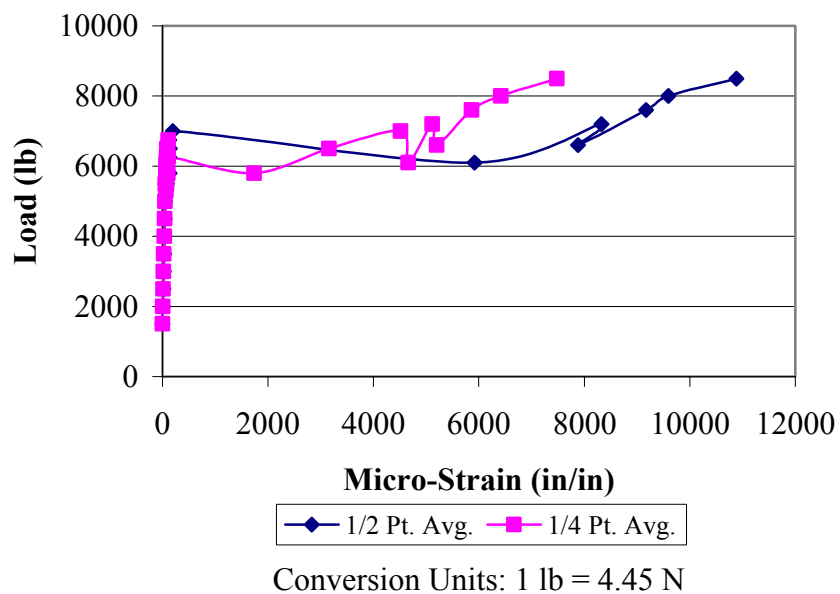


Figure B.17. Phase III: Slab 3 (5-#2 GFRP) Load vs. Strain Graph

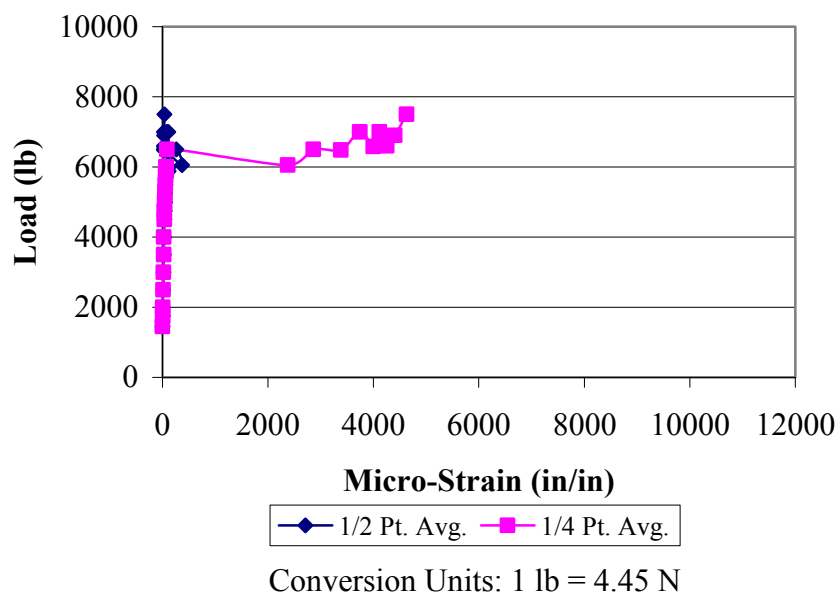


Figure B.18. Phase III: Slab 4 (7-#2 GFRP) Load vs. Strain Graph

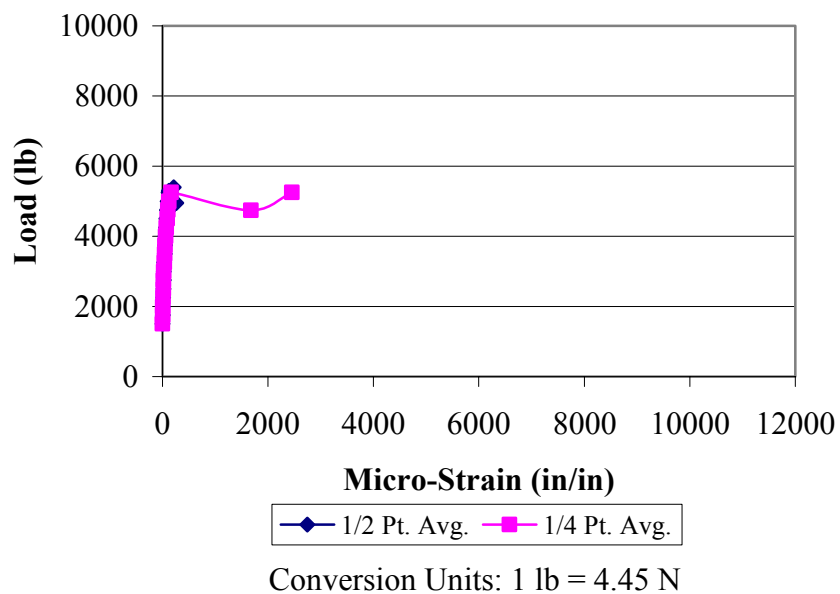


Figure B.19. Phase III: Slab 9 (2-#3 Steel) Load vs. Strain Graph

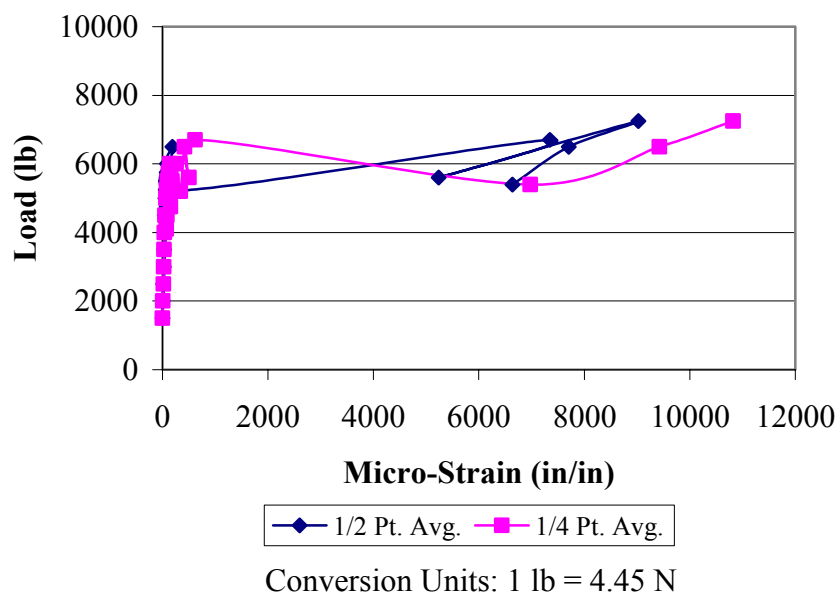


Figure B.20. Phase III: Slab 10 (2-#3 GFRP) Load vs. Strain Graph

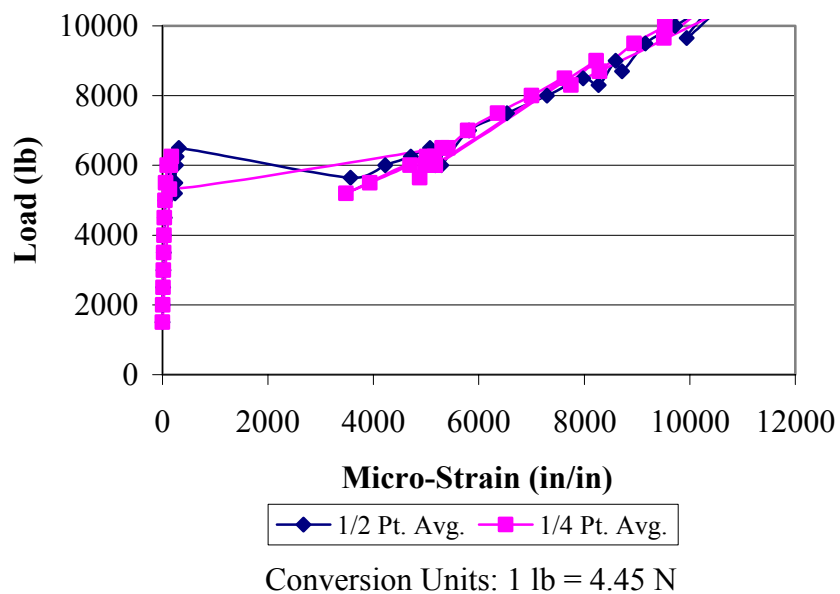


Figure B.21. Phase III: Slab 11 (3-#3 GFRP) Load vs. Strain Graph

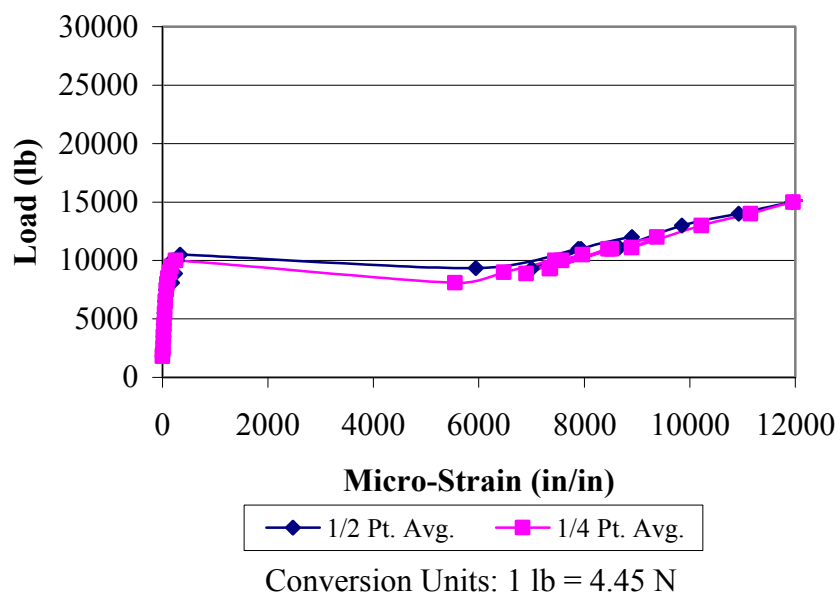


Figure B.22. Phase III: Slab 12 (2-#4 GFRP) Load vs. Strain Graph

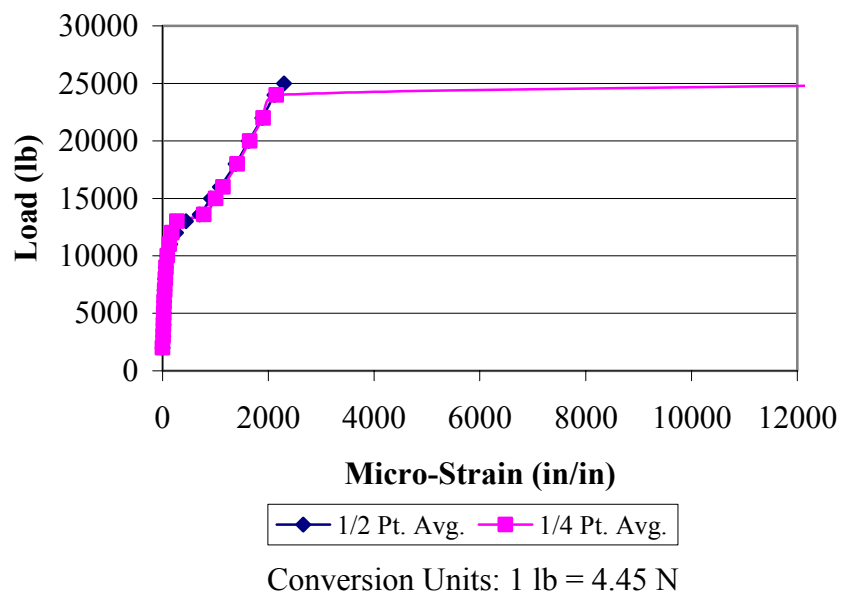


Figure B.23. Phase III: Slab 5 (2-#5 Steel) Load vs. Strain Graph

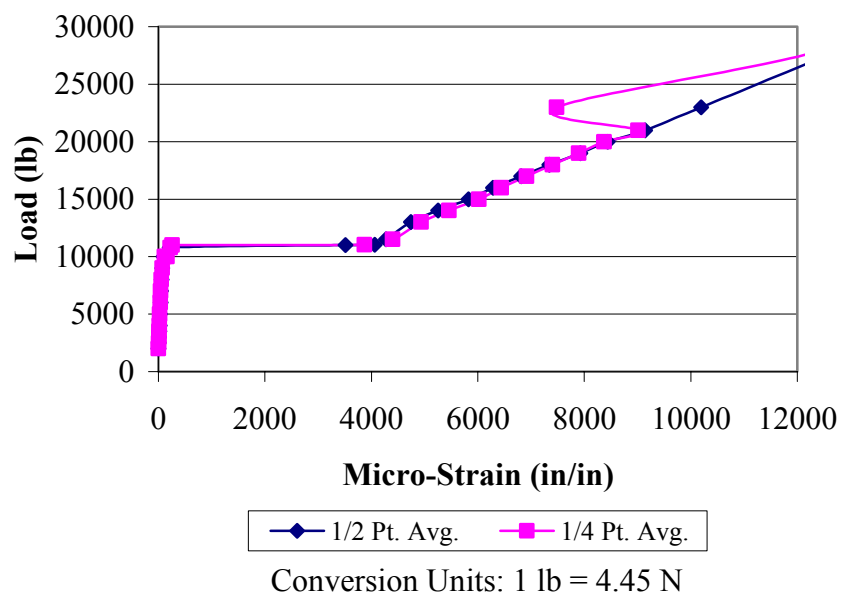


Figure B.24. Phase III: Slab 6 (2-#5 GFRP) Load vs. Strain Graph

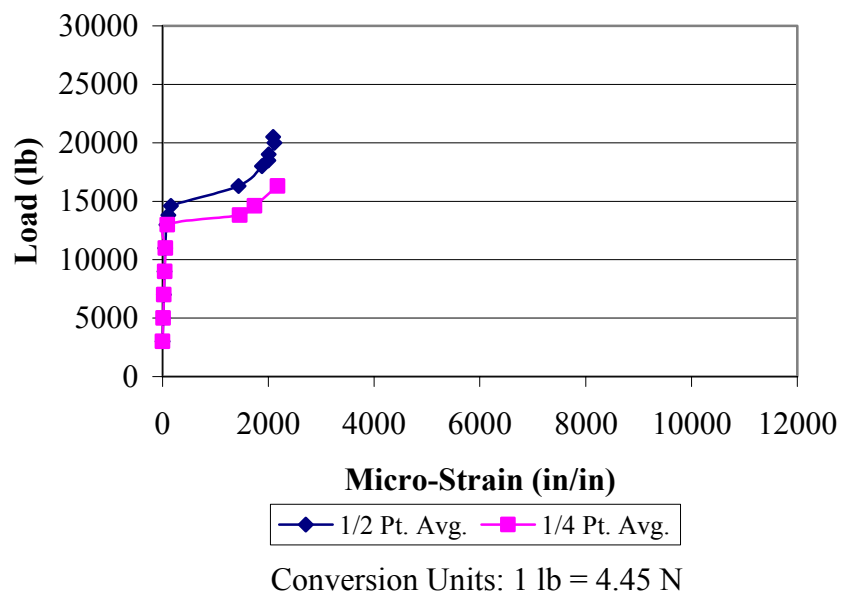


Figure B.25. Phase III: Slab 13 (2-#4 Steel) Load vs. Strain Graph

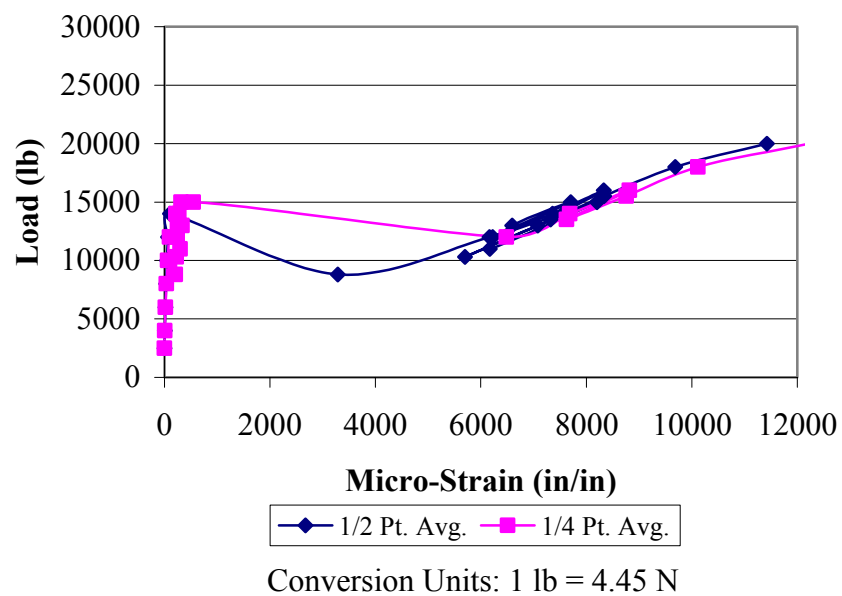


Figure B.26. Phase III: Slab 14 (2-#4 GFRP) Load vs. Strain Graph

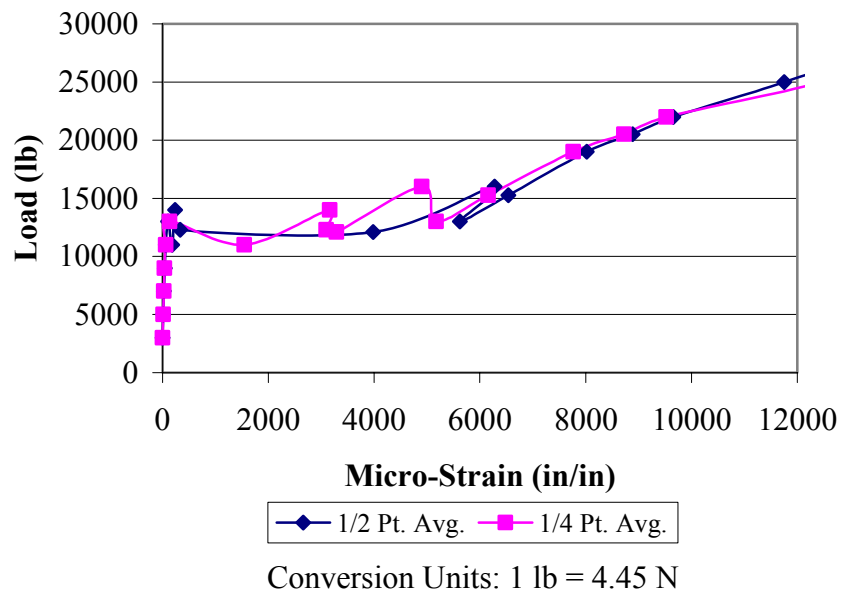


Figure B.27. Phase III: Slab 7 (2-#5 GFRP) Load vs. Strain Graph

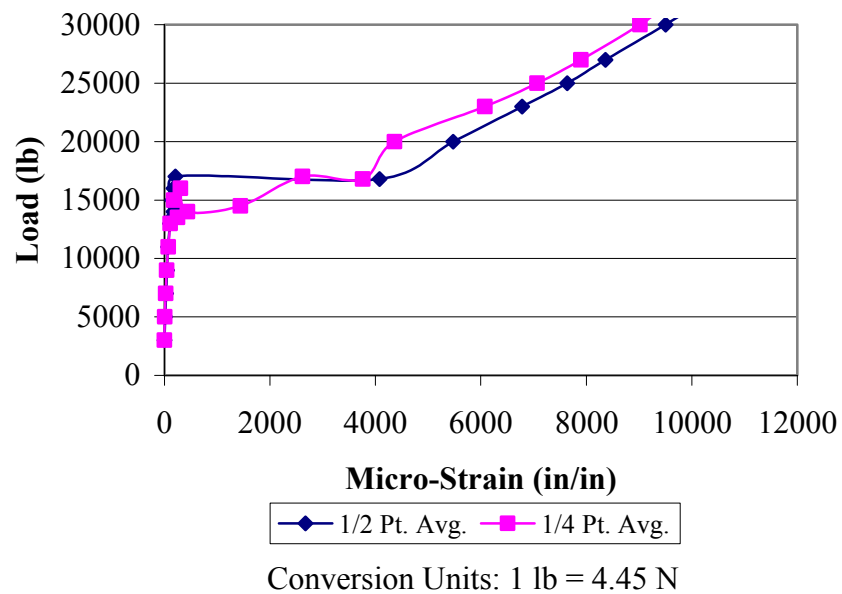


Figure B.28. Phase III: Slab 8 (3-#5 GFRP) Load vs. Strain Graph

BIBLIOGRAPHY

1. ACI Committee 224-89. "Control of Cracking in Concrete Structures (ACI 224R-90)," American Concrete Institute, Detroit, MI, 1991.
2. ACI Committee 318-02. "Building Code Requirements for Structural Concrete and Commentary (ACI 318R-02)," American Concrete Institute, Farmington Hills, MI, 2002.
3. ACI Committee 318-63. "Commentary on Building Code Requirements for Reinforced Concrete (ACI 318-63)," American Concrete Institute, Detroit, MI, 1965.
4. ACI Committee 318-71. "Commentary on Building Code Requirements for Reinforced Concrete (ACI 318-71)," American Concrete Institute, Detroit, MI, 1971.
5. ACI Committee 440.1 R-03. "Guide for the Design and Construction of Concrete Reinforced with FRP Bars, American Concrete Institute, Farmington Hills, MI, 2003.
6. ASTM A 370 – 02, "Standard Test Methods and Definitions for Mechanical Testing of Steel Products," American Society for Testing and Materials, West Conshohocken, PA, 2002.
7. ASTM A 615/A 615M – 01b, "Standard Specification for Deformed and Plain Billet-Steel Bars for Concrete Reinforcement," American Society for Testing and Materials, West Conshohocken, PA, 2001.
8. ASTM C 39/C 39M – 01, "Standard Test Method for Compressive Strength of Cylindrical Concrete Specimens," American Society for Testing and Materials, West Conshohocken, PA, 2001.
9. ASTM C 78 – 02, "Standard Test Method for Flexural Strength of Concrete (Using Simple Beam with Third-Point Loading)," American Society for Testing and Materials, West Conshohocken, PA, 2002.
10. ASTM C 143/C 143M – 00, "Standard Test Method for Slump of Hydraulic-Cement Concrete," American Society for Testing and Materials, West Conshohocken, PA, 2000.
11. ASTM C 192/C 192 M – 00, "Standard Practice for Making and Curing Concrete Test Specimens in the Laboratory," American Society for Testing and Materials, West Conshohocken, PA, 2000.
12. Almusallam, A. A., M. Abdul-waris, M. Maslehuddin, and A. S. Al-gahtani. "Placing and Shrinkage at Extreme Temperatures." *Concrete International* 21.1 (1999): 75-9.

13. Babaei, Khossrow and Amir M. Fouladgar. "Solutions to Concrete Bridge Deck Cracking." *Concrete International* 19.7 (1997): 34-6.
14. Banthia, Nemkumar and Cheng Yan. "Shrinkage Cracking in Polyolefin Fiber-Reinforced Concrete." *ACI Materials Journal* 97.4 (2000): 432-37.
15. Dobrowolski, Joseph A. *Concrete Construction Handbook*. New York: McGraw-Hill Inc., 1998.
16. Fricks, Terry. "Cracking in Floor Slabs." *Concrete International* 14.2 (1992): 59-63.
17. Frosch, Robert J. "Another Look at Cracking and Crack Control in Reinforced Concrete." *ACI Structural Journal* 96.3 (1999): 437-42.
18. Frosch, Robert J. "Flexural Crack Control in Reinforced Concrete." *Design and Construction Practices to Mitigate Cracking* 204.06 (2001): 136-53.
19. Gergely, Peter. "Distribution of Reinforcement for Crack Control." *Journal of the American Concrete Institute* 69.5 (1972): 275-77.
20. Ghali, A. and R. Favre. *Concrete Structures Stresses and Deformations*. London: E & Fn Spon, 1994.
21. Gilbert, R. Ian. "Shrinkage Cracking in Fully Restrained Concrete Members." *ACI Structural Journal* 89.2 (1992): 141-49.
22. Hughes Brothers Inc. "Glass Fiber Reinforced Polymer (GFRP) Rebar, Aslan 100." Seward, NE, 2001.
23. Leonhardt, Fritz. "Crack Control in Concrete Structures." *International Association for Bridge and Structural Engineering* (1977).
24. Lloyd, John P., Hassen M. Rejali, and Clyde E. Kesler. "Crack Control in One-Way Slabs Reinforced with Deformed Welded Wire Fabric." *Journal of the American Concrete Institute* 66.5 (1969): 366-76.
25. MacGregor, James G. *Reinforced Concrete Mechanics and Design*. Upper Saddle River: Prentice Hall, 1997.
26. Mehta, Harshvardhan C., John W. Vanderhoff, John A. Manson, and Wai F. Chen. "High-Temperature Drying of Thick Concrete Slabs." *Journal of Transportation Engineering* 102.2 (1976): 185-99.
27. Mindess, Sidney, J. Francis Young, and David Darwin. *Concrete*. Upper Saddle River: Prentice Hall, 2003.

28. Myers, J.J., V. Gopalaratnam, A. Nanni, D. Stone, and T.P. Earney, "Precast I-girder Cracking: Causes and Design Details," Center for Infrastructure Engineering Studies and Missouri Department of Transportation Research, Development, and Technology Report Number 00-06, January 2001.
29. "National Bridge Inventory," U.S. Department of Transportation, Federal Highway Administration, Washington, D.C., 2002.
30. Portland Cement Association. "Building Movements and Joints." 1st Ed. Skokie, IL, 1982.
31. Soroushian, Parviz, Faiz Mirza, and Abdulrahman Alhozaimy. "Plastic Shrinkage Cracking of Polypropylene Fiber Reinforced Concrete." *ACI Materials Journal* 92.5 (1995): 553-60.
32. Soroushian, Parviz and Siavosh Ravanbakhsh. "Control of Plastic Shrinkage Cracking with Specialty Cellulose Fibers." *ACI Materials Journal* 95.4 (1998): 429-35.
33. Uno, Paul J. "Plastic Shrinkage Cracking and Evaporation Formulas." *ACI Materials Journal* 95.4 (1998): 365-75.
34. Wang, Chu-Kia and Charles G. Salmon, *Reinforced Concrete Design*. Addison Wesley Educational Publishers, Inc., 1998.
35. Weiss, Jason W., Wei Yang, and Surendra P. Shah. "Shrinkage Cracking of Restrained Concrete Slabs." *Journal of Engineering Mechanics* 124.7 (1998): 765-74.
36. Yang, Y. and J.J. Myers. "Thermal Behavior of Missouri's First High Performance Concrete Superstructure Bridge." *Proceedings for the PCI/FHWA International Symposium on High Performance Concrete*, Orlando, FL., Sept. 2003, Submitted.